BERGISCHE
UNIVERSITÄT
WUPPERTAL

JÜLICH
Forschungszentrum

Characterization and calibration of the AtmoLITE satellite instrument for the INSPIRESat-4 mission

Dissertation

zur Erlangung des Grades
Doktor der Naturwissenschaften (Dr. rer. nat.)

vorgelegt der

Bergischen Universität Wuppertal
Fakultät für Mathematik und Naturwissenschaften

von

Qiucheng Gong

Wuppertal, April 2022

The PhD thesis can be quoted as follows:

urn:nbn:de:hbz:468-20220608-110107-1
[http://nbn-resolving.de/urn/resolver.pl?urn=urn%3Anbn%3Ade%3Ahbz%3A468-20220608-110107-1]

DOI: 10.25926/sffy-4w19
[https://doi.org/10.25926/sffy-4w19]

Abstract

Temperature measurements in the mesosphere and lower thermosphere (MLT) region play an important role in understanding atmospheric photochemical and dynamical processes. A miniaturized limb sounder aboard the atmospheric coupling and dynamics explorer INSPIRESat-4 is developed by our research team to enable temperature detection in the MLT region by observing the oxygen atmospheric band (O_2 A-band) day and night airglow emissions near 762 nm. Temperature is obtained from the rotational structure of the emission band, which follows a Boltzmann distribution. The intensity ratios of different emission lines at different temperatures are used to retrieve atmospheric temperature.

The International Satellite Program in Research and Education (INSPIRE) is a worldwide consortium of universities and research institutions formed to advance space science and engineering. INSPIRESat-4 is the fourth satellite in the INSPIRE series of satellites. Atmospheric limb interferometer for temperature exploration (AtmoLITE) is one of the payloads carried by the INSPIRESat-4 mission.

AtmoLITE uses a spatial heterodyne spectrometer (SHS) which is a monolithic small bandpass high-resolution interferometer. The characterization of this instrument is the main subject of this work, which can be divided into three phases: before the SHS glueing for the AtmoLITE instrument, during and after the SHS glueing for the AtmoLITE instrument, and after finalising the integration of the SHS system. At each phase, corresponding measurement strategies and alignment procedures are presented.

Before the SHS glueing for the AtmoLITE instrument, wavefront error measurements are performed on the different SHS front and camera optics samples for the AtmoLITE instrument's qualification model (QM) and flight model (FM). Quantitative analysis of the wavefront errors for the different optics samples is carried out to verify that the assembled optics samples meet the design requirements.

During and after the SHS glueing for the AtmoLITE instrument, a pinhole light

source setup is built to adjust the last lens of the front optics to find the optimum position with the smallest image point. The alignment result of the front optics shows that the measured spot size of 10 pixels matches the simulated result of 8 pixels with the alignment uncertainty about 2 pixels, which indicates that the alignment procedures for the front optics are correct and appropriate. After moving the vacuum compensator of the front optics, the measured spot size is two to three times larger than the simulated spot size. This will reduce our spatial resolution by a factor of about two or three. Meanwhile, the variation of the spot size at different temperatures is investigated. The results show that the spot size imaged by the pinhole setup increases as the temperature decreases. This suggests that due to the use of aluminium as an optomechanical material, the effect of its thermal expansion on the optical performance of the instrument should be further investigated for further missions.

After finalising the integration of the SHS system, a series of interferogram measurements have been performed at different wavelengths and temperatures in the vacuum environment, and corresponding calibration procedures are discussed which mainly include the dark and bias current subtraction, spike correction, removal of the DC and low frequency components, Littrow wavelength calibration, phase distortion correction and amplitude variation estimation. The Littrow calibration results show that there is a linear trend of temperature dependence. The expected thermal drift value for the Littrow wavenumber should be less than 1 cm^{-1} over the nominal operating temperature range, but the measured thermal drift of the Littrow wavenumber is up to 6 cm^{-1}. This means that the actual Littrow wavelength in the in-orbit measurements will shift towards the shorter wavelengths, resulting in the spectral overlap. Therefore, the ghost line removal needs to be considered for the in-orbit measurements. The calibrated results show that the validity of the calibration method and the final amplitude calibration matrix is obtained, which shows that the temperature dependence of the amplitude variation is almost negligible.

Contents

Chapter 1

Introduction

The middle atmosphere (stratosphere, mesosphere and lower thermosphere) which includes the mesopause region with the coldest temperatures on Earth is highly affected by anthropogenic activities and global change is clearly visible herein. One of the least explored dynamical processes in the middle atmosphere is gravity or buoyancy waves. Gravity waves propagate vertically and horizontally, carrying momentum from the troposphere up to the stratosphere, the mesosphere, and even to the thermosphere. The breaking of gravity waves drives the planetary wind circulation. Atmospheric temperature reflects the thermal balance of the atmosphere and causes significant atmospheric and ionospheric variability. The temperature field is also an essential component in the identification and quantification of atmospheric waves, as they displace air parcels adiabatically both in vertical and horizontal directions. Therefore, amplitudes, wavelengths, and phases of gravity waves can be determined from its temperature structure.

Research Centre Jülich and its partners proposed the AtmoSat satellite mission, which was planned to carry three main payloads: Gimballed Limb Observer for Radiance Imaging of the Atmosphere (GLORIA), Multiple Eye for Remote Investigation of the Atmosphere (MERIA) and Global Positioning System (GPS) radio occultation.

GLORIA is an imaging Michelson Fourier-transform infrared spectrometer. It detects the infrared radiation emitted by trace gases and aerosols to retrieve atmospheric temperature and the distribution of trace gases. MERIA consists of novel narrow-band heterodyne spectrometers. One channel detects the infrared airglow emissions from the oxygen atmospheric band (O_2 A-band) and another channel detects the ultraviolet airglow emissions from nitric oxide (NO) in the mesosphere and lower thermosphere region to obtain atmospheric temperature and the density of nitric oxide and atomic oxygen.

Nitric oxide is one of the major molecules affecting the energy balance of the up-

per atmosphere (*Roble et al.*, 1987; *Sætre et al.*, 2004). Like carbon dioxide (CO_2), it has vibration-rotation modes and emits infrared radiation. The nitric oxide thermal emissions at 5.3 μm contribute to the cooling of the lower thermosphere, especially for high solar activity (*Barth et al.*, 2009; *Barth*, 2010; *Hendrickx et al.*, 2018). The energy transfer from the ambient atmosphere to nitric oxide is done via collisions with atomic oxygen.

Atomic oxygen itself plays a key role in the thermal budget of the upper atmosphere (*Zhu et al.*, 2015; *Zhu and Kaufmann*, 2018, 2019; *Zhu*, 2016). It determines the amount of radiation emitted by CO_2 at 15 μm, in a similar way as for nitric oxide. Through intra-molecular collisions, atomic oxygen transfers thermal energy from the ambient atmosphere to infrared-active species such as CO_2 and NO, which radiate into space. Therefore, atomic oxygen is key for the energy budget, but its abundance needs also to be known to retrieve the abundance of CO_2 and NO, which are in non-local thermodynamic equilibrium.

The AtmoSat mission was finally not approved. The O_2 A-band instrument will be deployed on several other missions, but the development of the NO SHS instrument was put on hold. After an in-orbit demonstration of that instruments on a Chinese technology demonstration mission, the next deployment of the O_2 A-band instrument is the INSPIRESat-4 mission. The characterization of that instrument is the main subject of this work.

AtmoLITE is a spatial heterodyne spectrometer (SHS) which is capable of resolving individual emission or absorption lines in the atmosphere (*Kaufmann et al.*, 2018). The core of the instrument, the spatial heterodyne interferometer (SHI), was originally proposed in 1958 (*Connes*, 1958), which gains increased attention in recent decades due to the improvements of the imaging detectors. Compared with a traditional Fourier transform spectrometer, this kind of instrument owns higher spectral resolution, and it can be built as a monolith which makes it rigid and fault tolerant, which are both important factors for aerospace application. Additionally, a field-widened SHS with a prism in each arm of the interferometer increases the etendue or the throughput of the spectrometer by one to two orders of magnitude compared to a non-field-widened SHS.

The first generation payload of this satellite instrument is called atmospheric spatial heterodyne interferometer next exploration (AtmoSHINE), which was successfully deployed on the 22nd of December 2018 from the Jiuquan Satellite Launch Center into a sun-synchronous orbit. The spectra obtained from the in-orbit measurements effectively resolved the O_2 A-band emissions (*Liu*, 2019; *Chen*, 2020).

This thesis focuses on the characterization and calibration of the AtmoLITE instrument. Chapter 2 describes the principle of the SHS. Chapter 3 presents the optical component characterization before the SHS glueing for the AtmoLITE instrument. The

wavefront error measurements on the SHS front and camera optics for the AtmoLITE instrument are discussed in this chapter. Chapter 4 describes the optical performance characterization during and after the SHS glueing for the AtmoLITE instrument. Chapter 5 presents the property characterization and calibration results of the AtmoLITE instrument after finalising the integration of the SHS system.

Chapter 2

The Principle of the SHS

As an emerging passive optical detection technology, SHS is widely used in remote sensing applications such as atmospheric constituent measurement, temperature detection and wind speed detection (*Harlander*, 1991; *Harlander et al.*, 1992, 1994; *Cooke et al.*, 1999; *Milligan et al.*, 1999; *Cardon et al.*, 2003; *Harris et al.*, 2005; *Englert et al.*, 2006a,b, 2010; *Yi et al.*, 2017; *Kaufmann et al.*, 2018). The schematic diagram of a typical non-imaging transmission SHS is shown in Figure 2.1, where the return mirrors of a conventional Michelson interferometer are replaced by two reflective diffraction gratings 1 and 2. The light from an extended point source enters through the entrance aperture with a limited field of view (FOV) and is collimated by the collimating lens 1 to form a parallel beam incident on the beamsplitter, where the incident wavefront is divided into two coherent wavefronts. The reflective diffraction grating in each arm returns the wavefront back to the beamsplitter. For each wavelength within the spectral range, the two wavefronts exit at a wavelength-dependent intersection angle between each other. The resulting superposition of the Fizeau fringes with wavelength-dependent spatial frequencies is located on the localization plane near the grating as a virtual image of the grating. Lens 2 and lens 3 image the localization plane onto the detector to record the interferogram, where along the x-direction is the spectral direction (or the dispersion direction of the grating).

For an arbitrary incoming spectral radiation $B(\sigma)$, the intensity distribution recorded as a function of the position x is given by (*Harlander*, 1991):

$$I(x) = \frac{1}{2}\int_0^\infty B(\sigma)\left[1+\cos\left(2\pi f_x x\right)\right]d\sigma, \tag{2.1}$$

where σ is the wavenumber of the incoming emission line and f_x is the heterodyne

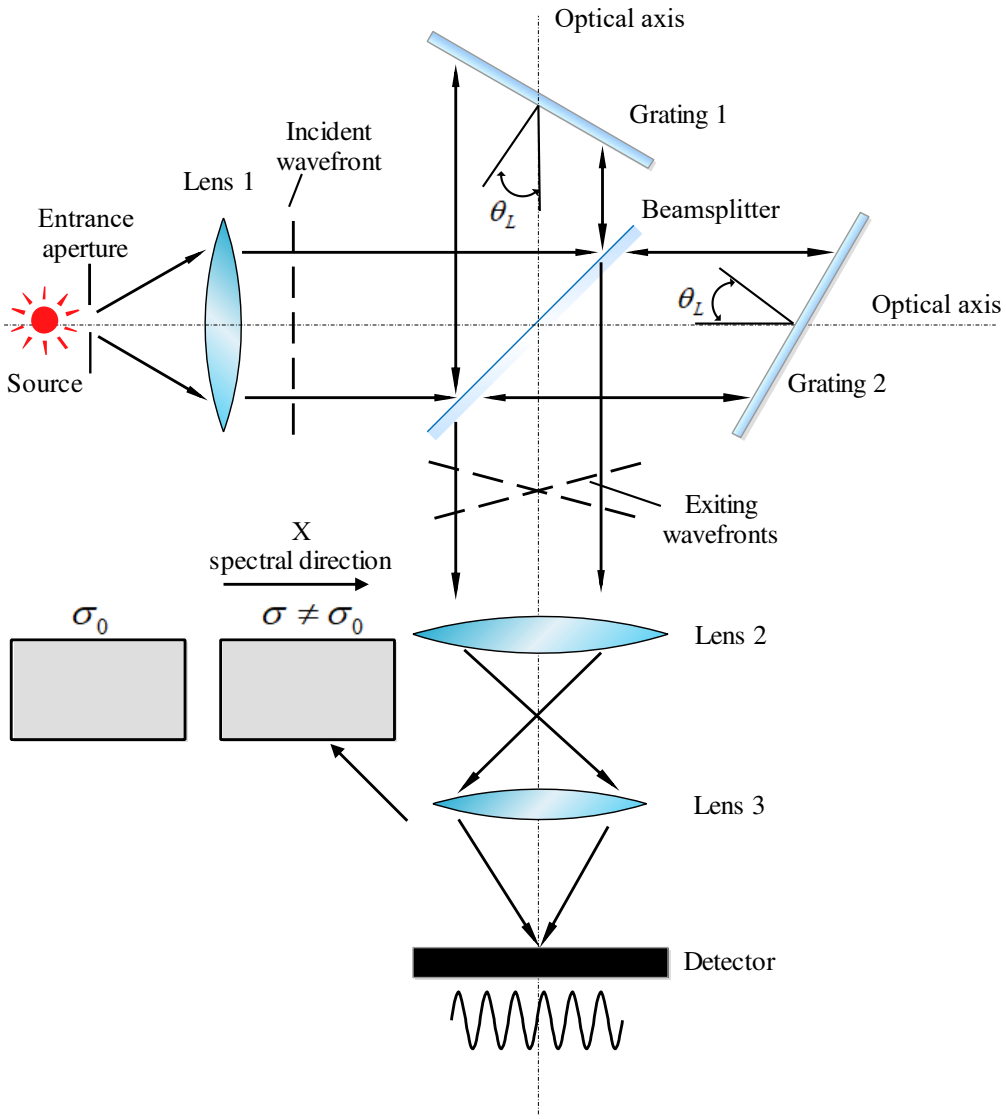

Figure 2.1: Schematic diagram of a basic non-imaging transmission SHS. Note that θ_L denotes the Littrow angle of the reflective diffraction grating. σ_0 and σ represent the Littrow wavenumber of the SHS and the wavenumber of the incident light, respectively.

spatial frequency of the recorded interferogram:

$$f_x = 4 \tan \theta_L (\sigma - \sigma_0), \tag{2.2}$$

in which θ_L is the Littrow angle of the grating and σ_0 is the corresponding Littrow

wavenumber of the SHS:

$$\sigma_0 = \frac{m}{2d\sin\theta_L}. \tag{2.3}$$

Note that m is the diffraction order or spectral order, and d is the groove spacing of the grating. Equation 2.1 is derived from the grating equation under the approximate condition of small angular incidence of paraxial light and does not take into account the effects of the phase distortion and optical efficiency. The modulated part of the interferogram intensity distribution $I(x)$ is the Fourier transform of the incoming spectral radiation $B(\sigma)$.

In Equation 2.2, the $(\sigma - \sigma_0)$ term represents the heterodyned nature of the SHS, which is fundamentally different from a conventional Fourier transform spectrometer (FTS) that records the interferograms from zero wavenumber. This means that the SHS technology can achieve ultra-high spectral resolution (resolving power) within a small spectral range for a given centre frequency, which can be explained by the optical path difference (OPD in terms of geometrical optics.

The spectral resolution of the SHS is associated with the instrument line shape (ILS, which is related to the maximum OPD of the designed optical system(*Watchorn*, 2001; *Lin*, 2010; *Cai*, 2016):

$$\delta\sigma = \frac{1}{2OPD_{max}}, \tag{2.4}$$

where $\delta\sigma$ is the minimum resolvable wavenumber interval.

The illustration of the OPD between two diffracted rays is shown in Figure 2.2, where the plane HH$'$ is the fringe localization plane parallel to the dispersion direction of the grating. The paraxial ray ED is diffracted by the Grating2 at an angle of β, and its transmitting ray DA is diffracted by the Grating1 at an angle of β in opposite direction.

The OPD between the two diffracted rays can be expressed as:

$$OPD = DA + AB + BD = 2(AB + AC) = 2AB(1 + \cos\beta). \tag{2.5}$$

For the paraxial rays, the angle β has a small value. Equation 2.5 can be approximately calculated as:

$$OPD \approx 4AB. \tag{2.6}$$

In the triangle OAB, AB can be obtained from the law of sines:

$$AB = OB\frac{\sin\theta_L}{\sin\left(\frac{\pi}{2} - \theta_L + \beta\right)} \approx OB\frac{\sin\theta_L}{\cos\theta_L} = OB\tan\theta_L. \tag{2.7}$$

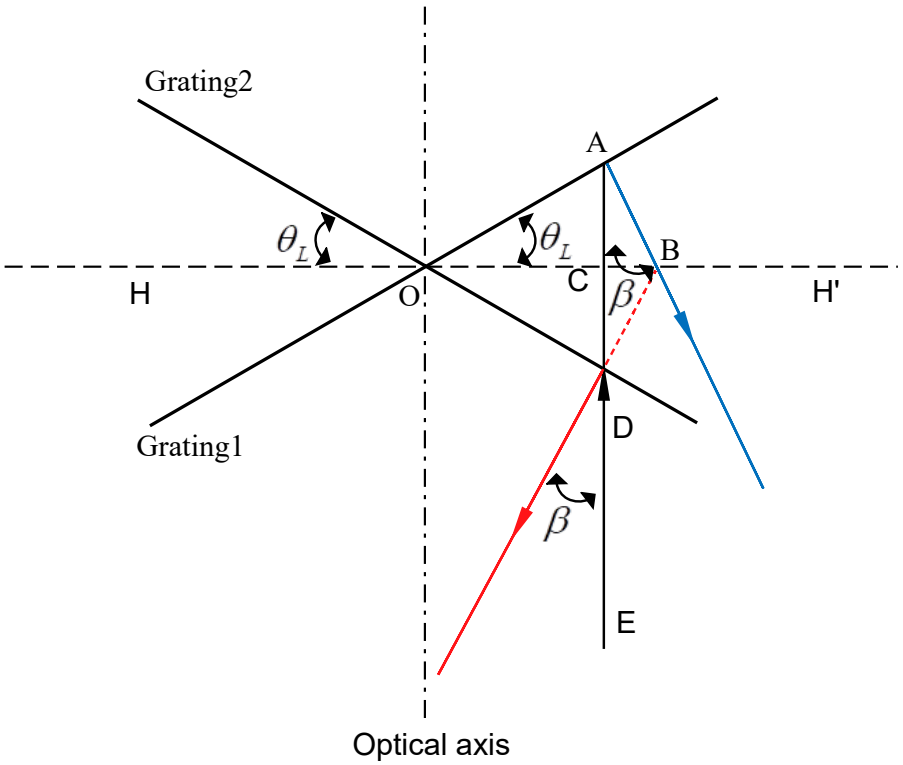

Figure 2.2: Illustration of the optical path difference between two diffracted rays, where the plane HH′ is the fringe localization plane parallel to the dispersion direction of the grating. The paraxial ray ED is diffracted by the Grating2 at an angle of β, and its transmitting ray DA is diffracted by the Grating1 at an angle of β in opposite direction.

The coordinate value of the point B is x, then:

$$OPD \approx 4x \tan\theta_L. \tag{2.8}$$

The maximum OPD can be calculated as:

$$OPD_{max} = 4x_{max} \tan\theta_L = 4 \tan\theta_L * \frac{1}{2} W \cos\theta_L = 2W \sin\theta_L, \tag{2.9}$$

where W is the illuminated width of the grating. Combining Equation 2.9 with Equation 2.4 gives:

$$\delta\sigma = \frac{1}{2OPD_{max}} = \frac{1}{4W \sin\theta_L}. \tag{2.10}$$

So the theoretical resolving power R of the SHS system can be deduced as:

$$R = \frac{\sigma}{\delta\sigma} = 4W \sin\theta_L \sigma. \tag{2.11}$$

Assuming that the incident wavenumber is equal to the Littrow wavenumber $\sigma = \sigma_0$, the resolving power can be calculated by:

$$R = 4W \sin\theta_L \sigma_0 = \frac{2Wm}{d} = 2N_{groove}(m = 1), \tag{2.12}$$

where Equation 2.3 was used in the second step and N_{groove} is the number of the illuminated grooves on the grating. It can be found that the theoretical resolving power of the SHS system is twice that of the grating. This is the significant advantage of the SHS system.

Chapter 3

Optical Components Characterization before the SHS glueing for the AtmoLITE Instrument

From this chapter onwards, the major work of this thesis, namely the characterization and calibration of the AtmoLITE instrument, will be discussed. Due to the chronological order of the assembly procedure, the AtmoLITE instrument consists of three versions: qualification model (QM) with old optical design (AtmoSHINE optics), prototype and flight model (FM), both with new optical design. For the AtmoLITE instrument, the most important optical components are the bandpass filter, the front optics, the camera optics and the SHI.

The main assembly, test and characterization procedures for the optical components of the AtmoLITE instrument, as shown in Figure 3.1, are:

1) Optical design: An optical design software was used to optimise the design of the SHS system: front optics, camera optics, SHI and bandpass filter.

2) Wavefront error measurement: The assembled front optics and camera optics were tested to select the optics that meet design requirements.

3) Glueing and assembling the SHI: The selected front optic and camera optic were used as the imaging system to glue and assemble the SHI. During the glueing process, the distance between the last lens of the front optics and the SHI, the distance between the SHI and the camera optics and the distance between the camera optics and the detector were adjusted to obtain the optimum performance of the SHS system.

4) Integrating the SHS system: The front optics, camera optics, bandpass filter, SHI and mechanical and electronic modules were integrated together to obtain the final SHS system.

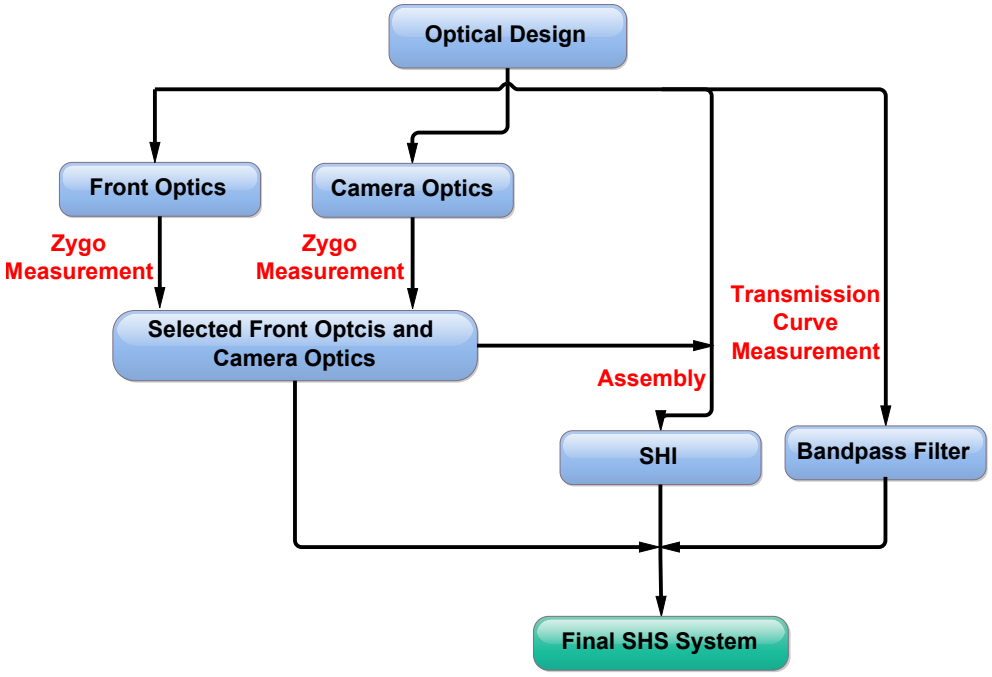

Figure 3.1: Flow chart for assembly, testing and characterization of the optical components of the AtmoLITE instrument.

This chapter mainly describes wavefront error measurements on the SHS front and camera optics for the AtmoLITE instrument's QM and FM. In addition, Section 3.4 presents an alternative version of the glass materials for the AtmoLITE instrument.

3.1 Optical Properties and Overview of the QM and FM

The AtmoLITE instrument's QM was assembled with the AtmoSHINE optical design. Figure 3.2(a) shows the corresponding shaded optical layout, including the bandpass filter, the front optics, the camera optics and the SHI with one arm. The front optics consists of four lenses, which image the atmosphere at infinity with a FOV of 1.3° onto the grating (so-called localization plane). The spatial resolution of the system is highly dependent on the performance of the front optics. The camera optics consists of four

lenses that image the localization plane onto the detector to obtain an interferogram. Its performance affects the visibility and imaging quality of the system.

The AtmoLITE instrument's FM was assembled with the new optical design, as shown in Figure 3.2(b). The most notable difference compared to the AtmoSHINE optical design is that the FM's camera optics consists of three lenses.

Table 3.1 presents the optical properties and specifications of the QM and FM. The most significant difference compared to the QM is the increased operating wavelength range of the FM. The operating wavelength range of the QM covers only one branch of the O_2 A-band, but the operating wavelength range of the FM covers both branches of the O_2 A-band, where most of the bright emission lines are located. This variation produces more information about the temperature and thus increases the accuracy of the temperature measurement.

Table 3.1: Optical properties and specifications of the QM and FM

Item	QM	FM
Littrow wavenumber [cm^{-1}]	13127	13047
Littrow wavelength [nm]	761.8	766.5
Littrow angle [°]	27.2	6.6
Grating groove density [cm^{-1}]	12000	3000
Resolving power [-]	16800	9000
Aperture diameter [mm]	68	75
Field of view [°]	1.3	1.3
Magnification factor of the camera optics [-]	0.6	0.6
Number of illuminated detector pixels [-]	784*784	861*861
Detector pixel size [μm^2]	5.04*5.04	11.0*11.0
Illuminated detector area [cm^2]	0.3953^2	0.9472^2
Operating wavenumber range [cm^{-1}]	13065 to 13118	13057 to 13160
Operating wavelength range [nm]	762.3 to 765.4	759.9 to 765.9

To compare the imaging quality and visibility of the QM and FM, Figure 3.3 displays the grid distortion maps of the QM and FM. The grid distortion map, as an indicator of optical aberration, shows the grid of the intercept points of the chief ray to indicate radial

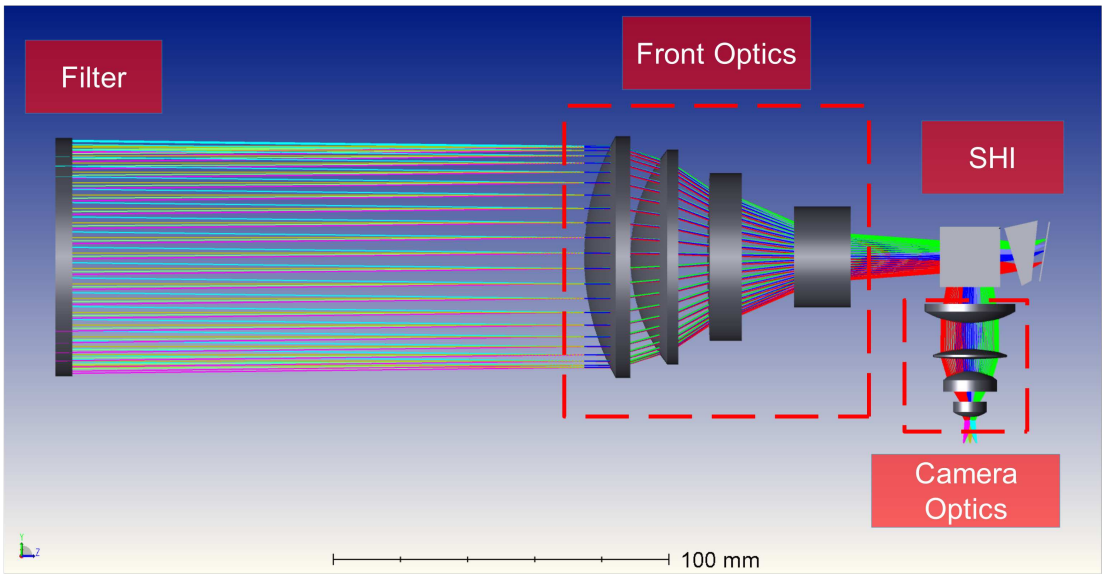

(a) The optical system layout for AtmoLITE's QM

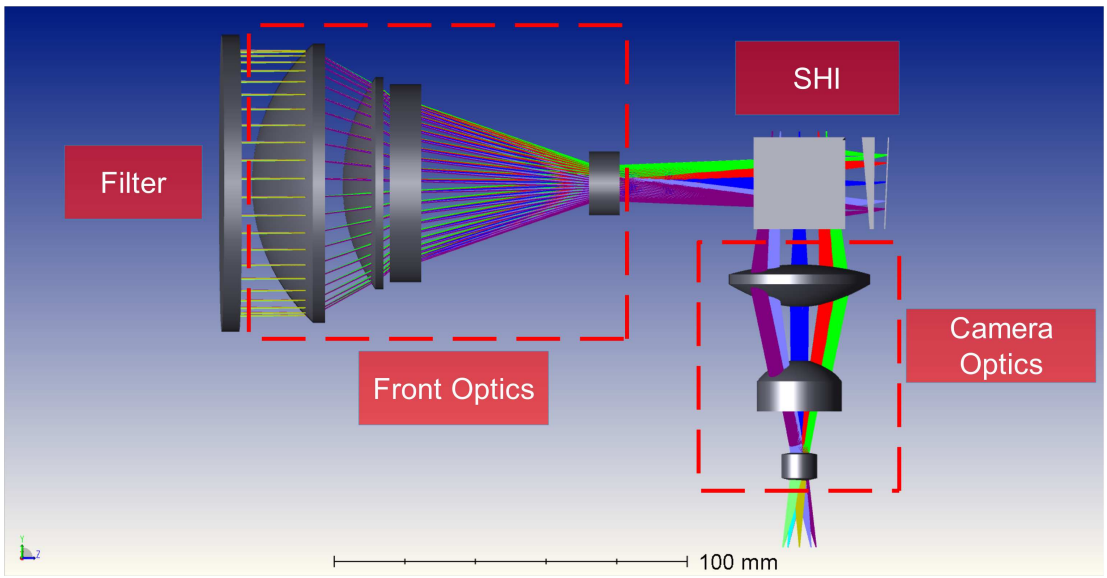

(b) The optical system layout for AtmoLITE's FM

Figure 3.2: The optical system layout for AtmoLITE's QM and FM, including the band-pass filter, the front optics, the camera optics and the SHI with one arm.

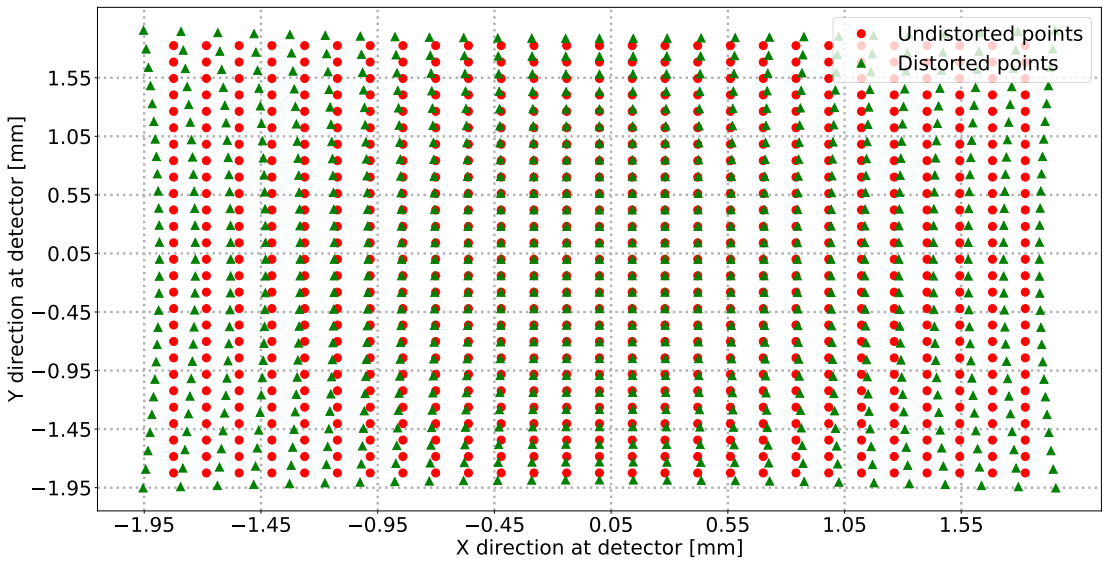

(a) Grid distortion map for the QM. The maximum distortion is 7.1211% relative to the primary wavelength of 763.01 nm

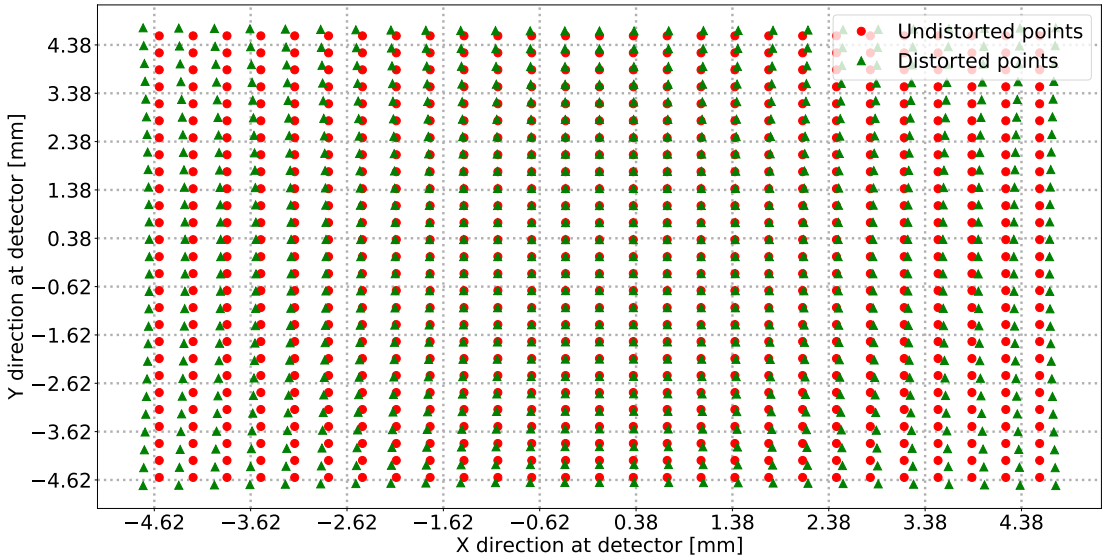

(b) Grid distortion map for the FM. The maximum distortion is 3.6750% relative to the primary wavelength of 766.46 nm

Figure 3.3: Grid distortion maps of the distorted and undistorted points obtained by ray-tracing simulation. The undistorted points represent the predicted ideal coordinates of the image points and the distorted points represent the actual coordinates of the image points. The grids are 27×27 points.

distortion (*ZEMAX LLC.*, 2020). The undistorted points represent the predicted ideal coordinates of the image points and the distorted points represent the actual coordinates of the image points. The size of the grid is 27∗27 points. The maximum radial distortion for the QM and FM is 7.1211% and 3.6750%, respectively, which means that the FM optical design has less image distortion compared to the QM optical design, thus, it has less variation in fringe frequency across the detector rows.

Figure 3.4 shows the RMS wavefront error field maps for the QM and FM with 100*100 sampling points. The maximum RMS wavefront error and minimum RMS wavefront error for the QM are 0.2052 and 0.0937 waves respectively. For the FM, they are 0.0882 and 0.0208 waves, respectively. The overall wavefront error of the FM is less than half of the wavefront error of the QM, which indicates that the visibility of the FM is higher than that of the QM.

In summary, the FM of the AtmoLITE instrument provides significantly better image quality and visibility than the QM.

3.2 Wavefront Error Measurements on the Front and Camera Optics for the QM

As previously mentioned, the wavefront quality of the AtmoLITE assembled front and camera optics should be measured to verify the correctness of the assembly before the SHS glueing. This section describes the wavefront error (WFE) measurements on the front and camera optics for the AtmoLITE instrument's QM.

The purpose of wavefront error measurements is to determine the transmitted wavefront error Peak-to-Valley (P-V) value of the front and camera optics by using a Zygo Dynafiz interferometer. Zygo laser interferometer has been widely accepted and applied in the optical industry (*Shukla et al.*, 1998; *Shukla and Udupa*, 2000; *Santiago-Alvarado et al.*, 2009). The Dynafiz-type interferometer as a new instantaneous Fizeau-type interferometer is suitable for wavefront error measurement. Its built-in software allows real-time wavefront analysis using Zernike polynomials during alignment and measurement.

Figure 3.5 shows the schematic diagram of a basic Fizeau-type laser interferometer in its standard configuration for measuring the quality of a reflecting surface. The light from the laser source (usually He-Ne laser) passes through the beamsplitter and is collimated by the collimation lens. Then the collimated wavefront passes through the transmission flat (TF), where the TF (usually the outermost surface of the TF) serves as a beamsplitter to divide the collimated wavefront into reference wavefront and testing wavefront. The reference wavefront will return back along the optical axis and the

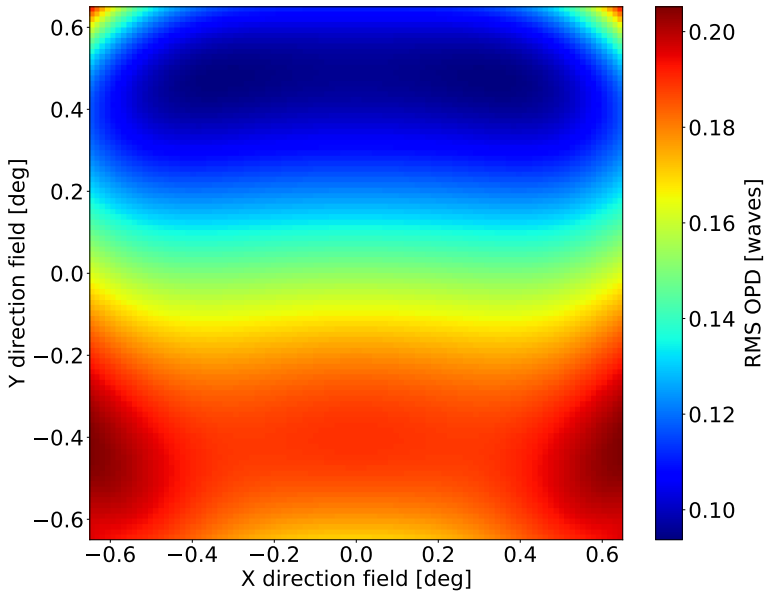

(a) RMS wavefront error field map for the QM with 100*100 sampling points. Max RMS = 0.2052 waves; Min RMS = 0.0937 waves

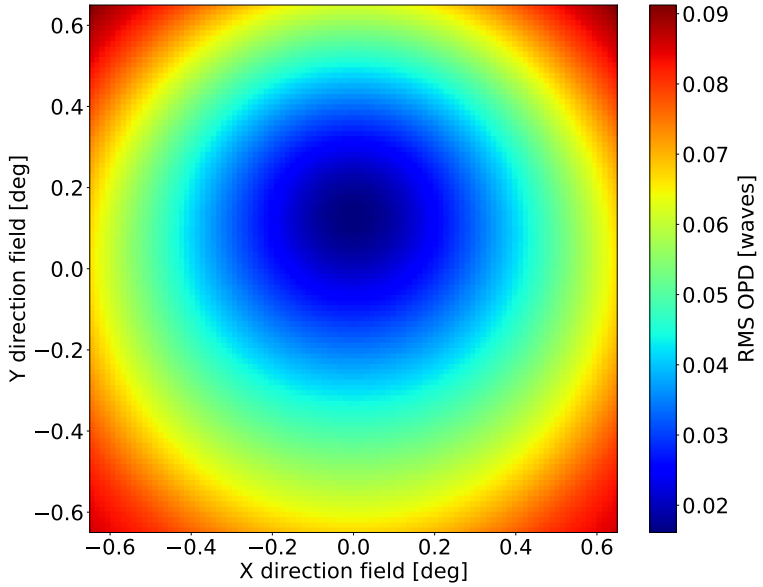

(b) RMS wavefront error field map for the FM with 100*100 sampling points. Max RMS = 0.0882 waves; Min RMS = 0.0208 waves

Figure 3.4: RMS wavefront error field maps for the QM and FM with 100*100 sampling points.

testing wavefront will propagate forward and reflect back by the test surface. The two wavefronts will recombine to form an interference fringe pattern. The geometrical properties of the interference fringe pattern are determined by the optical path difference of the two wavefronts, which include the information of the test surface. To characterize the front and camera optics, the test surface will be replaced by a reflective sphere (RS) reflecting the testing wavefront back, and the front or camera optics will be inserted between the TF or transmission sphere (TS) and RS.

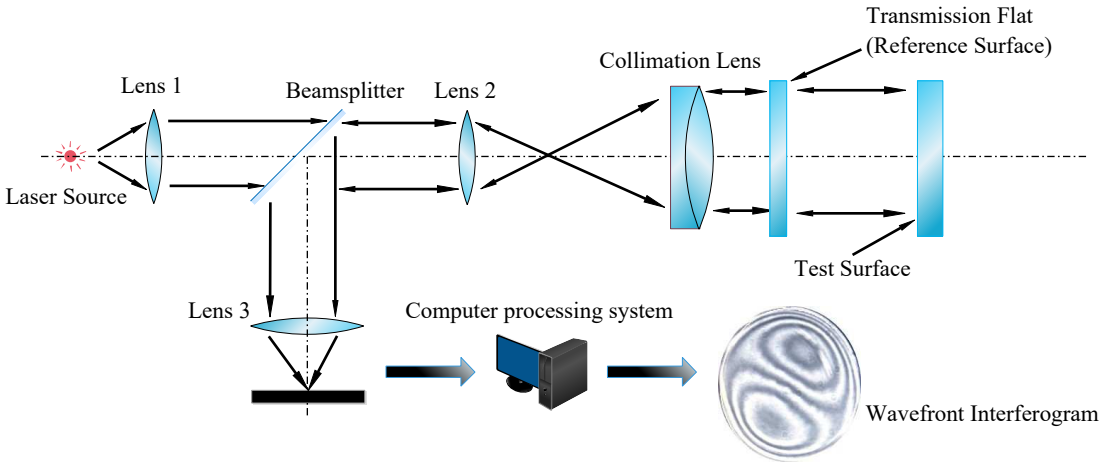

Figure 3.5: Schematic layout of a basic Fizeau-type laser interferometer.

3.2.1 Setup Schemes and Required Accessories

The infinite conjugate setup is used for the front optics due to the front optics is designed as an infinite-finite system, as shown in Figure 3.6(a). The camera optics is tested by using the finite conjugate configuration as it is designed as a finite-finite imaging system, as displayed in Figure 3.6(b). For the front optics, the transmission flat separates the wavefront into a collimated reference and testing wavefront. For the camera optics, the transmission sphere transforms the collimated wavefront into a spherical reference and testing wavefront. The actual configurations and distances will be given later. The required accessories are summarized as follows:

i) Interferometer: Zygo-Dynafiz; Model: MARK IV.

ii) Transmission Flat (TF, generating a collimated reflected reference wavefront and an identical transmitted measurement wavefront. The outermost surface of the TF acts as the beamsplitter); Type: Zygo standard TF 4"-4%.

iii) Transmission Sphere (TS, generating a converging beam. Usually the final surface of the TS is concentric with the focus point of the TS. This surface acts as the beamsplitter); Type: JENfizar TS 4"-f/1.5.

iv) Reflective Sphere (RS, which reflects the measurement beam back); Type: JENfizar RS-f/0.65 cc-hr.

v) Two front optics samples (front#1 and front#3); Two camera optics samples (camera#1 and camera#2) and corresponding mechanical holders.

vi) X-Y-Z-Rotation translation stage and tip-tilt mount for tip-tilt adjustment on the optics samples.

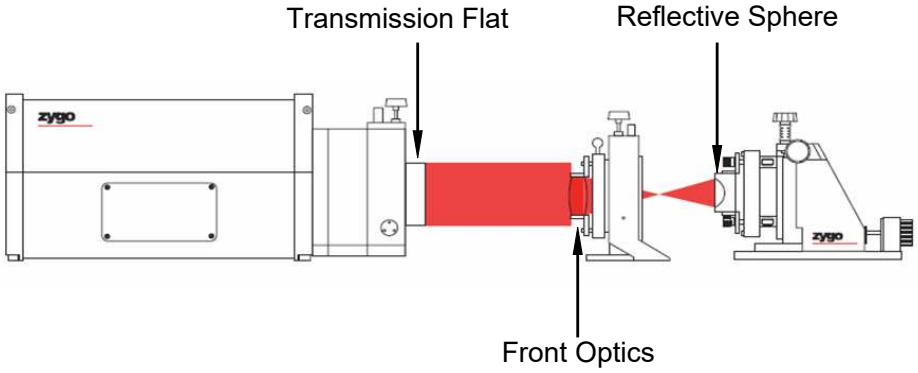

(a) The infinite conjugate setup scheme for the front optics

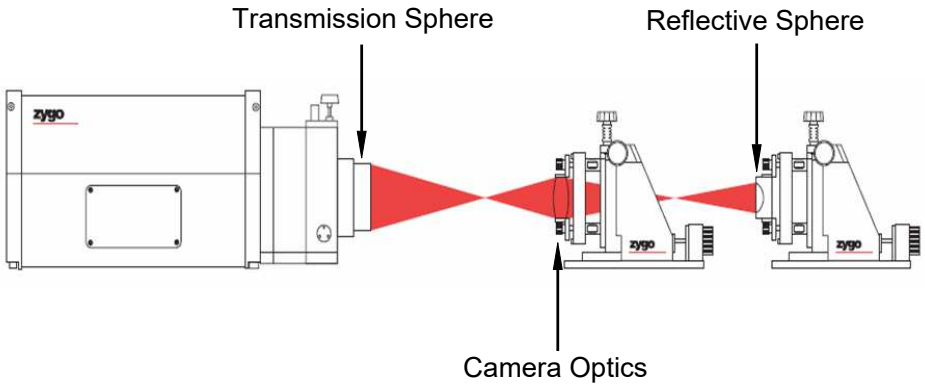

(b) The finite conjugate setup scheme for the camera optics

Figure 3.6: The infinite and finite conjugate setups for the front and camera optics, where the Zygo frame is taken from Zygo's guide manual (*ZYGO.*, 2015).

3.2.2 Front Optics Measurement Setup and Results

3.2.2.1 Front Optics Test Setup

The optical and mechanical setup used for testing the front optics is shown in Figure 3.7. The collimated interferometer beam from the Zygo was transmitted through the front optics to form a focus about 4 cm behind the last mechanical surface. The reflective sphere was placed at two times its focal distance from this focal point to ensure that the beam was travelling back the same optical path to the interferometer.

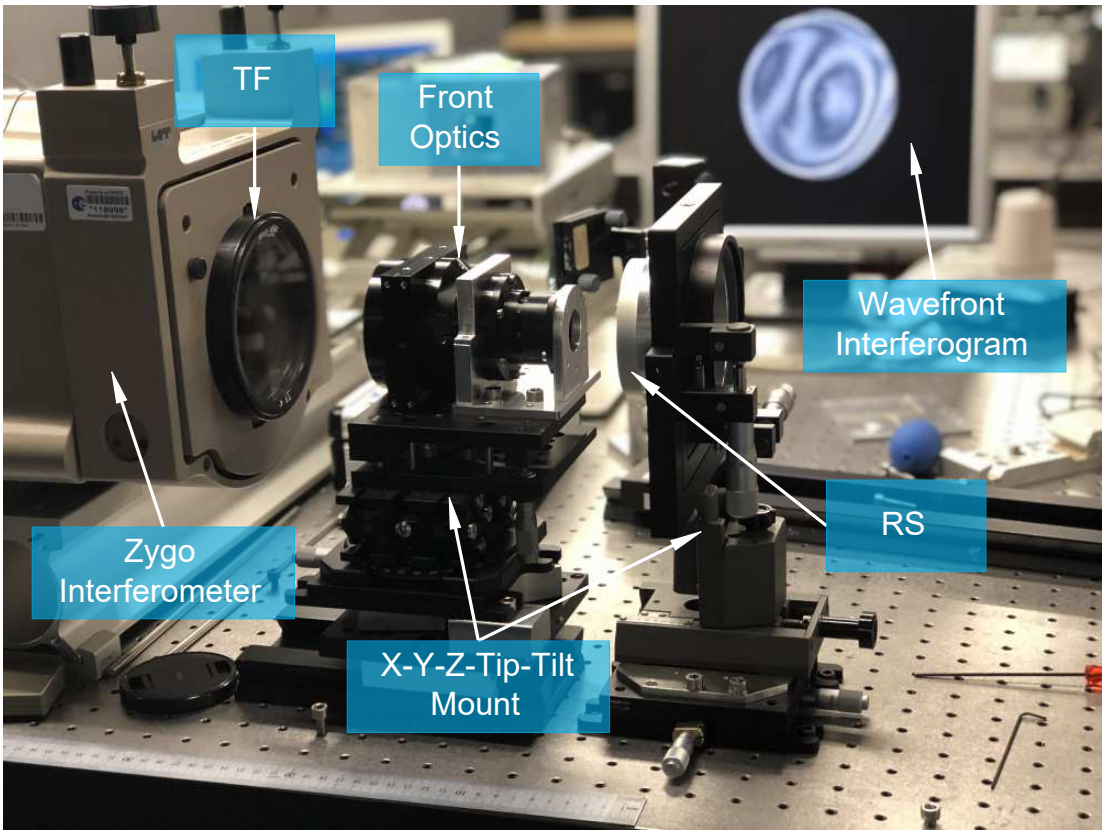

Figure 3.7: Measurement setup for the front optics with the old optical design.

3.2.2.2 Alignment and Measurement Procedures

In order to obtain a transmitted wavefront interferogram, the front optics, Zygo, TF and RS need to be aligned to a common optical axis. Note that a perfectly common optical path is an ideal situation and any interferometer system will have a certain amount of

wavefront errors. The aim of our alignment is to minimize the overall systematic errors. The alignment and measurement procedures are as follows:

1) Insert the TF into the accessory receptacle on the Zygo interferometer. Gently tighten the thumbscrews.

2) Press the 'Align/View' button on the remote control to switch to the Align mode.

3) Monitor the display screen and align the tip and tilt screws of the TF to center the brightest spot on the crosshairs so that the optical center of the TF is concentric with the optical aperture center of the Zygo interferometer.

4) Place the front optics onto corresponding mechanical holders in front of the TF.

5) Use a flag with a hole or a paper to find the foci position of the front optics.

6) Place the center of RS's surface at the foci of the front optics to reach the cat's-eye reflection. This step is to get the RS and Zygo to coaxial. Figure 3.8 shows

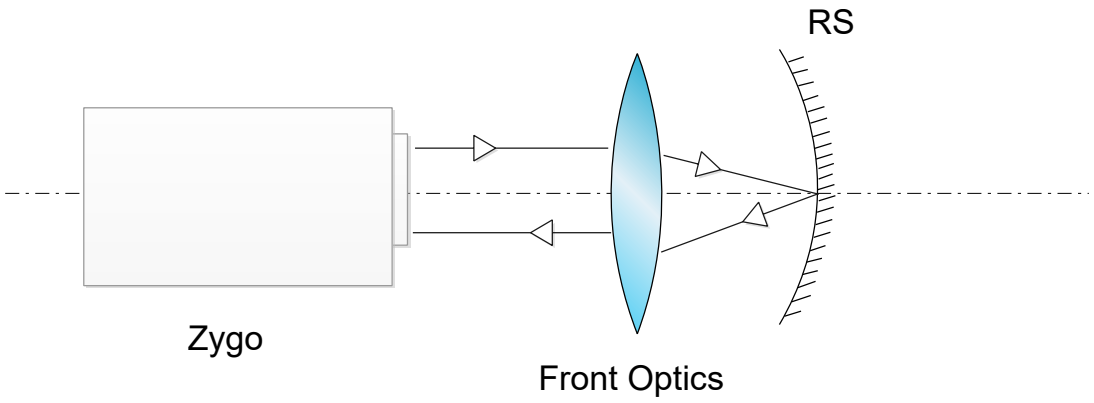

Figure 3.8: Measurement geometry for the cat's-eye reflection.

the measurement geometry for the cat's-eye reflection, where the light beam after passing through the front optics is focused at the center point of the RS. For this case, the light beam is reflected back parallel to the incident beam. Adjusting the x-y-z-tip-tilt mount of the RS to obtain a nulled fringe pattern which means the focal point of the front optics is correctly positioned at the centre of the RS. Figure 3.9 shows the process of reducing interference fringes. Meanwhile, to double verify that it is in the cat's-eye position, a piece of paper is inserted blocking the side of the optical beam. If the two symmetrical shadow images appear synchronously, it indicates that the cat's-eye position is reached, as shown in Figure 3.10.

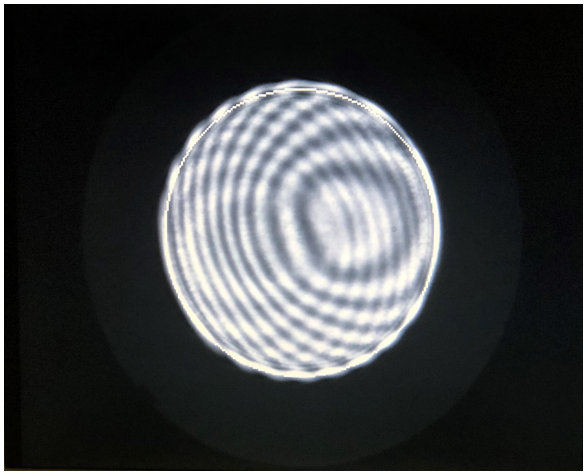

(a) Starting alignment

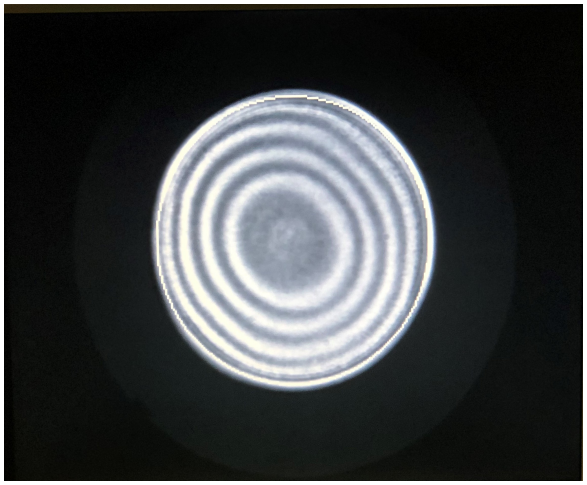

(b) Decreasing the number of fringes

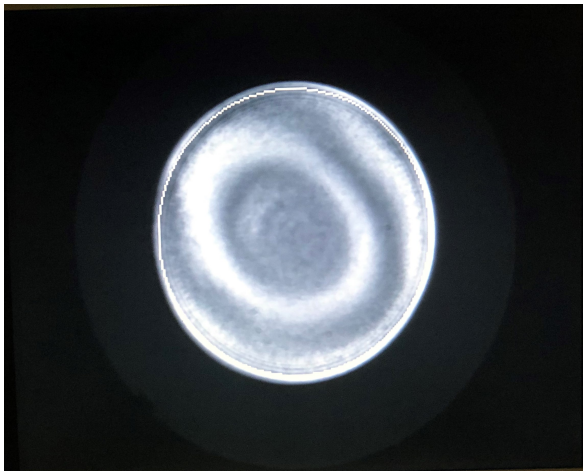

(c) Minimal fringes

Figure 3.9: Aligning procedures at the cat's-eye reflection.

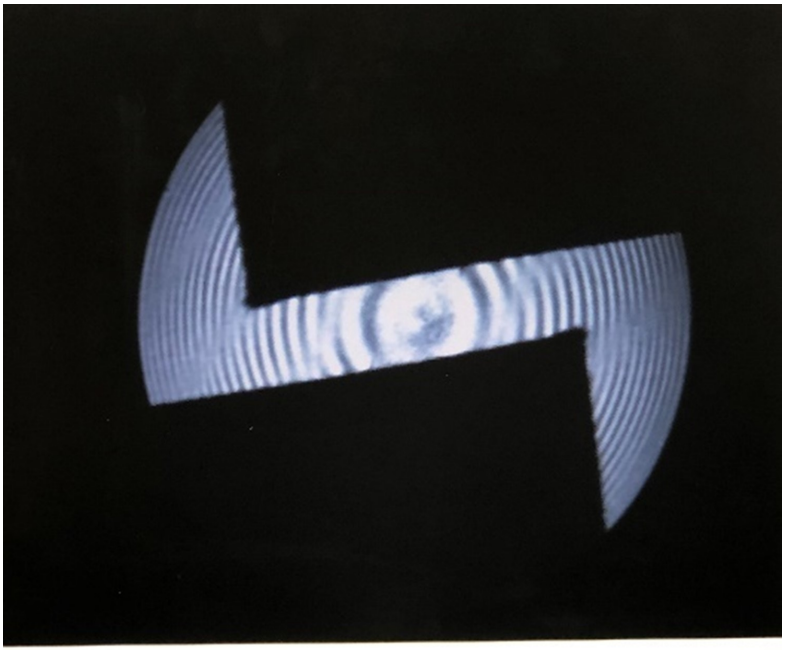

Figure 3.10: Verifying the cat's-eye position.

7) Place the RS at two times its focal distance from the foci position, and the imaging geometry is shown in Figure 3.11.

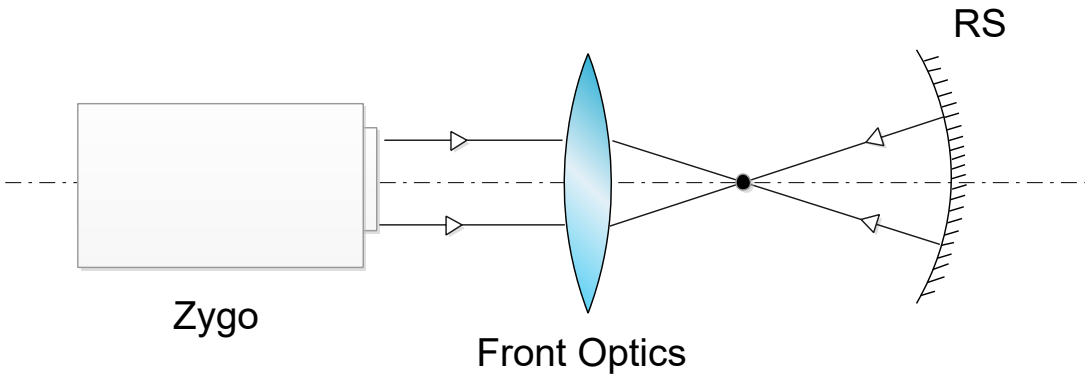

Figure 3.11: Imaging geometry for the front optics measurement.

8) Adjust the X-Y-Z-Rotation translation stage and tip-tilt mount for the front optics to minimize the number of interference fringes. The transmitted wavefront interferogram of the front optics will be obtained, as shown in Figure 3.12.

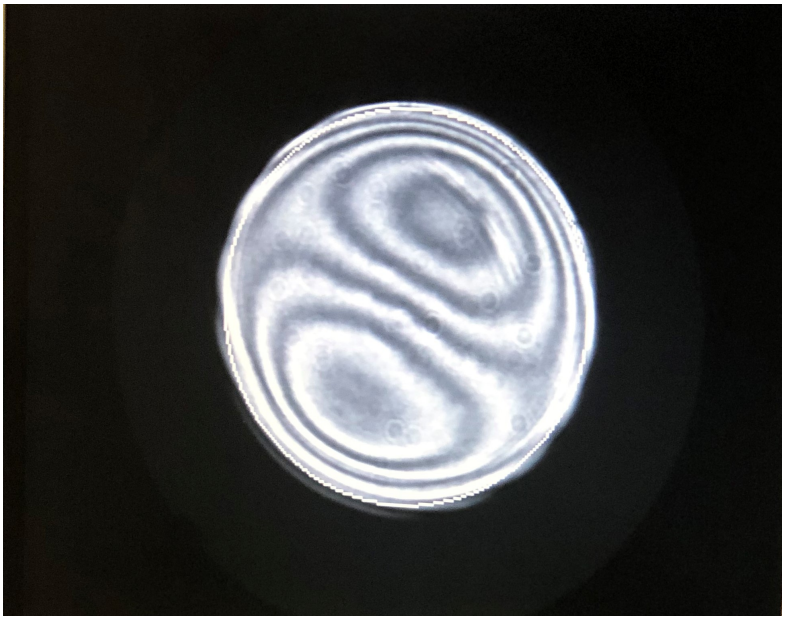

Figure 3.12: The transmitted wavefront interferogram sample of the front optics.

9) Due to the mechanical design of the front optics, the position of the last lens of the front optics can be adjusted by the screws, which are used to find the optimum position of the last lens of front optics. The last lens of the front optics is turned in successive turns of 30° to investigate the WFE performance.

10) Once the optimum position of the last lens of the front optics is found, the screws will be tightened into the barrel to fix the position of the last lens of the front optics. Then tilt the front optics to pass through the system at different field angles to evaluate the off-axis WFEs of the front optics.

3.2.2.3 Measurement Results

A full detailed measurement data report can be found at *Gong* (2020). This sub-section presents some important data for further analysis and discussion. The wavefront errors of the front optics were calculated and fitted by the first nine Zernike polynomials in Table 3.2.

The Zernike polynomials were introduced by the Dutch scientist Frederik Zernike in the early 20th century and have since been refined to describe the wavefront aberrations for an optical system with a circular pupil (*Lakshminarayanan and Fleck*, 2011; *Gray et al.*, 2012). Each term in the Zernike polynomials has an explicit physical meaning for the wavefront aberration. The first term of the Zernike polynomials Z_1 is a constant term

Table 3.2: Definition of the Zernike polynomials utilised in analysis of the WFEs

Number	Zernike Item	Aberration Type
Z_1	1	Piston
Z_2	$\rho\cos\theta$	Tilt in x-direction
Z_3	$\rho\sin\theta$	Tilt in y-direction
Z_4	$2\rho^2-1$	Defocus
Z_5	$\rho^2\cos(2\theta)$	Astigmatism 0°
Z_6	$\rho^2\sin(2\theta)$	Astigmatism 45°
Z_7	$(3\rho^3-2\rho)\cos\theta$	Coma in x-direction
Z_8	$(3\rho^3-2\rho)\sin\theta$	Coma in y-direction
Z_9	$6\rho^4-6\rho^2+1$	Spherical Aberration

that represents the mean phase value of the wavefront, which does not affect the image quality of the optical system. Z_2 and Z_3 correspond to the tilt terms, which reflect the overall tilt of the wavefront in the x and y directions respectively. It causes the image spot to drift in the image plane. Z_4 corresponds to the defocus item for the longitudinal position. Z_5 and Z_6 correspond to the astigmatism items. Z_7 and Z_8 correspond to the coma items. Z_9 is for the spherical aberration item. From Z_4 to Z_9, these higher order terms reflect the distortion of the wavefront, which expands and blurs the image spot.

As mentioned before, the position of the last lens of the front optics has to be adjusted to find the optimum position. Figure 3.13 shows one of the measured data for the last lens of the front#3 at +30° from the nominal position. The 'Raw Interferogram' in Figure 3.13 shows the measured raw data and the 'Zernike Fit Interferogram' is the fitted result by using the first nine Zernike polynomials in Table 3.2, where the red circle in the figure indicates the range where the fit was performed. The 'Residual' is the residuals between the measured data and the fitted data. The other six subplots represent the corresponding fitted wavefront aberration terms.

Table 3.3 shows the summarised wavefront performances of the front#3 at different positions of the last lens of the front#3, where the increase in coma value is displayed in the order of light green, dark green, light yellow, dark yellow and red. The calculated WFE values are given in units of the operational wavelength λ = 632.8 nm, which is the internal laser wavelength of the Zygo interferometer. Due to the actual operating central wavelength of the SHS system is around 763 nm, the measured optics wavefront

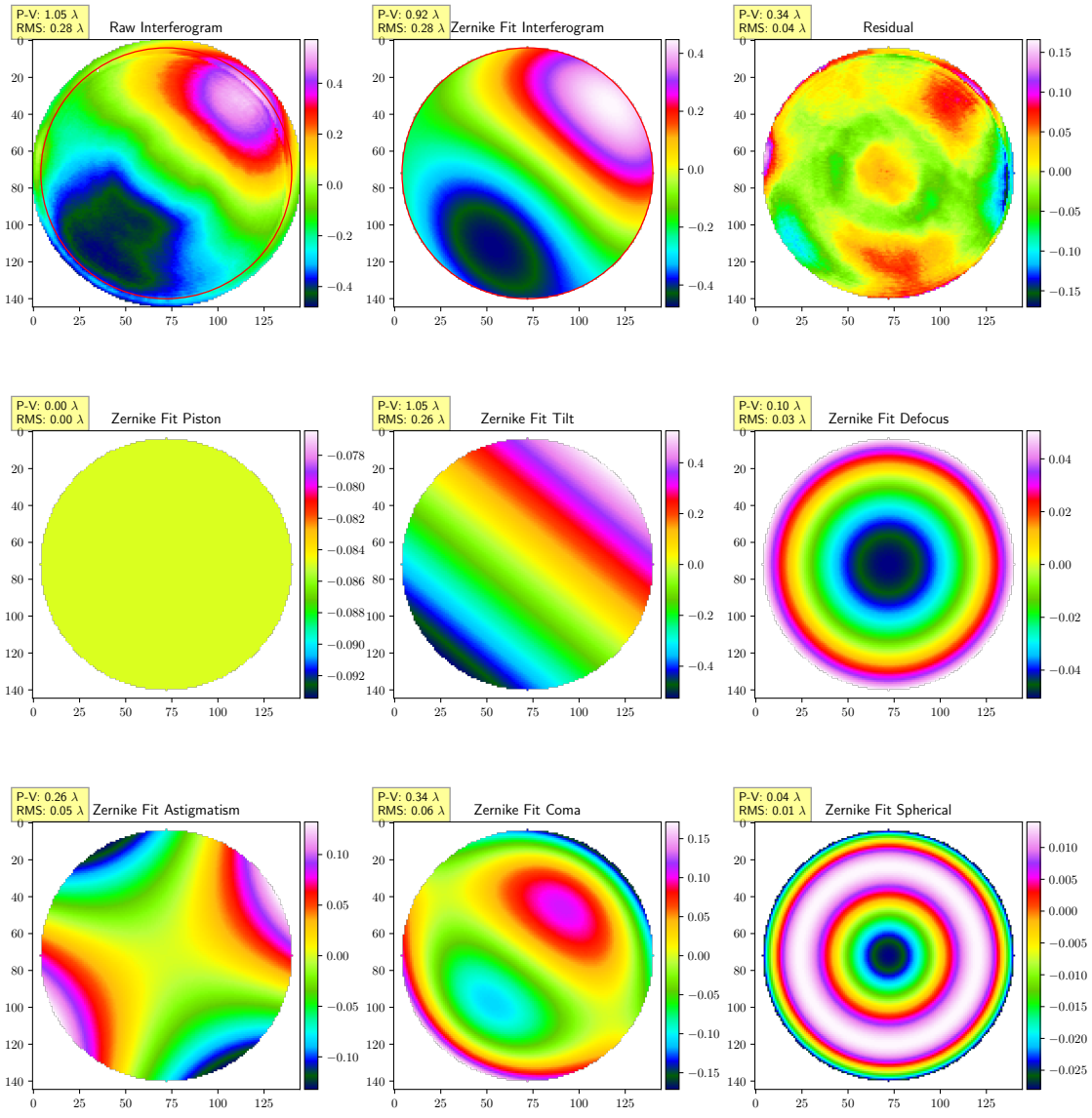

Figure 3.13: The measured wavefront aberrations for the last lens of the front#3 at 30°. The 'Raw Interferogram' is the measured raw data and the 'Zernike Fit Interferogram' is the fitted result by using the first nine Zernike polynomials in Table 3.2, where the red circle in the figure indicates the range where the fit was performed. The 'Residual' is the residuals between the measured data and the fitted data. The other six subplots represent the corresponding fitted wavefront aberration terms. The calculated WFE values are given in units of the operational wavelength λ = 632.8 nm, which is the internal laser wavelength of the Zygo interferometer.

Table 3.3: Calculated wavefront performance of the front#3 sample for different positions of the last lens, where the increase in coma value is displayed in the order of light green, dark green, light yellow, dark yellow and red. As the piston does not affect the image quality of the optical system, it is not included in this table. 'Front#3@00°' represents the nominal position.

Optic	Front#3@-90°		Front#3@-60°		Front#3@-30°		Front#3@00°	
Unit	P-V [λ]	RMS [λ]	P-V [λ]	RMS [λ]	P-V [λ]	RMS [λ]	P-V [λ]	RMS [λ]
Tilt	0.69	0.17	0.85	0.21	0.83	0.21	1.02	0.26
Defocus	0.52	0.15	0.19	0.06	0.09	0.03	0.04	0.01
Coma	0.31	0.06	0.19	0.03	0.19	0.03	0.25	0.05
Astigmatism	0.09	0.02	0.18	0.04	0.24	0.05	0.27	0.05
Spherical Ab.	0.25	0.07	0.16	0.05	0.11	0.03	0.01	0.00
Optic	**Front#3 @30°**		**Front#3 @60°**		**Front#3 @90°**			
Unit	P-V [λ]	RMS [λ]	P-V [λ]	RMS [λ]	P-V [λ]	RMS [λ]		
Tilt	1.05	0.26	1.06	0.27	1.04	0.26		
Defocus	0.10	0.03	0.04	0.01	0.10	0.03		
Coma	0.34	0.06	0.60	0.11	0.86	0.15		
Astigmatism	0.26	0.05	0.17	0.04	0.11	0.02		
Spherical Ab.	0.04	0.01	0.13	0.04	0.20	0.06		

performance is expected to be the worst case scenario. The P-V and RMS values are the fitted Zernike polynomial results, which are not scaled by the interferogram scale factor (ISF). Since the measurement wavefront passed through the front optics twice, it carries twice the actual wavefront error information. Thus the ISF is 0.5 for the front optics.

From Table 3.3, it can be clearly seen that the tilt and coma are the two main dominated wavefront aberrations for the front#3. Due to there is no option to separate the contributions of the piston and tilt introduced by the alignment and setup of the entire Zygo interferometer from the measured WFEs, these two terms are of lesser importance. Our concern is to find the minimal coma. By minimising the coma, we optimise the position of the last lens of the front optics. The optimal position was found at -30° from the nominal position. At this position, the defocus and spherical aberrations are also the smallest.

Astigmatism, defocus and spherical aberrations for the most positions of the last

lens of the front#3 are less than 0.2 λ with RMS less than 0.05 λ, so their contributions to the overall WFEs of the front optics are negligible.

Using the same procedures, we can also find the optimal position of the last lens of the front#1. Once the optimum position of the last lens of the front optics has been found, the off-axis measurements can be performed. Table 3.4 shows the summarised off-axis wavefront performances of the front#1 after finding the optimal position. The scanning angle range is 0.9°. The '$0.0^\circ \pm 0.05^\circ$' represents the initial measurement angle with the uncertainty of 0.05°.

It is clear to see that the coma value first decreases and then increases, where a minimum value can be found around the field angle of '$0.4^\circ \pm 0.05^\circ$'. For the field angle of '$0.5^\circ \pm 0.05^\circ$', it has a smaller coma, but the other wavefront aberrations are larger. Thus the measurement at the field angle of '$0.4^\circ \pm 0.05^\circ$' is considered to be the theoretical on-axis measurement. The field angle of '$0.0^\circ \pm 0.05^\circ$' represents the actual off-axis angle of 0.4°.

Astigmatism aberration increases with field angle compared to the on-axis measurement, which is as expected because astigmatism is an off-axis point wavefront aberration, caused by the obliquity of the incident wavefront relative to the optical surface.

One sees clearly, that spherical aberration for each measurement is smaller than 0.1 λ P-V and 0.02 λ RMS. Thus its contribution to the overall WFEs of the front#1 is negligible.

3.2.2.4 Comparison of ZEMAX Simulation Results with Zygo Measurements

In order to verify the above measurement results, a simulation analysis of the designed front optics configuration is performed by using ZEMAX. Figure 3.14 shows the simulated Zernike fringe coefficients with the different field angles, where the last lens of the front optics is at the designed nominal position and the operating wavelength is 763 nm. It is clearly seen that the tilt and coma dominate the wavefront aberrations of the front optics, which is consistent with Zygo experimental results shown in Table 3.4. Astigmatism, defocus and spherical aberrations are less than 0.3 λ, which means their contribution to the overall WFEs of the front optics is negligible. This is also in line with the measurement results in Section 3.2.2.3.

The coma for the large off-axis angle of 0.4° is 1.15$\pm$0.20 λ in Table 3.4, which corresponds to 0.48$\pm$0.08 λ after applying the ISF factor of 0.5 and the wavelength difference factor of 1.2, which will be discussed later. The simulated coma coefficient is 0.57 λ for the field angle of 3.9° in Figure 3.14. Considering the measurement error, the measured result of 0.48$\pm$0.08 λ is consistent with the simulation result of 0.57 λ.

Table 3.4: Calculated wavefront performance of the front#1 for the off-axis measurement, where the increase in coma value is displayed in the order of light green, dark green, light yellow, dark yellow and red. 'Front#1@00°' represents the optimal position of the front#1, and '0.0° ± 0.05°' represents the initial measurement angle.

Optic	Front#1@ 00°		Front#1@ 00°		Front#1@ 00°	
Field Angle	0.0° ± 0.05°		0.1° ± 0.05°		0.2° ± 0.05°	
Unit	P-V [λ]	RMS [λ]	P-V [λ]	RMS [λ]	P-V [λ]	RMS [λ]
Tilt	0.98	0.25	0.64	0.16	0.52	0.13
Defocus	0.04	0.01	0.02	0.01	0.09	0.03
Coma	1.15	0.20	0.95	0.17	0.76	0.13
Astigmatism	0.27	0.06	0.21	0.04	0.16	0.03
Spherical Ab.	0.07	0.02	0.06	0.02	0.06	0.02
Optic	Front#1@ 00°		Front#1@ 00°		Front#1@ 00°	
Field Angle	0.3° ± 0.05°		0.4° ± 0.05°		0.5° ± 0.05°	
Unit	P-V [λ]	RMS [λ]	P-V [λ]	RMS [λ]	P-V [λ]	RMS [λ]
Tilt	0.96	0.24	0.70	0.17	0.83	0.21
Defocus	0.02	0.01	0.00	0.00	0.03	0.01
Coma	0.56	0.10	0.48	0.09	0.47	0.08
Astigmatism	0.11	0.02	0.19	0.04	0.31	0.06
Spherical Ab.	0.05	0.02	0.04	0.01	0.05	0.01
Optic	Front#1@ 00°		Front#1@ 00°		Front#1@ 00°	
Field Angle	0.6° ± 0.05°		0.7° ± 0.05°		0.8° ± 0.05°	
Unit	P-V [λ]	RMS [λ]	P-V [λ]	RMS [λ]	P-V [λ]	RMS [λ]
Tilt	1.00	0.25	0.90	0.23	0.96	0.24
Defocus	0.21	0.06	0.37	0.11	0.17	0.05
Coma	0.51	0.09	0.69	0.12	0.81	0.14
Astigmatism	0.43	0.09	0.63	0.13	0.78	0.16
Spherical Ab.	0.05	0.01	0.05	0.02	0.06	0.02
Optic	Front#1@ 00°					
Field Angle	0.9° ± 0.05°					
Unit	P-V [λ]	RMS [λ]				
Tilt	0.71	0.18				
Defocus	0.55	0.16				
Coma	0.98	0.17				
Astigmatism	0.96	0.20				
Spherical Ab.	0.07	0.02				

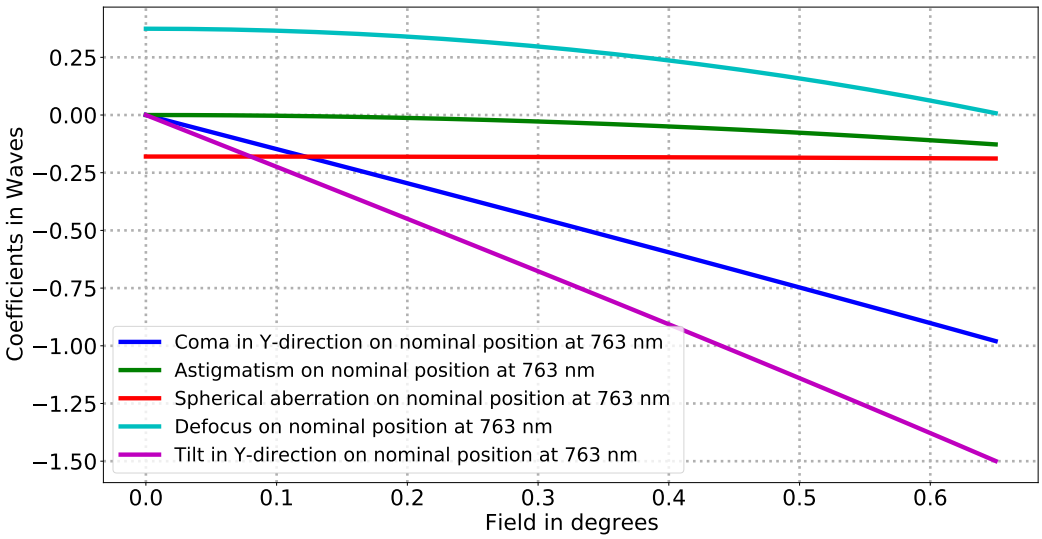

Figure 3.14: Simulated Zernike fringe coefficients for the different field angles, where the last lens of the front optics is at the designed nominal position and the operating wavelength is 763 nm.

Figure 3.15 shows the extreme situation where the last lens of the front optics is rotated away from the nominal position to -8 mm, where the negative symbol indicates the direction of rotation is away from the SHI. The coma increases significantly when the absolute deviation distance increases beyond 3 mm. This gives us a hint that if the coma of the assembled front optics is much larger than the theoretical value, then it means that the last lens of the front optics is not correctly assembled.

Due to the actual mechanical design, the deviation distance after one rotation will not exceed 1 mm. The corresponding simulation results are shown in Figure 3.16. For different field angles, the coma value is always the smallest at the nominal position. Therefore, the strategy of optimally positioning the last lens of the front optics by finding the smallest coma is correct.

3.2.2.5 Discussion and Conclusion

The measured WFEs of the front optics are calculated by using the internal laser wavelength of the Zygo-interferometer (λ = 632.8 nm). However, the SHS system is optimized to operate at a central wavelength of around 763 nm. Due to the difference in wavelengths, the measured WFEs increase by a factor of 1.2, as shown in Figure 3.17, where the two dominated wavefront aberrations are plotted, the coma and tilt. Thus, the measured WFEs of the front optics are expected to be the worst case scenario.

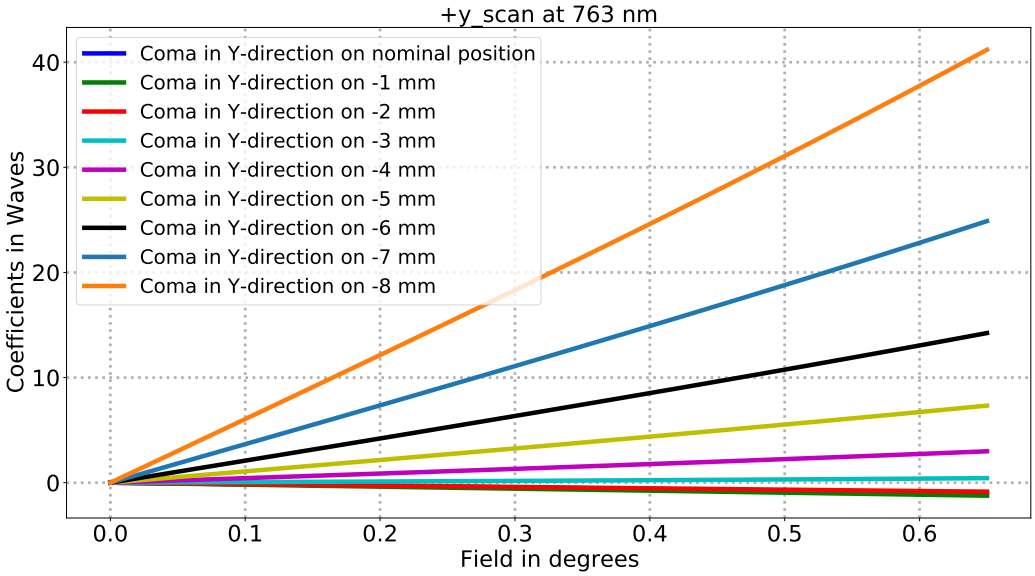

Figure 3.15: Rotating the last lens of the front optics from the nominal position to -8 mm, where the Zernike terms are calculated along the positive Y-field direction and the operating wavelength is 763 nm.

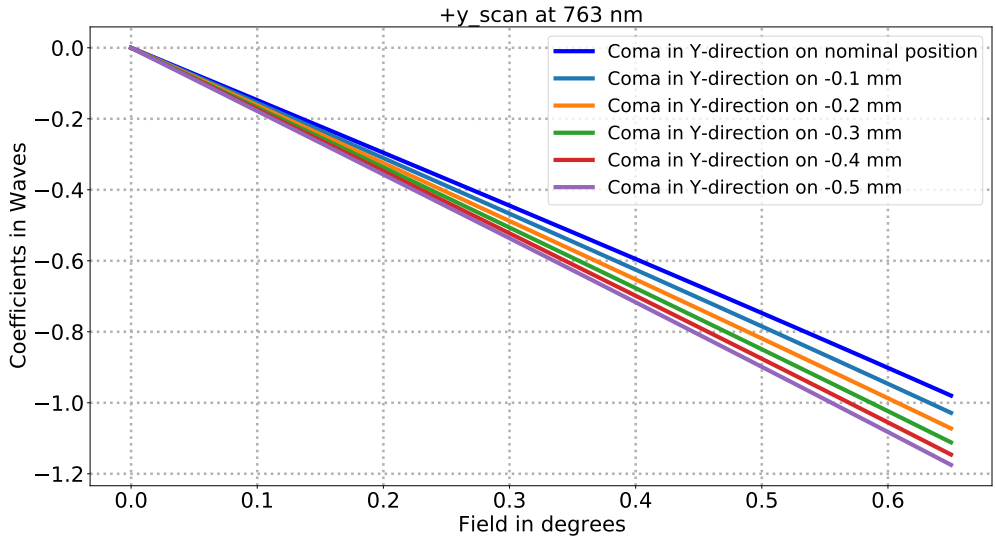

Figure 3.16: Rotating the last lens of the front optics from the nominal position to -0.5 mm, where the Zernike terms are calculated along the positive Y-field direction and the operating wavelength is 763 nm.

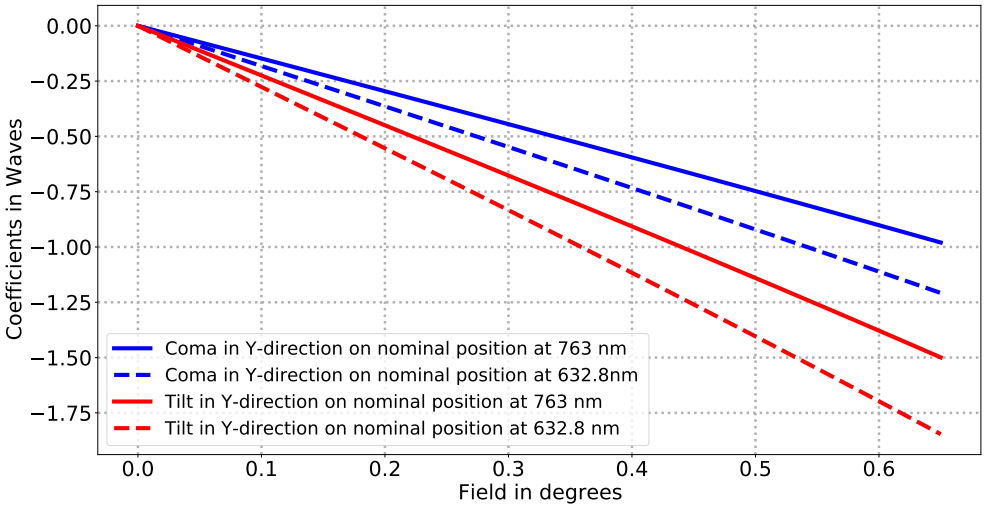

Figure 3.17: The coma and tilt aberration of the front optics at the different operating wavelengths. Due to the difference in wavelengths, the measured WFEs increase by a factor of 1.2.

From the foregoing discussion and the comparison of the two front optics samples at *Gong* (2020), both samples of the front optics showed no significant deviation from theoretical expectations. The front#3 has smaller coma aberration compared to the front#1. And the front#1 has some dust particles on the surface of the lens. Therefore, the front#3 was selected for the QM of the AtmoLITE instrument.

3.2.3 Camera Optics Measurement Setup and Results

3.2.3.1 Camera Optics Test Setup

The optical and mechanical setup used to test the camera optics is shown in Figure 3.18. The beam from the Zygo interferometer was focused by using a transmission sphere with an f-number of 1.5. At 23.8 mm distance from this focal point, the camera optics sample was introduced and formed another focus at the back, in about 7.3 mm distance. The reflective sphere was placed at two times its focal distance from this focal point to ensure that the beam was travelling back the same path to the interferometer.

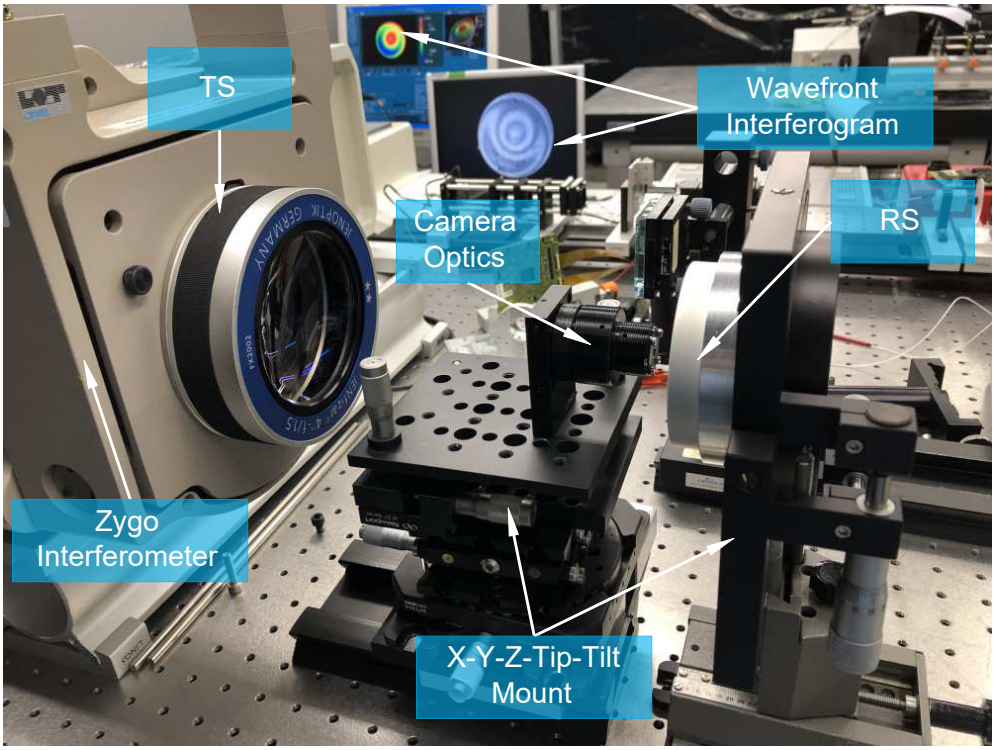

Figure 3.18: Measurement setup for the camera optics with the old optics design.

3.2.3.2 Alignment and Measurement Procedures

The objective of the alignment is to make the camera optics, Zygo, TS and RS position at a common optical axis. For the camera optics, it is crucial to find two foci positions, namely the front foci and back foci of the camera optics. The alignment and measurement procedures are as follows:

1) Insert the TS into the accessory receptacle on the Zygo interferometer. Gently tighten the thumbscrews.

2) Press the 'Align/View' button on the remote control to switch to the Align mode.

3) Monitor the display screen and align the tip and tilt screws of the TS to center the brightest spot on the crosshairs so that the optical center of the TS is concentric with the optical aperture center of the Zygo interferometer.

4) Use a reflective mirror or paper to find the front foci position as the light beam is focused by the TS.

5) Place the RS or reflective mirror at the front foci position to find the first cat's-eye position. This step is to make the RS or reflective mirror and Zygo reach coaxial.

6) Place the camera optics sample at the designed object distance from this foci position.

7) Use the reflective mirror or paper to find the back foci position of the camera optics.

8) Adjust the reflective mirror and camera optics to find the second cat's-eye position. This step is to make the RS or reflective mirror, Zygo and camera optics reach coaxis.

9) To place the RS at two times its focal distance from the back foci position.

10) Adjust the X-Y-Z-Rotation translation stage and the tip-tilt mount of the camera optics to minimize the number of interference fringes. The transmitted wavefront interferogram of the camera optics will be obtained.

11) Tilt the camera optics for the different field angles to evaluate the off-axis WFEs.

3.2.3.3 Measurement Results

The off-axis WFE measurements of the camera#1 are summarised in Table 3.5. It is clearly seen that the spherical aberration keeps almost constant within the measurement uncertainty for the different field angles. Defocus and coma are another two main aberrations contributed to the overall WFE.

The off-axis WFE measurements of the camera#2 are summarised in Table 3.6. Spherical aberration also keeps almost constant within the measurement uncertainty for the different off-axis angles. An increased astigmatism is likely caused by non-ideal alignment of the coaxial optical path.

3.2.3.4 Discussion and Conclusion

Figure 3.19 shows the simulated Zernike fringe coefficients of the camera optics for the different object heights while the operating wavelength is 763 nm. The spherical aberration is almost constant for the different object heights, which is consistent with the trend presented in Table 3.5 and Table 3.6. In addition to the tilt term, coma and defocus are another two main aberrations, which also satisfy the measured trend. The reason why the WFE values in the simulation results are higher than the WFE values in the measurement results is that the simulation results overestimate the WFE values because of the lack of a valid merit function to optimize the old optical system when

Table 3.5: Calculated wavefront performance of the camera#1 for the off-axis measurements, where '$0.0° \pm 0.05°$' represents the initial measurement angle. The spherical aberration is indicated in green because it is the dominant WFE of the camera optics.

Optic	Camera#1		Camera#1		Camera#1	
Field Angle	$0.0° \pm 0.05°$		$0.1° \pm 0.05°$		$0.2° \pm 0.05°$	
Unit	P-V [λ]	RMS [λ]	P-V [λ]	RMS [λ]	P-V [λ]	RMS [λ]
Tilt	0.17	0.04	0.22	0.05	0.37	0.09
Defocus	0.20	0.06	0.41	0.12	0.42	0.12
Coma	0.28	0.05	0.31	0.05	0.36	0.06
Astigmatism	0.04	0.01	0.07	0.01	0.12	0.02
Spherical Ab.	0.24	0.07	0.22	0.06	0.21	0.06
Optic	Camera#1		Camera#1		Camera#1	
Field Angle	$0.3° \pm 0.05°$		$0.4° \pm 0.05°$		$0.5° \pm 0.05°$	
Unit	P-V [λ]	RMS [λ]	P-V [λ]	RMS [λ]	P-V [λ]	RMS [λ]
Tilt	0.50	0.13	0.20	0.05	0.41	0.10
Defocus	0.25	0.07	0.32	0.09	0.20	0.06
Coma	0.41	0.07	0.45	0.08	0.46	0.08
Astigmatism	0.15	0.03	0.20	0.04	0.22	0.05
Spherical Ab.	0.20	0.06	0.18	0.05	0.17	0.05

Table 3.6: Calculated wavefront performance of the camera#2 for the off-axis measurements, where '$0.0° \pm 0.05°$' represents the initial measurement angle. The spherical aberration is indicated in green because it is the dominant WFE of the camera optics.

Optic	Camera#2		Camera#2		Camera#2	
Field Angle	$0.0° \pm 0.05°$		$0.1° \pm 0.05°$		$0.2° \pm 0.05°$	
Unit	P-V [λ]	RMS [λ]	P-V [λ]	RMS [λ]	P-V [λ]	RMS [λ]
Tilt	0.71	0.18	0.66	0.17	0.39	0.10
Defocus	0.29	0.08	0.28	0.08	0.71	0.21
Coma	0.29	0.05	0.31	0.06	0.22	0.04
Astigmatism	0.12	0.03	0.18	0.04	0.23	0.05
Spherical Ab.	0.28	0.08	0.29	0.09	0.26	0.08
Optic	Camera#2		Camera#2		Camera#2	
Field Angle	$0.3° \pm 0.05°$		$0.4° \pm 0.05°$		$0.5° \pm 0.05°$	
Unit	P-V [λ]	RMS [λ]	P-V [λ]	RMS [λ]	P-V [λ]	RMS [λ]
Tilt	0.58	0.15	0.40	0.10	0.78	0.19
Defocus	0.10	0.03	0.75	0.22	0.70	0.20
Coma	0.13	0.02	0.09	0.02	0.02	0.00
Astigmatism	0.28	0.06	0.33	0.07	0.37	0.08
Spherical Ab.	0.26	0.08	0.23	0.07	0.21	0.06

creating a separate camera optics ZEMAX file. However, the trend of the WFEs can be used to evaluate whether the measured camera optics meets the expectations.

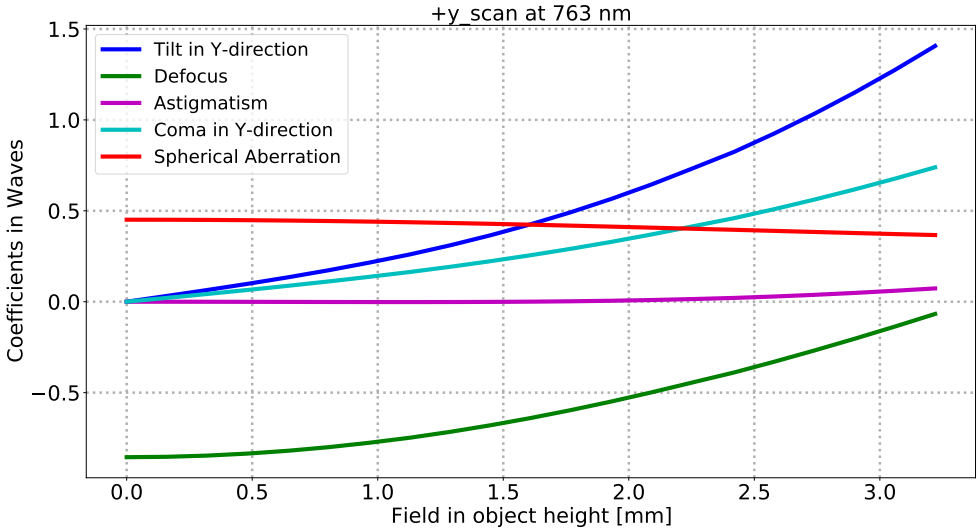

Figure 3.19: Simulated Zernike fringe coefficients for the different object heights of the camera optics, where the Zernike terms are calculated along the positive Y field direction, and the operating wavelength is 763 nm.

The camera#1 and camera#2 provide similar wavefront performances. The camera#1 has a slightly smaller coma on average. Due to the inner lens surfaces of the camera#1 was contaminated by the dust, the camera#2 was selected for the QM of the AtmoLITE instrument.

3.3 Wavefront Error Measurements on the Camera Optics for the FM

For the FM of the AtmoLITE instrument, it uses a newly designed front and camera optics configuration and a different Littrow wavelength compared to the QM, as mentioned in Section 3.1. However, the strong converging backreflection of the front optics was found when measuring with the Zygo interferometer. The main suspect candidate for this is probably the anti-reflection coating on the lenses of the front optics, which operates at around 765 nm instead of 632.8 nm. Therefore, the Zygo measurement was not available for the front optics of the FM. As an alternative, the imaging performance of the front optics was checked by utilizing a pinhole light source setup, which will be introduced in Chapter 4.

This section presents the WFE results for three camera optics samples of the FM: the camera#2, camera#3 and camera#4. The camera#1 was assembled into the prototype with the new optical design.

3.3.1 FM' s Camera Optics Test Setup

The optical and mechanical setup used to test the camera optics with the new optical design is shown in Figure 3.20. The beam from the Zygo interferometer was focused by using the f/1.5 transmission sphere. At 29.8 mm distance from this focal point the camera optics sample was introduced and formed another focus at the back, in about 4.2 mm distance. The reflective sphere was placed at two times its focal distance from this focal point to ensure that the beam was travelling back the same path to the interferometer.

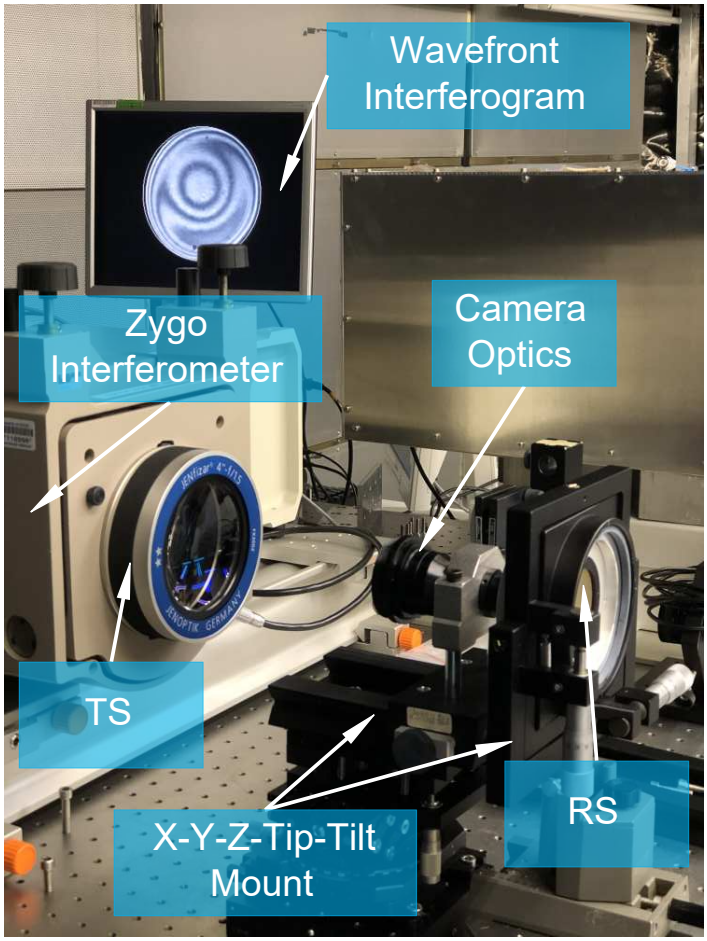

Figure 3.20: Measurement setup for the camera optics with the new optics design.

3.3.2 Measurement Results

The comparison of the measurement data of the three camera optics camera#2, camera#3 and camera#4 is given in Table 3.7. In addition to the tilt term, spherical aberration is the dominant WFE of the camera optics.

Table 3.7: Calculated wavefront performance of the camera#2, camera#3 and camera#4 of the FM, where the increase in spherical aberration and coma is shown in the order of light green, dark yellow and red.

Optic	Camera#2		Camera#3		Camera#4	
Unit	P-V [λ]	RMS [λ]	P-V [λ]	RMS [λ]	P-V [λ]	RMS [λ]
Tilt	1.00	0.25	0.73	0.18	0.60	0.15
Defocus	0.18	0.05	0.20	0.06	0.17	0.05
Coma	0.12	0.02	0.73	0.13	0.32	0.06
Astigmatism	0.08	0.02	0.21	0.04	0.17	0.03
Spherical Ab.	0.39	0.12	0.52	0.15	0.55	0.16

The overall increase in the coma and spherical aberration of the camera#3 might be due to inadequate alignment of the lenses during assembly. The camera#2 has the smallest spherical aberration. Table 3.8 gives the summarised measurement data of the camera#2 for the off-axis measurements. The corresponding data for the camera#3 is given in Appendix A.2. Spherical aberration stays constant within the measurement uncertainty for different off-axis angles.

3.3.3 Discussion and Conclusion

Figure 3.21 shows the simulated Zernike fringe coefficients of the camera optics of the FM for the different object heights while the operating wavelength is 632.8 nm. The large defocus values in the simulation results are caused by the field curvature of the camera optics. The localization plane in our new system is not a strict plane because of the field curvature of the front optics, so the camera optics is designed to compensate for this field curvature, which introduces the large defocus errors in our simulations.

The spherical aberration is about 0.12 λ on average in the simulation results in Figure 3.21. The corresponding measured spherical aberration is 0.35$\pm$0.10 λ on average in Table 3.8. Dividing by the ISF factor of 0.5, the actual spherical aberration is 0.17$\pm$0.05 λ. This is approximately equal to the simulation value of 0.12 λ with 2% uncertainty. This confirms the correctness of our measurements and the correct assembly

Table 3.8: Calculated wavefront performance of the camera#2 of the FM for the off-axis measurements, where '$0.0° \pm 0.05°$' represents the initial measurement angle. The spherical aberration is indicated in green because it is the dominant WFE of the camera optics.

Optic	Camera#2		Camera#2		Camera#2	
Field Angle	$0.0° \pm 0.05°$		$0.1° \pm 0.05°$		$0.2° \pm 0.05°$	
Unit	P-V [λ]	RMS [λ]	P-V [λ]	RMS [λ]	P-V [λ]	RMS [λ]
Tilt	1.00	0.25	0.58	0.14	1.08	0.27
Defocus	0.18	0.05	0.35	0.10	0.60	0.17
Coma	0.12	0.02	0.20	0.04	0.18	0.03
Astigmatism	0.08	0.02	0.07	0.01	0.08	0.02
Spherical Ab.	0.39	0.12	0.37	0.11	0.33	0.10
Optic	Camera#2		Camera#2		Camera#2	
Field Angle	$0.3° \pm 0.05°$		$0.4° \pm 0.05°$		$0.6° \pm 0.05°$	
Unit	P-V [λ]	RMS [λ]	P-V [λ]	RMS [λ]	P-V [λ]	RMS [λ]
Tilt	0.81	0.20	0.97	0.24	0.67	0.17
Defocus	0.42	0.12	0.43	0.12	0.59	0.17
Coma	0.22	0.04	0.25	0.04	0.37	0.07
Astigmatism	0.09	0.02	0.09	0.02	0.09	0.02
Spherical Ab.	0.36	0.11	0.35	0.10	0.36	0.11
Optic	Camera#2		Camera#2		Camera#2	
Field Angle	$0.8° \pm 0.05°$		$1.0° \pm 0.05°$		$1.2° \pm 0.05°$	
Unit	P-V [λ]	RMS [λ]	P-V [λ]	RMS [λ]	P-V [λ]	RMS [λ]
Tilt	1.00	0.25	0.64	0.16	0.77	0.19
Defocus	0.47	0.14	0.14	0.04	0.19	0.05
Coma	0.38	0.07	0.45	0.08	0.55	0.10
Astigmatism	0.08	0.02	0.09	0.02	0.05	0.01
Spherical Ab.	0.32	0.09	0.32	0.09	0.31	0.09
Optic	Camera#2					
Field Angle	$1.4° \pm 0.05°$					
Unit	P-V [λ]	RMS [λ]				
Tilt	0.60	0.15				
Defocus	0.12	0.03				
Coma	0.54	0.10				
Astigmatism	0.04	0.01				
Spherical Ab.	0.27	0.08				

of the camera#2. Based on the above results, the camera#2 was utilised for the FM of the AtmoLITE instrument.

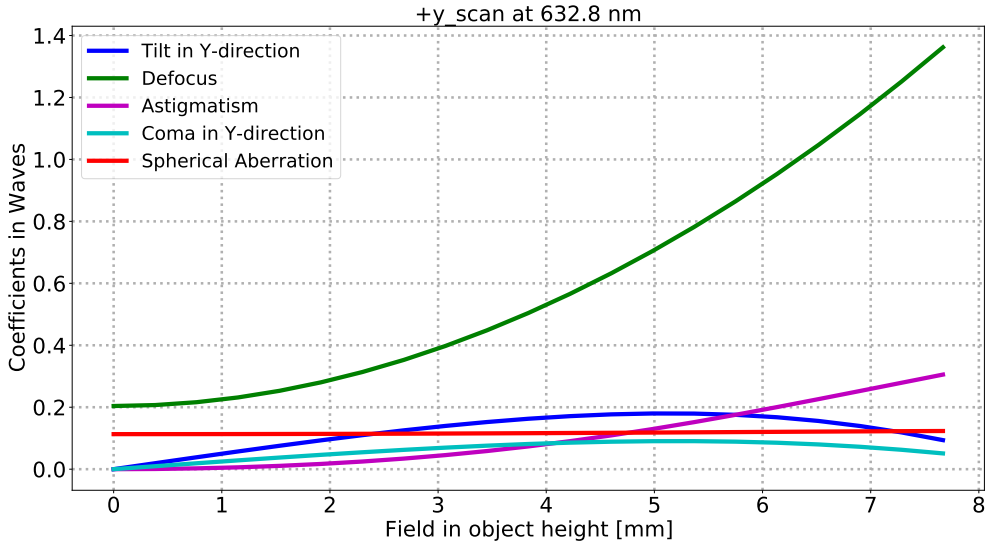

Figure 3.21: Simulated Zernike fringe coefficients for the different object heights for the camera optics of the FM, where the Zernike terms are calculated along the positive Y field direction, and the operating wavelength is 632.8 nm. Note that the simulated Zernike fringe coefficients are calculated for the field points from the object plane. For the camera optics, the field is defined as the object height. However, the off-axis measurements are defined for the off-axis angles. As the detailed optical setup of the internal Zygo optics is not available, it can not be directly scaled between each other.

3.4 Alternative Version of the Glass Materials for the AtmoLITE Instrument

In the early stages of the progress of the AtmoLITE project, it was necessary to find an alternative version of the glass materials for the AtmoLITE instrument, where all lens materials for the front and camera optics should be selected from the Chinese glass material catalogue, because the procurement time for the European or Japanese glasses was too long and might delay the progress of the whole project. At that moment, the almost final version of the optical design (not the real final version for the prototype and FM of the AtmoLITE) was used for optimization analysis to select an alternative version.

The optimization strategy is to determine the radii of the lens surfaces, the materials of the lenses and the distance between two adjacent lenses as variables, while keeping the thickness of the lens, the SHI and other environment parameters as fixed initial values. The RMS wavefront, OPD and spot size are used as optimization criteria. All Chinese substituted glasses data are sought from the CDGM catalogues (*CDGM GLASS CO.,LTD*, 2018).

Table 3.9 summarizes the substituted Chinese glasses of the front and camera optics for the AtmoLITE instrument. All glasses materials from the SCHOTT and OHARA have been substituted by the glasses materials from the CDGM. A detailed comparison of the optical performance of the two glass versions is presented in Appendix A.3

Table 3.9: Substituted Chinese glasses of the front and camera optics for the AtmoLITE

		Original lens		Substitute lens	
		Glass	Manufacturer	Glass	Manufacturer
Front optics	Lens1	N-SK16	SCHOTT	H-ZK9A	CDGM
	Lens2	S-BAL35	OHARA	H-ZK3	CDGM
	Lens3	S-NPH3	OHARA	H-ZF88	CDGM
	Lens4	N-LASF44	SCHOTT	H-ZLAF50D	CDGM
Camera optics	Lens1	N-PSK3	SCHOTT	H-BAK4	CDGM
	Lens2	S-BAL35	OHARA	H-ZK3	CDGM
	Lens3	S-BSM2	OHARA	H-ZK50	CDGM

3.5 Chapter Summary

This chapter focuses on the wavefront error measurements of the front optics and camera optics of the QM and FM of the AtmoLITE instrument. For the front optics, the coma aberration is the dominating Zernike polynomial that gives the most contribution to the overall WFEs. The strategy to find the optimum position of the last lens of the front optics is to obtain the minimal coma during the alignment. For the camera optics, apart from the tilt and defocus aberrations, the spherical aberration contributes the most to the overall WFEs. The large defocus value of the camera optics in the simulation results is due to the fact that the camera optics is designed to compensate for the field curvature of the front optics, resulting in the localization plane in our new system not being a

strictly plane. The measured WFEs satisfy the simulated WFEs within the measurement uncertainty.

Finally, the front#3 and the camera#2 with the old optical design were selected for the QM. The camera#2 with the new optical design was utilised for the FM. In addition, an alternative version of the glass materials for the AtmoLITE instrument was introduced, where the all lens materials for the front and camera optics were selected from the Chinese glass material catalogues.

Chapter 4

Optical Performance Characterization during and after the SHS Glueing for the AtmoLITE Instrument

Once the assembled front and camera optics are selected, it will be used combining with the AtmoLITE calibration unit (ACU) as the imaging system to glue and assemble the SHS. The ACU, a variant of the collimation system designed by another PhD student Oliver Wroblowski (*Wroblowski*, 2022), provides a light stimulus similar to a natural atmospheric scene observed by the satellite instrument. The ACU is used for the AtmoLITE as the light source to provide a homogeneous aperture illumination and angular illumination covering the full aperture and FOV of the instrument.

As mentioned in Chapter 3 , the distance between the last lens of the front optics and the SHI, the distance between the SHI and the camera optics and the distance between the camera optics and the detector should be adjusted to obtain the optimum performance of the SHS system during the SHS integration. This chapter mainly presents the optical performance characterization during this process, including verification of the imaging performance of the SHS system in the ambient (instrument operating at standard atmospheric pressure) and vacuum environments (instrument operating under vacuum), filter transmission curve measurements, etc.

4.1 Alignment of the Front and Camera Optics during the SHS Integration

Section 3.3 presented that the Zygo measurement was not available for the front optics of the FM due to the strong converging back-reflection. Therefore, a pinhole light source setup was built to adjust the position of the last lens of the front optics to find the optimum position with the smallest image point, in which the pinhole light source provides an approximately collimated light beam with a limited divergence angle.

4.1.1 Alignment Procedures of the Pinhole Setup

The function of the pinhole setup is to collimate and expand the light beam from a point source (in our case that a pinhole with a diameter of 25 μm) to a virtual infinity where the beam diameter exceeds 75 mm. Figure 4.1 shows the pinhole alignment setup with a shearing plate collimation tester and a GSENSE detector.

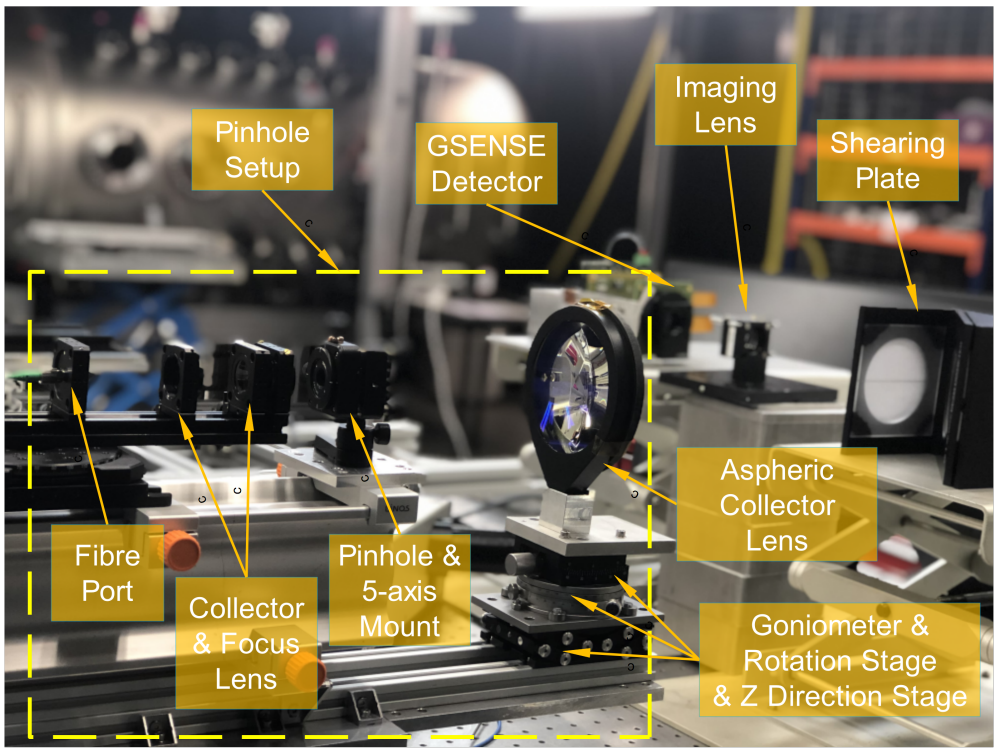

Figure 4.1: Pinhole alignment setup with a shearing plate collimation tester and a GSENSE detector.

The alignment procedures of the pinhole setup are as follows:

1) Create a laser focus generator. This step is to use an aspheric collector lens L_1 with a focal length of $f_1 = 75$ mm to collimate the light beam from the fibre port. Then the focus lenses are used to focus the collimated beam into the air to form a focal point mid-air.

2) Place an aspheric collector lens L_2 with a focal length of $f_2 = 200$ mm on the alignment stage. Tip and tilt the aspheric collector lens L_2 with the goniometer and rotation stage so that it is approximately perpendicular to the optical axis defined by the central axis of the laser focus generator created in the step 1. Adjust the height of the aspheric lens L_2 with Z-direction stage to reach coaxial with the laser focus generator.

3) Adjust the distance between the laser focus generator and the aspheric collector lens L_2 to make the focal point created by the laser focus generator overlapped with the virtual foci of the L_2. A shearing plate collimation tester and a starlight camera are utilised to observe the corresponding shearing interferogram which is used to evaluate the wavefront curvature exiting from the L_2.

4) Adjust the relative positions of the laser focus generator, the L_2 and the shearing plate until a clear shearogram is observed. Then replace the starlight camera by the GSENSE detector which is more difficult to handle, but has a larger photoelectric area to capture the shearogram more completely. In order to verify that the detector is focused on the reference plane of the shearing plate, an infrared detector card is put on the reference plane as the object image. Figure 4.2 shows the recorded image of the infrared detector card after adjusting the position of the imaging lens between the shearing plate and the GSENSE detector, where the letters can be clearly distinguished.

5) Once the quasi-parallel shear interference fringes have been obtained, the pinhole is placed in the focus position of the laser focus generator. During this process, the interferogram will disappear as the pinhole blocks the optical path. Use the five-axis kinematic mount to align the pinhole until the interference fringes come back. Figure 4.3 shows the measured quasi-parallel shearogram after aligning the pinhole, where the black horizontal line near the row 705 is the image of the reference line of the shearing plate. The curved fringe shape mainly arises from the wavefront aberration, especially the spherical aberration of the whole pinhole setup, because the focus generated by the laser focus generator is not an ideal point. Only one aspheric collimator can not suppress and correct all wavefront aberrations. But the quality of the recorded shearogram is still sufficient to evaluate the tilt angle of the fringes with respect to the reference line.

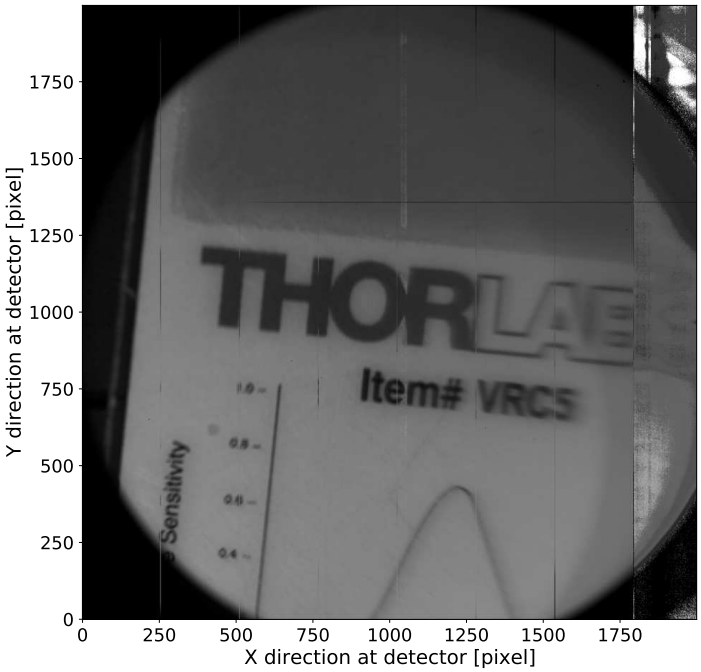

Figure 4.2: The recorded image of the infrared detector card.

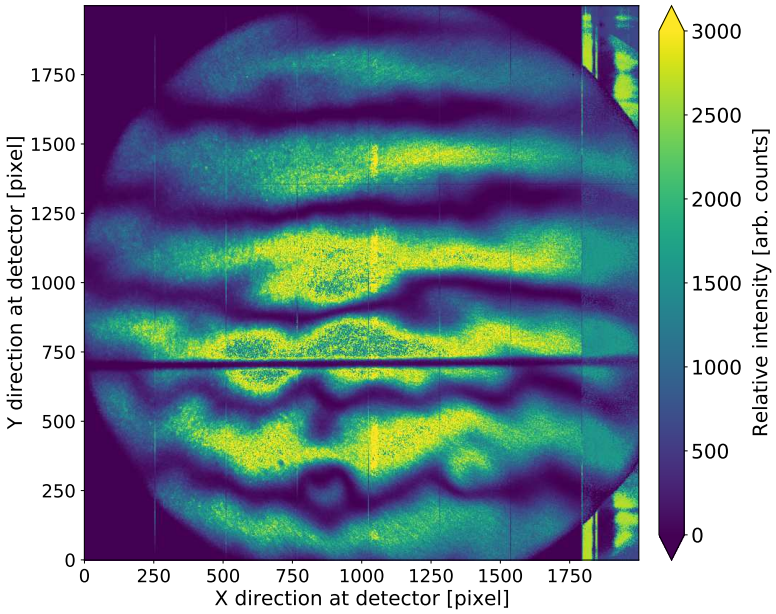

Figure 4.3: Measured shearogram after inserting the pinhole, where the black horizontal line near the row 705 is the image of the reference line of the shearing plate.

In order to evaluate the virtual distance of the point source provided by the pinhole setup, the orientation angle of the shearogram fringe should first be estimated based on the principal component analysis (PCA) method, where the PCA method gives the orientation angle of the points within the contour lines of the shearogram (*Ntokas*, 2022). Figure 4.4 shows the estimated orientation angles of the reference line and shearogram in Figure 4.3, where the tilt angle of the reference line is about -0.641°, and the tilt angle of the shearogram fringe is about -1.414° $\pm$ 0.699°. Note that the negative sign is defined with respect to the X-direction of the detector and the uncertainty $\pm$0.699° is the standard deviation of the individual fringe estimations in one image.

Therefore, the actual orientation angle of the shearogram fringe is about 0.773° $\pm$ 0.699° with respect to the reference line of the shearing plate. Based on the calculated orientation angle of the shearogram fringes, the radius of curvature of the wavefront exiting from the pinhole setup can be estimated according to the method proposed by Riley and Gusinow (*Riley and Gusinow*, 1977). The radius of curvature of the wavefront R is calculated by:

$$R = \frac{s * d}{\lambda * tan(\Phi)}, \tag{4.1}$$

where λ is the operating wavelength, Φ is the fringe tilt angle of the shearogram, d is the fringe spacing perpendicular to the shear direction and s is the shear distance between two overlapped wavefronts.

The shear value s is estimated by:

$$s = t * \frac{sin(2\alpha)}{(n^2 - \sin^2\alpha)^{\frac{1}{2}}}, \tag{4.2}$$

where α is the angle of incidence onto the shearing plate, n is the refractive index of the shear plate and t is the thickness of the shearing plate.

For our measurement setup, the shearing plate is made by the fused silica so that $n = 1.454$. The thickness of $t = 13$ mm and the incident angle of $\alpha = 45°$ are provided by the manufacturer Thorlabs. Substitute these values into the Equation 4.2, the lateral shear distance s is:

$$s = 13\ mm * \frac{sin(2 * 45°)}{(1.454^2 - \sin^2 45°)^{\frac{1}{2}}} = 10.23\ mm. \tag{4.3}$$

The fringe spacing in Figure 4.3 is about 285 pixels. Due to the magnification factor of the imaging lens is 0.57 and the pixel width is 11 μm, thus the actual fringe spacing is:

$$d = \frac{285 * 11\ \mu m}{0.57} = 5500\ \mu m = 5.5\ mm. \tag{4.4}$$

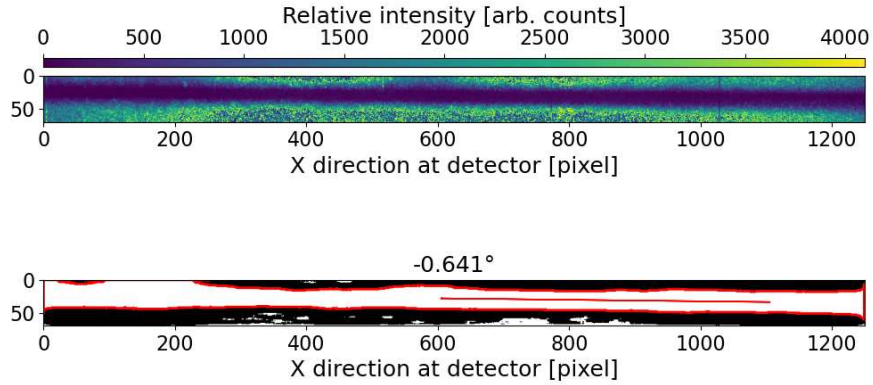

(a) Estimated tilt angle of the reference line. The top subplot shows the original image, and the bottom subplot shows the tilt angle of the fringes calculated using the PCA method, where the red lines represent the fringe shape identified using the threshold filter

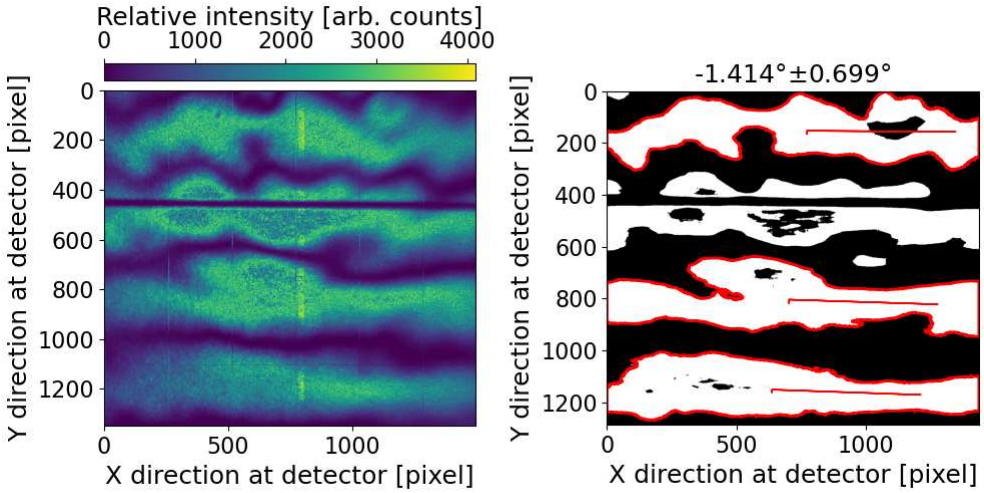

(b) Estimated tilt angle of the shearogram fringes. The left subplot shows the original image, and the right subplot shows the tilt angle of the fringes calculated using the PCA method, where the red lines represent the fringe shape identified using the threshold filter

Figure 4.4: Estimated orientation angles of the reference line and shearogram based on the PCA method.

The operating wavelength λ is at 762 nm. The orientation angle of the shearogram is about $0.773^\circ \pm 0.699^\circ$ based on the PCA calculation. Substitute these values into the

Equation 4.1, the radius of curvature of the wavefront exiting from the pinhole setup is:

$$R = \frac{(10.23 * 10^{-3})\ m * (5.5 * 10^{-3})\ m}{(762 * 10^{-9})\ m * tan(0.773^{\circ})} = 5473.9\ m. \tag{4.5}$$

For the worst case of $\Phi = 0.773^{\circ} + 0.699^{\circ} = 1.472^{\circ}$, the corresponding radius of curvature of the wavefront is 2874.1 m, which indicates that the pinhole setup is sufficient to be used as a virtual infinite point source.

4.1.2 Alignment Procedures of the Front Optics and Camera Optics

The purpose of aligning the front optics is to minimize the size of the spot imaged by the pinhole setup on the detector array by adjusting the distance between the last lens of the front optics and the SHI. And the object of aligning the camera optics is to achieve the desired contrast or visibility of the entire SHS system by adjusting the distance between the SHI and the camera optics and the distance between the camera optics and the detector.

Figure 4.5 shows the measurement setup for aligning the front and camera optics during the SHS integration. The instrument was mounted on the X-Y-Z-Rotation translation stage and a tilt mount platform. The ACU mounted on the Bosch Rexroth profile stage and the pinhole setup mounted on the lab jack were placed vertically on either side of the instrument.

The alignment procedures are as follows:

1) Adjust the position of the central axis of the instrument, the ACU and the pinhole setup so that the three are equal in height and coaxial.

2) First point the instrument to the ACU and align the camera optics to make the blurred interferogram clear. This step brings the camera optics into focus.

3) Then rotate the instrument by 90° and point it to the pinhole setup. Adjust the last lens of the front optics to minimise the size of the spot imaged by the pinhole setup on the detector array.

4) Rotate the instrument back by 90° and point it toward the ACU. The laser wavelength is tuned to approximately 759.5 nm, which corresponds to a spatial frequency slightly above our maximum expected frequency. The camera optics is then adjusted to obtain the visibility map of over 60% for the whole regions of interest (ROI). According to the simulation analysis of another PhD student Oliver Wroblowski who takes the consideration of the optical design parameters of the AtmoLITE instrument's FM in his thesis work (*Wroblowski*, 2022), the expected visibility of the

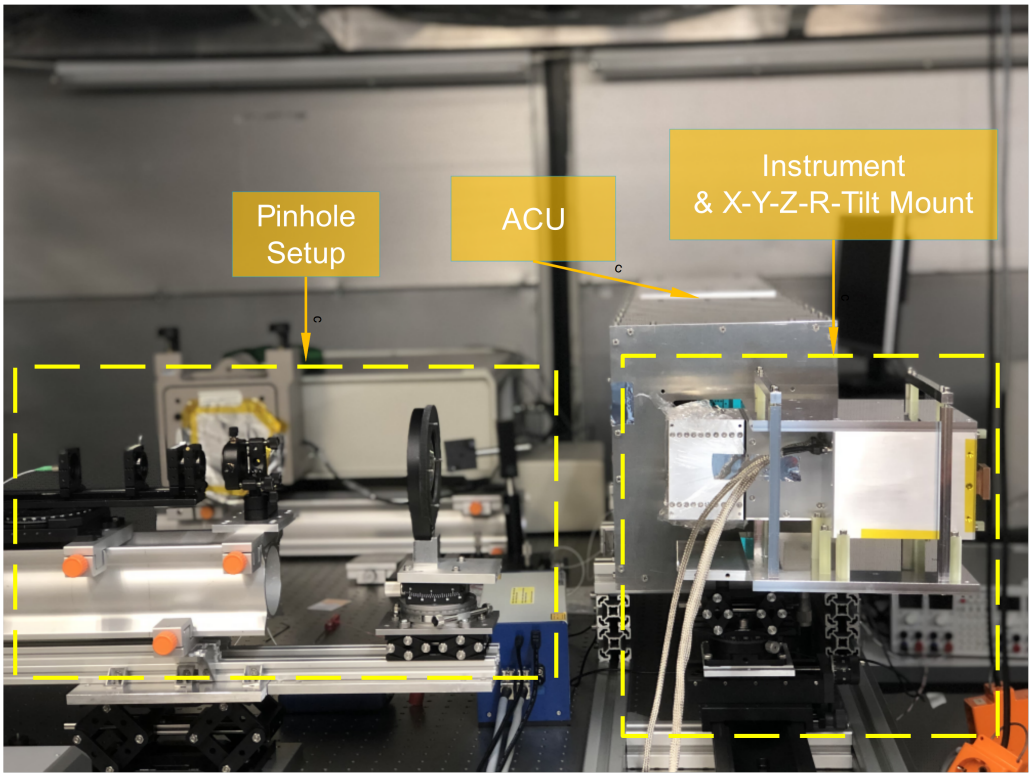

Figure 4.5: Measurement setup for aligning the front and camera optics.

central region of the interferogram is lower than the expected visibility of the two edges for this high spatial frequency. And for high spatial frequencies near the maximum expected frequency, the expected visibility is about 60% in the middle and about 70% in the edges. For low spatial frequencies, the expected visibility of most regions of the ROI is above 80%, and the expected visibility of the central area of the interferogram should be higher than that of the two edges. Therefore, this step is to find a balance between the visibility of the edges and the middle of the image.

5) Repeat the step 3 and step 4 several times to reduce the systematic error during alignment and find the optimum positions of the front optics and camera optics.

6) Scan the entire designed wavelength range of the instrument to check the corresponding visibility map of the interferogram. Ensure that the visibility map follows the expected trend for all spatial frequencies within the measurement range.

7) Finally, the position of the front optics and camera optics are fixed into the barrel and fixture frame.

4.1.3 Alignment Results for the Front Optics of the FM

Figure 4.6 shows the final minimised size of the spot imaged by the pinhole setup, where Figure 4.6(a) displays the output image on the detector array and Figure 4.6(b) shows the two cross slices at the brightest point of the spot image. The measurement mode of the detector is HDR_LowGain which the output frames are obtained in the high dynamic range (HDR) mode with a low gain factor.

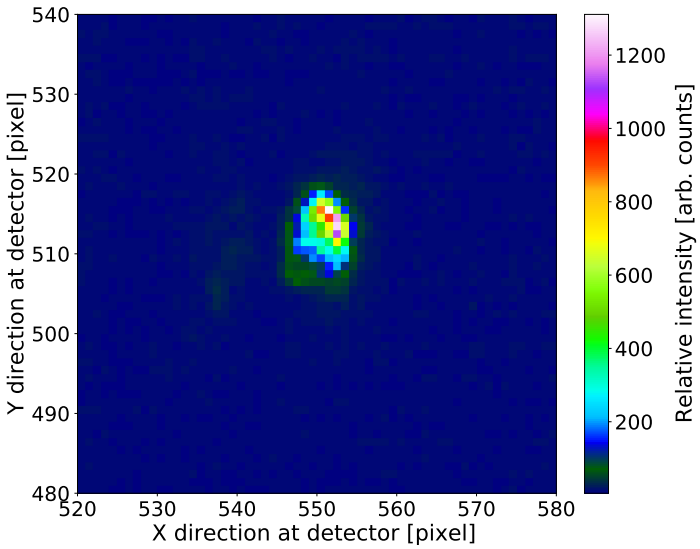

(a) The output image on the detector array

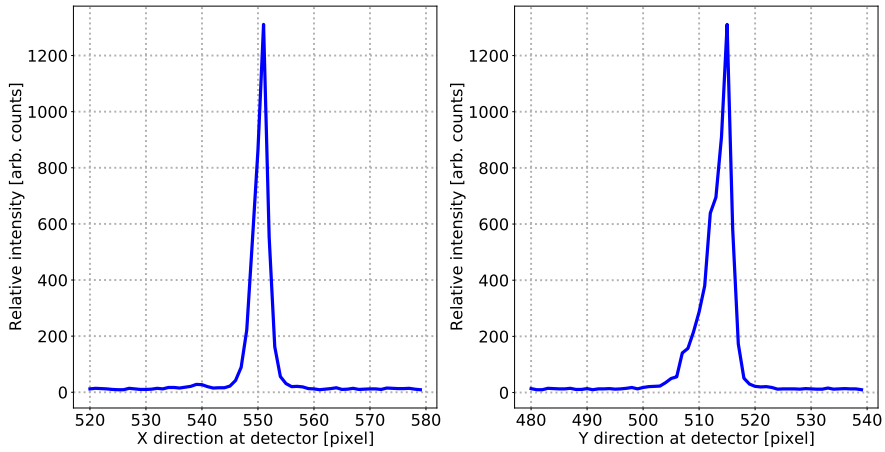

(b) The two cross slices at the brightest point

Figure 4.6: The spot imaged by the pinhole setup on the detector and the corresponding two cross slices at the brightest point of the spot image.

One sees clearly, that the full size of the spot imaged by the pinhole setup is about 10 pixels and the corresponding full width at half maximum (FWHM) is 4 to 6 pixels. Figure 4.7 shows the simulated spot diagrams of the FM at the field points of (0.00°, 0.00°) and (0.65°, 0.65°) in the ambient environment.

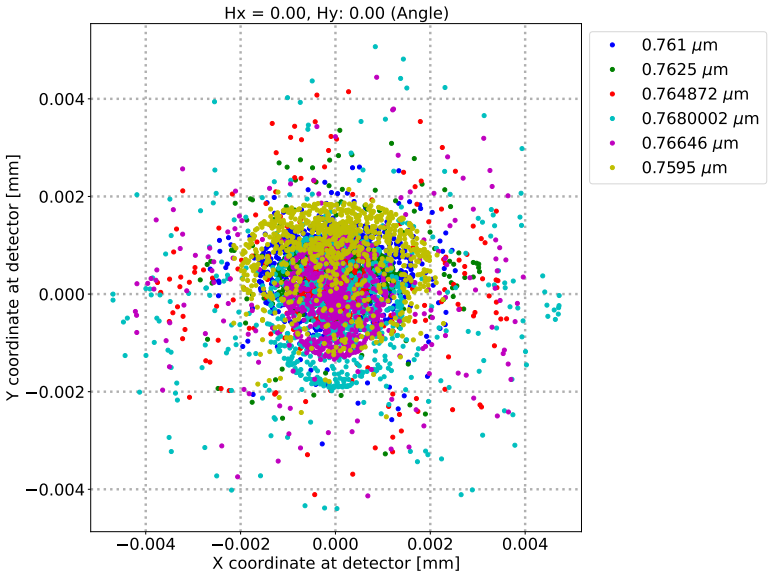

(a) Spot diagram of the FM at the on-axis field point. RMS radius: 2.225 μm, GEO radius: 5.297 μm

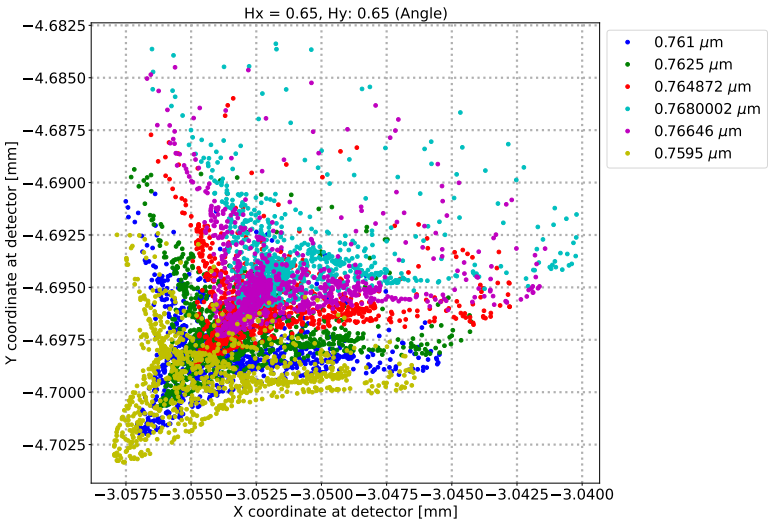

(b) Spot diagram of the FM at the off-axis field point. RMS radius: 6.062 μm, GEO radius: 18.685 μm

Figure 4.7: Simulated spot diagrams of the FM at different field points.

The spot diagram shows the ray distributions by tracing bundles of rays through the system to the image surface (*ZEMAX LLC.*, 2020). It provides the RMS spot radius which describes the distribution range of the most image points in the spot diagram, and the geometric (GEO) spot radius which describes the actual geometric radius of the dispersion image points. In Figure 4.7, the GEO radii are 5.297 μm at the on-axis field point of (0.00°, 0.00°) and 18.685 μm at the off-axis field point of (0.65°, 0.65°). As the detector GSENSE400BSI has a pixel size of 11 μm, thus the designed system is capable of imaging a perfect point source onto approximately 2 pixels. Since the pinhole setup is a non-ideal point source, an additional cone of divergence has to be considered.

For the pinhole setup, a pinhole with a diameter of 25 μm is collimated by an aspheric lens with a focal length of 200 mm. This corresponds to an additional half cone angle: $\tan^{-1}(\frac{0.0125}{200}) \approx 0.003581°$. Since the FOV of 1.3° corresponds to the illuminated detector area of 861*861 pixels, the image height of the pinhole setup is about $\frac{861\ pixels}{1.3°} * 0.003581° * 2 = 5$ pixels. Therefore, the overall expected spot size is about 7 illuminated pixels if the whole system is perfectly aligned. As the virtual distance of the pinhole setup is about 2.9 km for the worst case scenario, not at the infinity, this corresponds to a GEO radius of 24.177 μm at the off-axis field point of (0.65°, 0.65°) as simulated with optical raytracing software ZEMAX. Therefore, the expected size of the spot imaged by the pinhole setup is 8 pixels.

Compared with the measured spot size in Figure 4.6, the actual measured spot size of 10 pixels matches the above simulated result of 8 pixels with the alignment uncertainty about 2 pixels, which indicates that the alignment procedures for the front optics are correct and appropriate. Meanwhile, the instrument is designed with a full FOV of 1.3°, which is equally divided into 40 altitude layers with a vertical resolution of 1.5 km at the tangent point (*Wroblowski*, 2022). Thus one space altitude layer seen by the instrument corresponds to the illuminated area of $22 * 861$ pixels on the detector array. As the measured spot size of 10 pixels is smaller than 22 pixels, the instrument can achieve the designed vertical resolution of 1.5 km.

4.1.4 Alignment Results for the Camera Optics of the FM

As mentioned before, a visibility map in the spatial domain should be calculated to evaluate the alignment of the camera optics. The visibility of a monochromatic interferogram is defined by:

$$Visibility = \frac{I_{max} - I_{min}}{I_{max} + I_{min}}, \tag{4.6}$$

where I_{max} is the maximum value (or peak value) of the fringes and I_{min} is the minimum value (or valley value) of the fringes.

According to Equation 2.1, the monochromatic interferogram of an ideal SHS instrument can be modified as:

$$I(x,\sigma) = I_0(x,\sigma) + I_1(x,\sigma)\cos\left[2\pi f_x x + \varphi(x,\sigma)\right], \tag{4.7}$$

where $I_0(x,\sigma)$ is the direct current (DC) term or the baseline term as the unmodulated part, $I_1(x,\sigma)$ is the amplitude of the modulated part, and $\varphi(x,\sigma)$) is the additive phase distortion term associated with the emission wavenumber and the position at the detector array.

Combining Equation 4.6 with Equation 4.7, the visibility of a monochromatic interferogram can be calculated as:

$$\begin{aligned} Visibility &= \frac{I_{max} - I_{min}}{I_{max} + I_{min}} \\ &= \frac{I_0 + I_1 - (I_0 - I_1)}{I_0 + I_1 + I_0 - I_1} \\ &= \frac{2I_1}{2I_0} = \frac{I_1}{I_0}. \end{aligned} \tag{4.8}$$

Therefore, the interferogram visibility can be derived by taking the ratio of the amplitude to the baseline. The unmodulated frequency components and modulated frequency components can be separated with two different window functions in the spectral domain after applying fast Fourier transform (FFT) with the recorded interferogram. Then inverse fast Fourier transform (IFFT) can be implemented to obtain the separated unmodulated signal and modulated signal in the spatial domain. Then the signal amplitude and baseline can be estimated by taking the modulus of the modulated and unmodulated signal.

In addition, the visibility of a polychromatic interferogram can be calculated as:

$$Visibility = \frac{I_{max} - I_{avg}}{I_{avg}}, \tag{4.9}$$

where I_{avg} means the average value of the interferogram and $I_{max} - I_{avg}$ represents the signal amplitude of the modulated portion.

Once the optimum position of the camera optics is found, the interferogram and corresponding visibility, baseline and amplitude maps before fixing the position of the camera optics are calculated and shown in Figure 4.8. Note that there are three bad columns of the detector array as shown in Figure 4.8(a) at the column 268, column 523 and column 781. They arise from the detector itself with the non-ideal training parameters. After applying suitable training parameters for the further measurements,

these bad columns can be removed. The designed illuminated ROI is roughly $861 * 861$ pixels. The plotting is $1000 * 1000$ pixels. As an additional stop is inserted in the front of the detector array to suppress the straylight, the vignetting shadows can be observed in the edges of Figure 4.8(a).

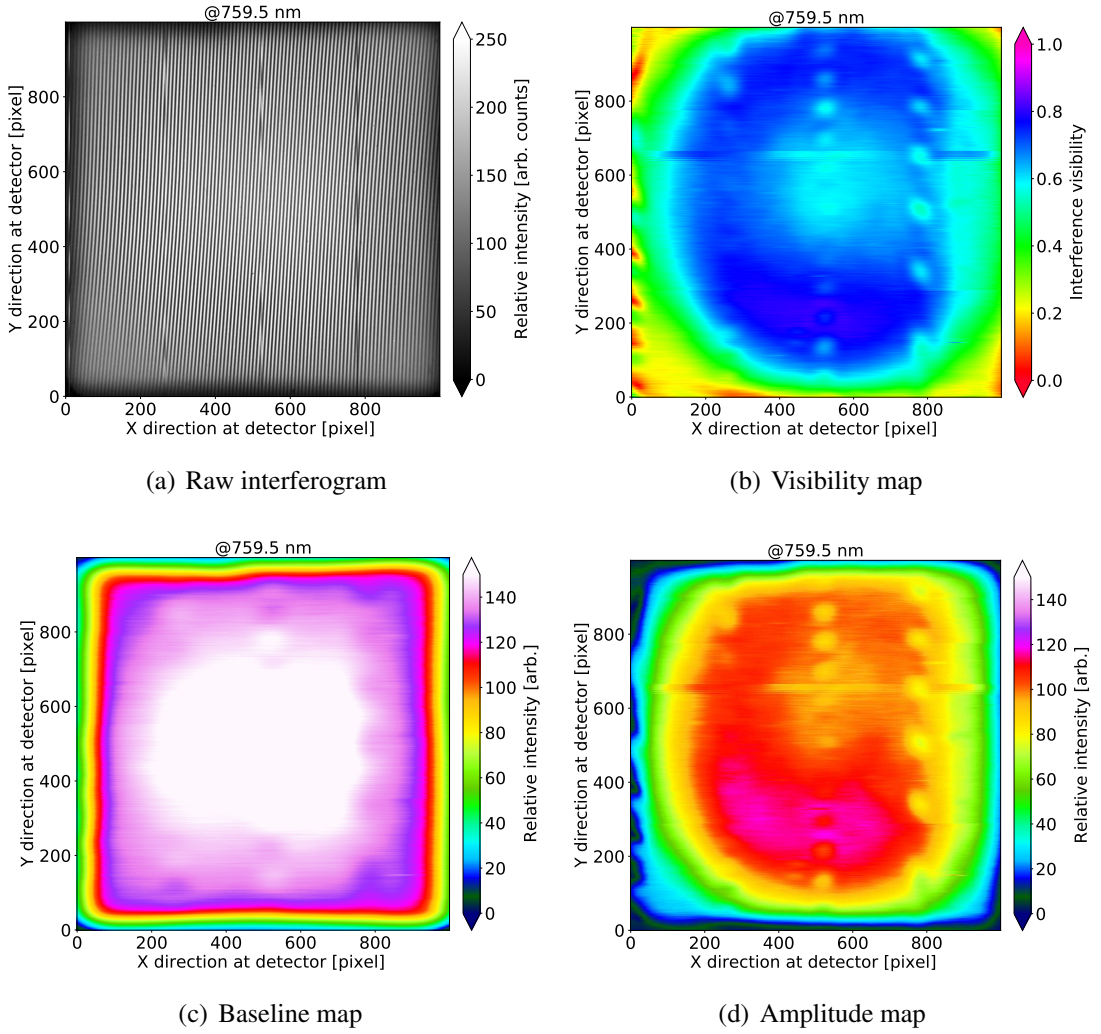

(a) Raw interferogram

(b) Visibility map

(c) Baseline map

(d) Amplitude map

Figure 4.8: The raw interferogram and corresponding calculated visibility, baseline and amplitude maps before fixing the position of the camera optics, where the operating wavelength is 759.5 nm.

Figure 4.8(b) shows the estimated visibility map. For the high spatial frequency operating at a wavelength of 759.5 nm, the visibility is about 60% in the middle and over 70% in the edges of the image. The trend in visibility is in line with the designed

expectations as mentioned in Section 4.1.2, which indicates that the alignment of the camera optics is correct.

After the optimum position of the camera optics is found, it must be secured into the barrel and fixture frame. During this fixing process, the slight displacements are inevitably induced. Thus it is necessary to compare the visibility performance before and after fixing the position of the camera optics. Figure 4.9 shows the visibility difference before and after fixing the position of the camera optics. The mean difference is 0.0026, the median difference is 0.0015 and the standard deviation is 0.033 in the ROI of the image. Ignoring the calculation error induced by the three bad columns, the actual standard deviation is below 0.008, which indicates that the camera optics is still well aligned after fixing.

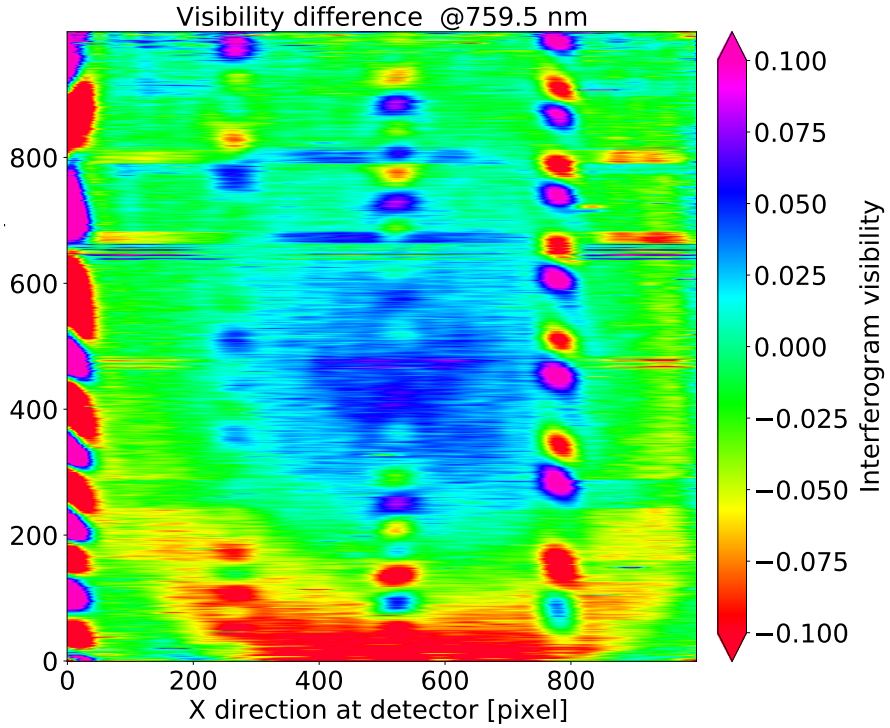

Figure 4.9: Visibility difference before and after fixing the position of the camera optics.

4.2 Imaging Performance Characterization of the SHS System

After the alignment of the front optics and camera optics has been completed, the imaging performances of the SHS system in the ambient and vacuum environments can be evaluated by using the pinhole setup. As the overall alignment of the instrument is carried out in the ambient environment and at room temperature of approximately 20°C, but the final in-orbit measurements will be carried out in a vacuum environment. Therefore a vacuum compensator is required to maintain good image performance when bringing the instrument from air into vacuum.

This vacuum compensator can be achieved by moving the last lens of the front optics away from the SHS by $\Delta = -0.1$ mm (*Wroblowski*, 2022) which is the expected compensation required to preserve good imaging qualities over the atmospheric scenery when bringing the instrument from air into vacuum. This section presents the imaging performance characterization of the instrument before and after moving the vacuum compensator.

4.2.1 Field Target Measurement of the FM Instrument before Moving the Vacuum Compensator

The distant buildings were imaged as the object of the instrument to evaluate the image quality of the instrument. Figure 4.10 shows the image of the telecommunication tower in Wuppertal measured by the FM of the AtmoLITE before moving the vacuum compensator. The distance between the telecommunication tower and instrument is about 4.2 km. The outline of the telecommunication tower can be clearly distinguished from the picture.

The further measurement was taken to look at different objects as shown in Figure 4.11, where Figure 4.11(a) shows the raw image including the forest, buildings, etc. Figure 4.11(b) shows the corresponding slice signal, which is represented by a vertical red line passing through five floors of a building in Figure 4.11(a).

There are five valleys in Figure 4.11(b), and one valley covers roughly 20 pixels which corresponds to one window in Figure 4.11(a). The window size of 20 pixels seen by the instrument corresponds to a cone angle $\frac{1.3^\circ}{861\ pixels} * 20\ pixels \approx 0.0302^\circ$. Thus the height of one window can be estimated as 2.1 m, which matches the actual window size within the estimated uncertainty.

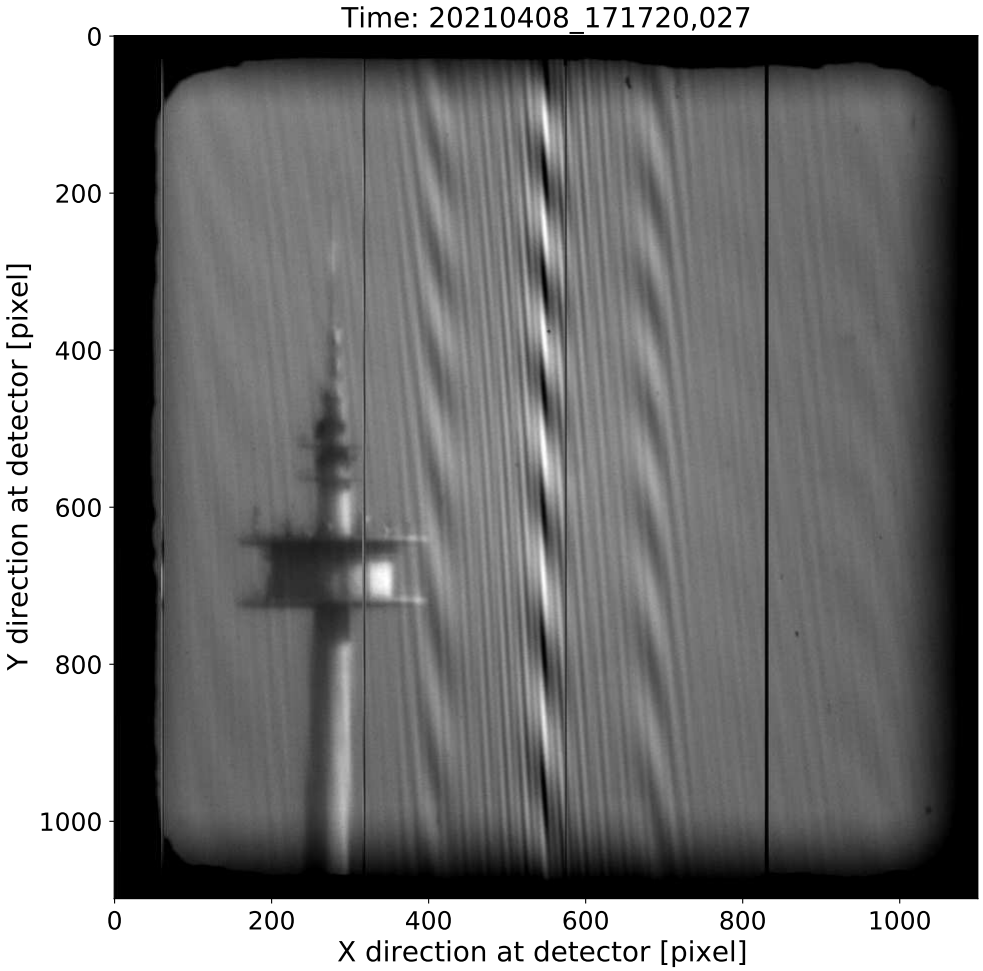

Figure 4.10: The telecommunication tower was imaged by the FM instrument before moving the vacuum compensator. Three bad columns are also shown in the plot and the center of the Barber pole is located roughly at the column 545 to 549. Note that as a plastic aperture is placed on the front of the instrument baffle to prevent contamination of the instrument, it might introduce multiple reflections, resulting in a slight decrease in contrast.

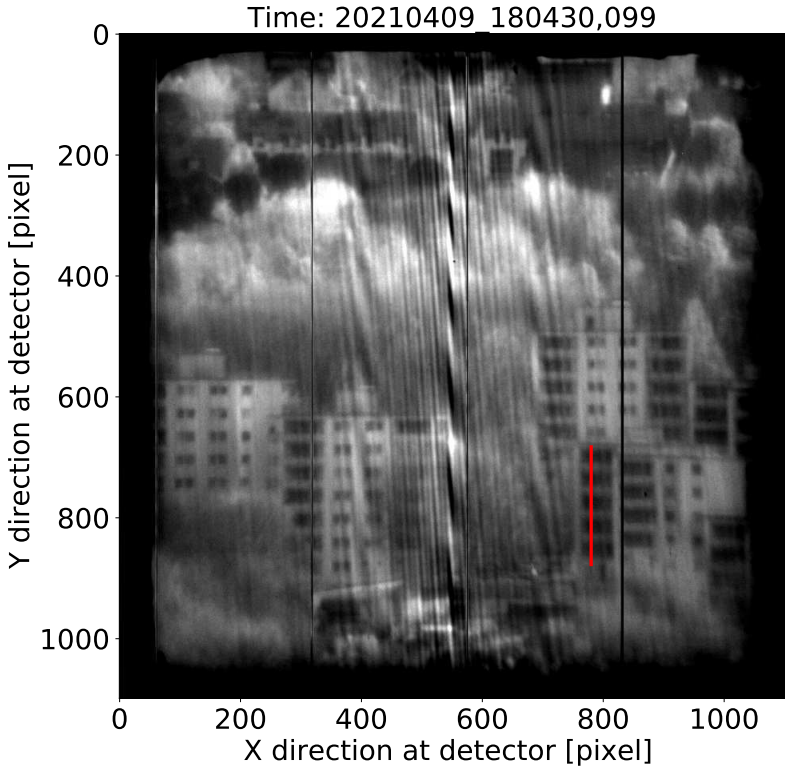

(a) Raw image

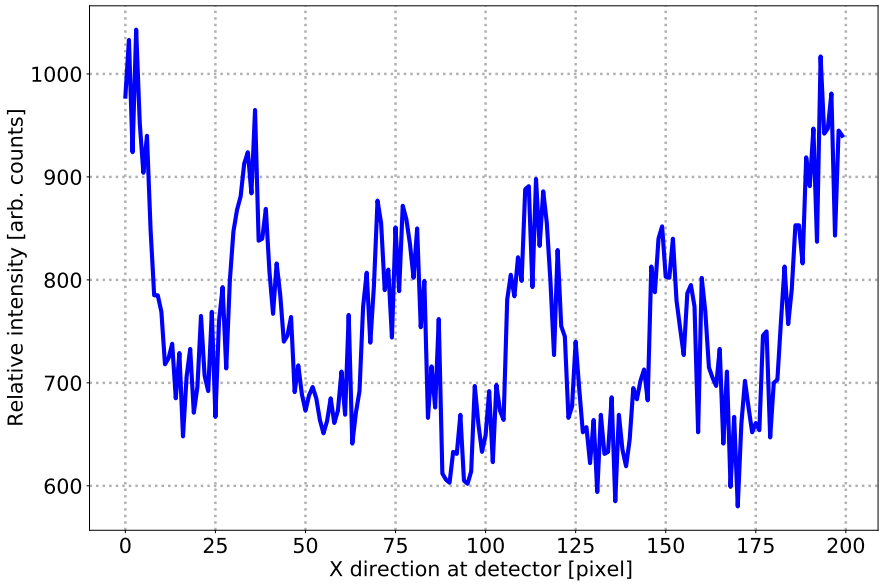

(b) Slice signal of the red line

Figure 4.11: Field imaging measurement of the instrument before moving the vacuum compensator.

4.2.2 Field Target Measurement of the FM Instrument after Moving the Vacuum Compensator

Figure 4.12 shows the field imaging measurement of the instrument after moving the vacuum compensator, where the image quality shows significant degradation. This is because the vacuum compensator is designed for the situation of bringing the instrument from air into vacuum. As the instrument was operating in the ambient environment for the field imaging measurement, the front optics of the instrument was out of focus after moving the vacuum compensator.

Figure 4.13 shows the simulated spot diagrams of the FM at the field points of (0.00°, 0.00°) and (0.65°, 0.65°) after moving the vacuum compensator in the ambient environment. The GEO radii are 149.431 μm at the on-axis field point of (0.00°, 0.00°), and 165.454 μm at the off-axis field point of (0.65°, 0.65°). Compared with the situation before the vacuum compensator is moved in Figure 4.7, the spot size increased by approximately 28 times for the on-axis field point and 9 times for the off-axis field point. This results in blurred images of the field imaging measurement after moving the vacuum compensator.

Table 4.1 summarizes the spot sizes at different field points simulated with the optical raytracing software ZEMAX for different application scenarios with and without moving the vacuum compensation in the ambient and vacuum environments, respectively. The corresponding spot diagrams are shown in Appendix A.4. It can be found that the spot size after moving the vacuum compensator of the front optics should be the smallest in the vacuum environment.

As the virtual distance of the pinhole setup is about 2.9 km for the worst case scenario, not at the infinity, Table 4.1 also includes the simulation results for a light source distance of 2.9 km. It can be clearly seen that the non-infinite virtual distance of the pinhole setting has a negligible effect on the spot size imaged on the detector if the virtual distance of the pinhole setting exceeds 2.9 km.

Note that the correct movement direction of the last lens of the front optics should be away from the SHS by $\Delta = -0.1$ mm when bringing the instrument from air into vacuum. If moving in the opposite direction by $\Delta = +0.1$ mm, the spot size will be worse. The GEO radii are 141.448 μm at the on-axis field point of (0.00°, 0.00°), and 163.613 μm at the off-axis field point of (0.65°, 0.65°) in the ambient environment. In the vacuum environment, the GEO radii are 289.316 μm at the on-axis field point of (0.00°, 0.00°), and 323.701 μm at the off-axis field point of (0.65°, 0.65°). The corresponding spot diagrams are shown in Appendix A.4. Thus, the spot size is biggest in the vacuum environment if the last lens of the front optics is moved in the opposite direction.

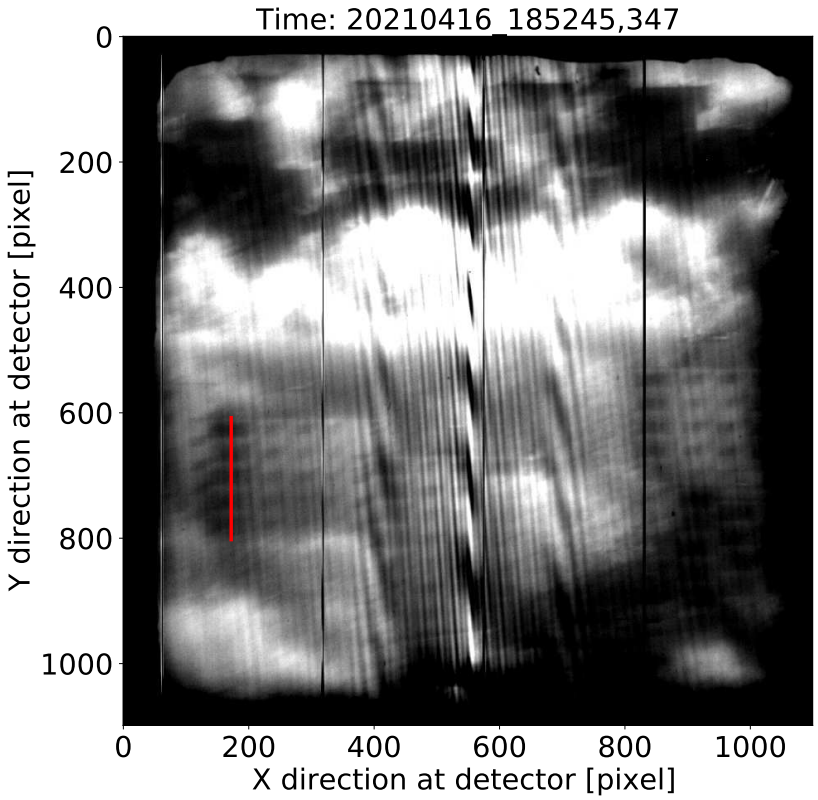

(a) Raw image

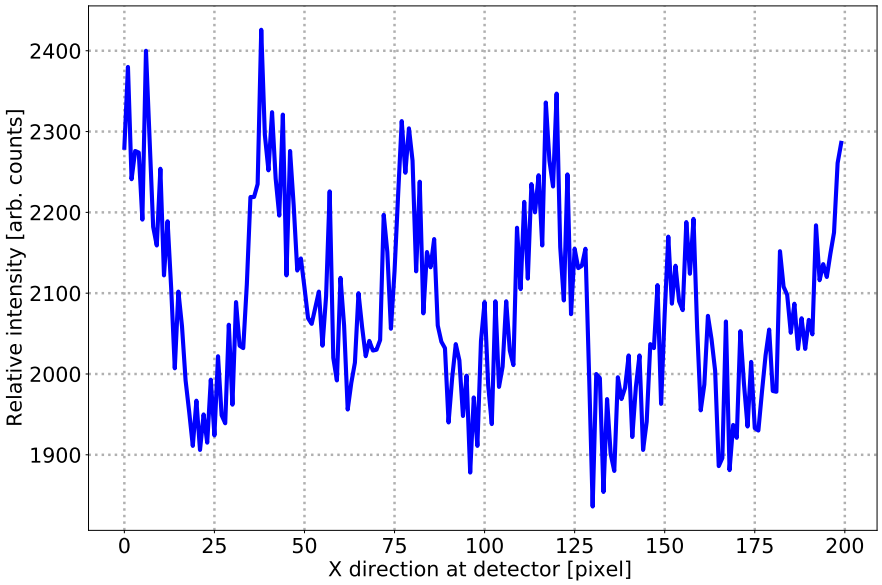

(b) Slice signal of the red line

Figure 4.12: Field imaging measurement of the instrument after moving the vacuum compensator.

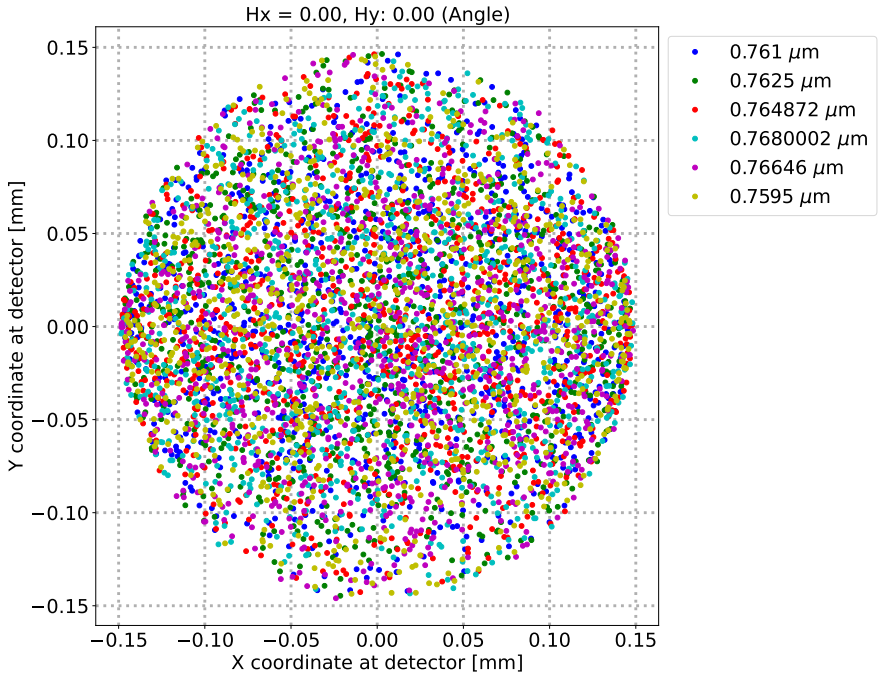

(a) RMS radius: 103.831 μm, GEO radius: 149.431 μm

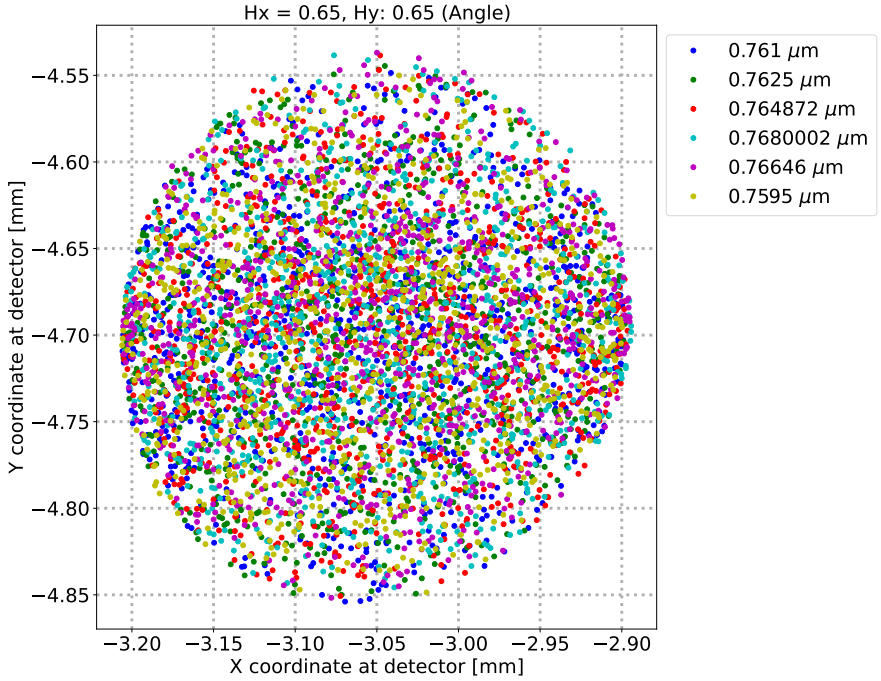

(b) RMS radius: 110.250 μm, GEO radius: 165.454 μm

Figure 4.13: Simulated spot diagrams at different field points for the FM with the vacuum compensation in the ambient environment.

Table 4.1: Spot sizes at different field points at room temperature of 20°C for different application scenarios simulated with the optical raytracing software ZEMAX

Environment	Ambient				Vacuum			
Compensation	Without		With		Without		With	
Field Point	0°	0.65°	0°	0.65°	0°	0.65°	0°	0.65°
GEO radius [μm]	5.297	18.685	149.431	165.454	145.518	162.511	2.551	11.649
Pixel [-]	1	2	14	16	14	15	1	2
GEO radius for the Pinhole [μm]	10.485	24.177	154.627	170.966	140.316	156.990	7.231	16.644
Pixel for the Pinhole [-]	1	3	15	16	13	15	1	2

Therefore, it is necessary to pay enough attention to the direction of movement of the last lens of the front optics when bringing the instrument from air into vacuum. Further measurements are carried out with the pinhole setup to investigate the change in spot size after moving the vacuum compensator.

4.2.3 Pinhole Setup Measurement of the FM Instrument after Moving the Vacuum Compensator

Figure 4.14 shows the spot imaged by the pinhole setup and the corresponding two cross slices at the brightest point of the spot image, where the instrument is operated in the ambient environment with moving the vacuum compensator. The FWHM of the spot size is about 25 to 30 pixels.

Figure 4.15 shows the corresponding vacuum measurement results after pumping the vacuum chamber. The FWHM of the spot size reduced to 10 to 20 pixels. For the off-axis field, the measurement results are shown in Appendix A.5.

The measured spot sizes and the simulated spot sizes of the pinhole setup are summarised in Table 4.2. The simulated spot size in Table 4.2 is the sum of the simulated spot size for the pinhole setup in Table 4.1 plus the 5 pixels corresponding to the cone angle of the pinhole, as mentioned in Section 4.1.3.

Table 4.2: Comparison of the measured spot size and simulated spot size at room temperature of 20°C for the pinhole setup

Environment	Ambient		Vacuum
Compensation	Without	With	With
Simulated spot size [pixel]	8	21	7
Measured spot size [pixel]	10	30	20

Obviously, the measured spot size is two to three times larger than the simulated spot size after moving the vacuum compensator. This will reduce our spatial resolution by a factor of about 2 or 3.

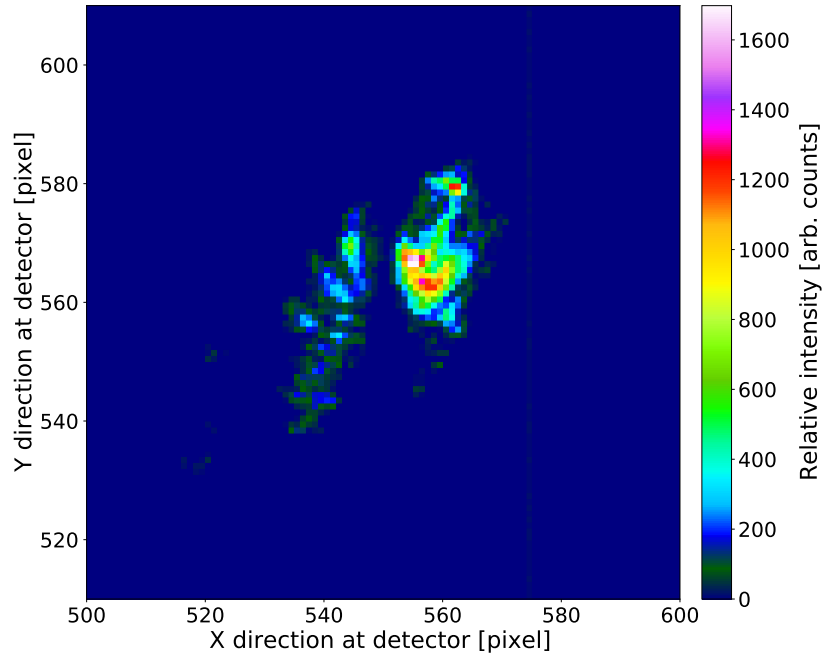

(a) The output image on the detector array.

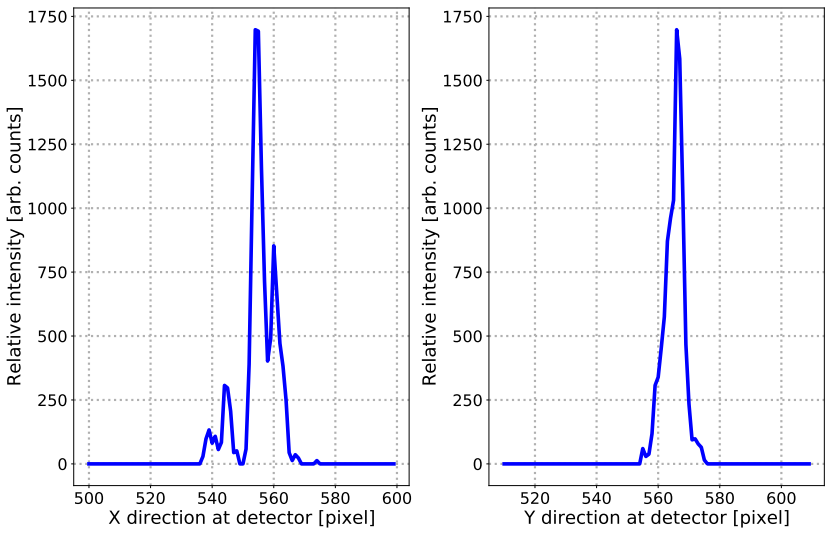

(b) The two cross slices at the brightest point of the image points.

Figure 4.14: The spot imaged by the pinhole setup in the ambient environment with moving the vacuum compensator, where the mode of the detector is HDR_LowGain and the instrument is oriented to the on-axis field point. Note that this measurement was done before the vibration test for the FM of the AtmoLITE.

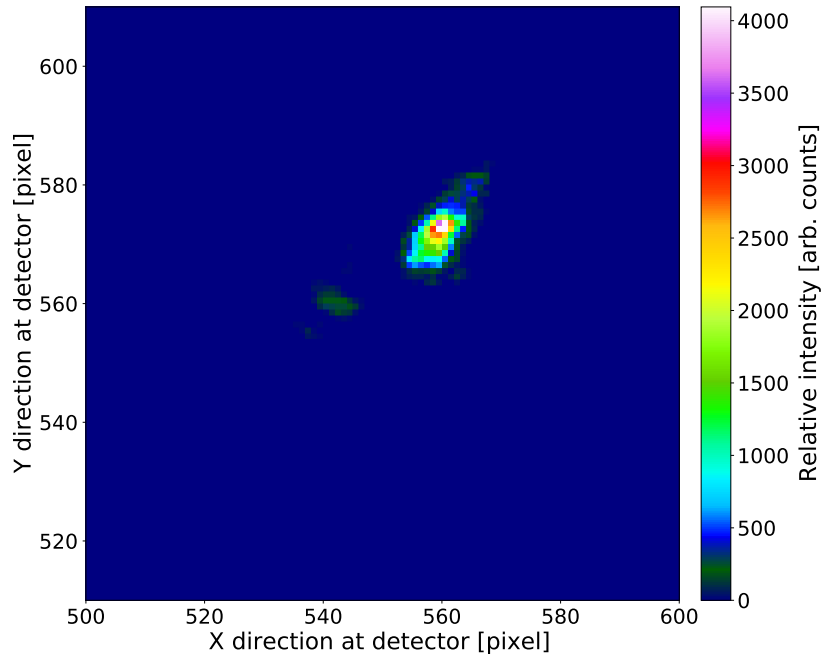

(a) The output image on the detector array.

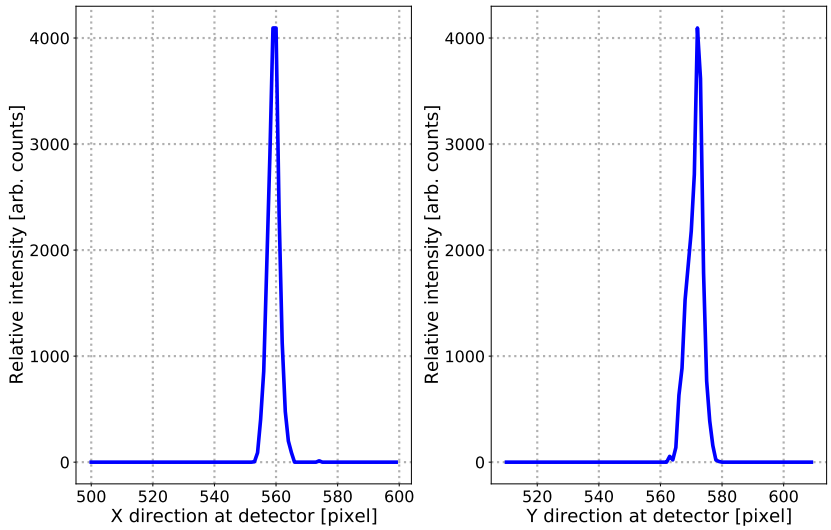

(b) The two cross slices at the brightest point of the image points.

Figure 4.15: The spot imaged by the pinhole setup in the vacuum environment with moving the vacuum compensator, where the mode of the detector is HDR_LowGain and the instrument is oriented to the on-axis field point.

4.2.4 Pinhole Setup Measurement of the FM at Different Temperatures in the Vacuum Environment.

The designed optomechanical material of the FM of the AtmoLITE instrument is Invar, but the actual material used is aluminium. It is therefore necessary to investigate the variation in spot size at different temperatures.

Figure 4.16 shows the simulated spot diagrams of the FM at 25.0°C and -35.0°C after moving the vacuum compensator in the vacuum environment, where the distance of the light source in the simulation is set to 2.9 km, taking into account the non-infinite virtual distance of the pinhole setup. The GEO radii are 15.227 μm at 25.0°C, and 24.561 μm at -35.0°C respectively. The change in spot size at these two temperatures is 9.334 μm, which is less than a pixel width of 11 μm. This means that the spot size should remain almost constant if the thermal expansion effect of the optomechanical material is not taken into account.

Figure 4.17 shows the measured points imaged by the pinhole setup at 29.0°C and -34.3°C. Figure 4.18 shows the corresponding two cross slices at the brightest point in Figure 4.17. It can be clearly seen that the size of the spots increases as the temperature decreases. The measured spot sizes are about 20 pixels at 29.0°C, and about 45 pixels at -34.3°C, which indicates that due to the use of aluminium as an optomechanical material, the effect of its thermal expansion on the optical performance of the instrument should be further investigated for further missions.

As mentioned in Section 4.1.3, a vertical resolution of 1.5 km at the tangent point seen by the instrument corresponds to an illuminated area of 22 pixels on the detector array. One altitude layer corresponds to a cone angle of 0.0325° as seen by the instrument and the pinhole setup provides a cone angle of 0.007°. Depending on the measured spot sizes imaged by the pinhole setup, the actual spatial resolution of the instrument may be at least three times worse than expected. This requires that the imaging characteristics of the instrument should be re-evaluated with the moon as the imaging target during the in-orbit measurements.

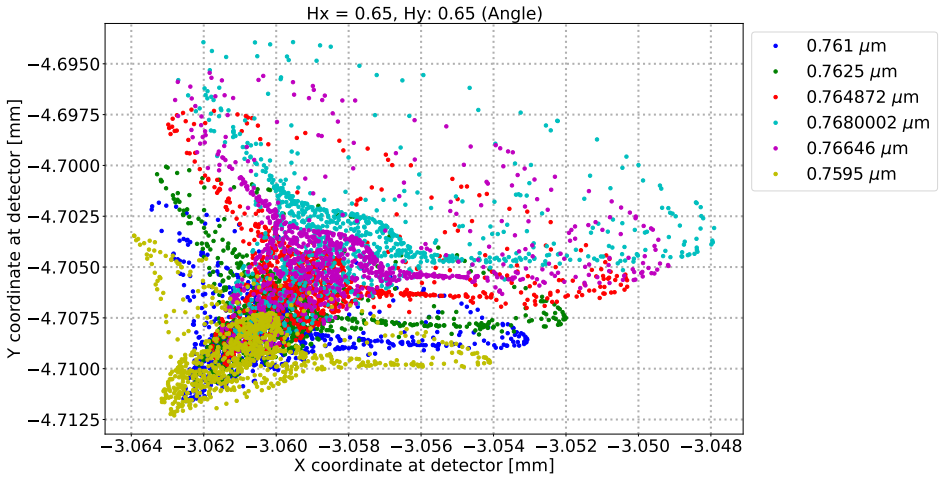

(a) Instrument temperature: 25.0°C, GEO radius: 15.227 μm

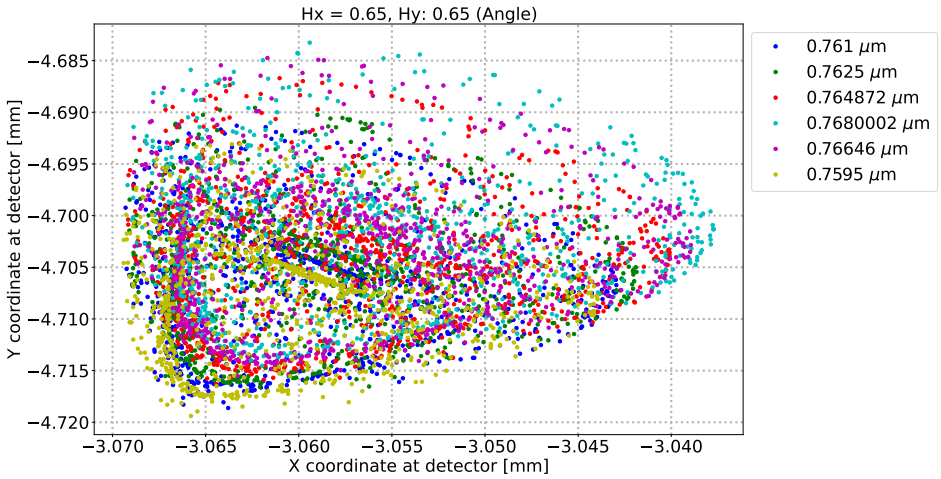

(b) Instrument temperature: -35.0°C, GEO radius: 24.561 μm

Figure 4.16: Simulated spot diagrams of the FM at 25.0°C and -35.0°C after moving the vacuum compensator in the vacuum environment. Note that the distance of the light source in the simulation is set to 2.9 km, taking into account the non-infinite virtual distance of the pinhole setup.

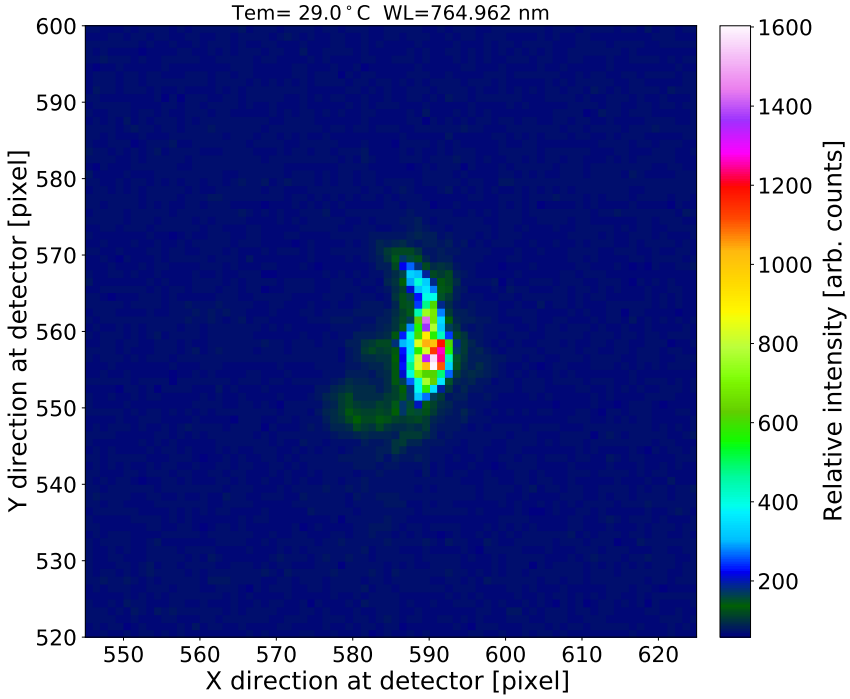

(a) Spot imaged by the pinhole setup at 29.0°C

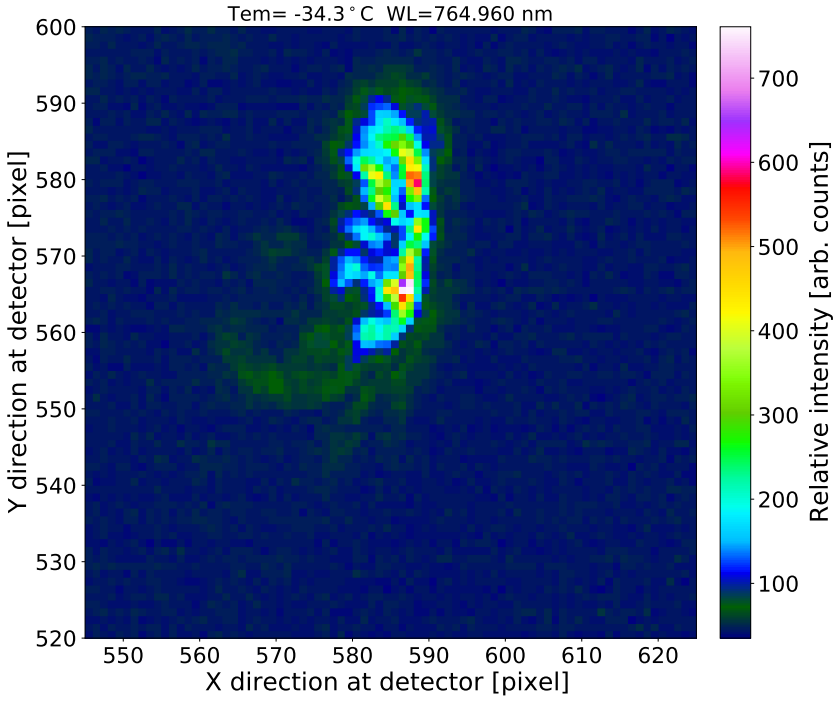

(b) Spot imaged by the pinhole setup at -34.3°C

Figure 4.17: Measured points imaged by the pinhole setup at 25.0°C and -35.0°C after moving the vacuum compensator in the vacuum environment.

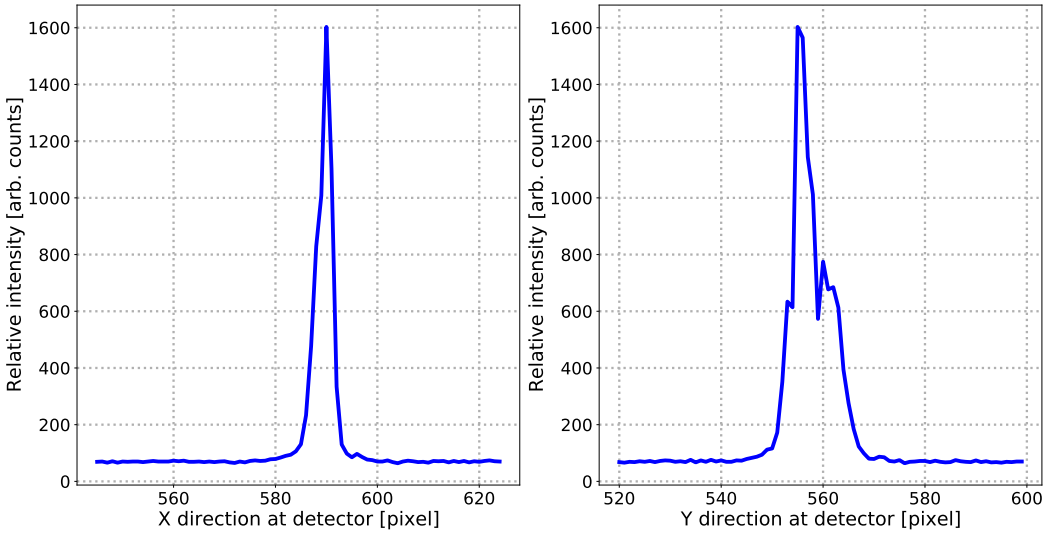

(a) The two cross slices at the brightest point in Figure 4.17(a)

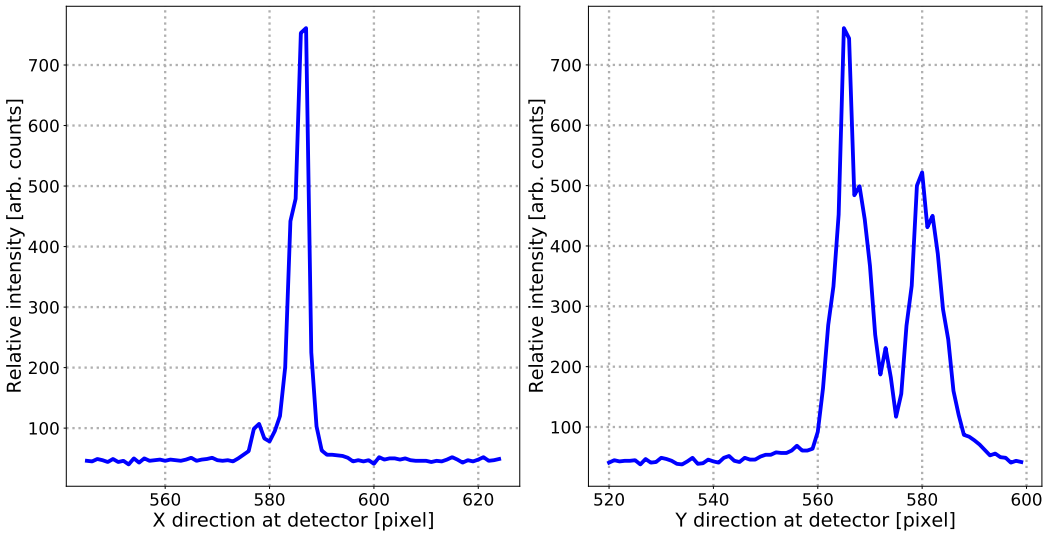

(b) The two cross slices at the brightest point in Figure 4.17(b)

Figure 4.18: The corresponding two cross slices at the brightest point in Figure 4.17.

4.3 Optical Filter Characterization

An optical bandpass filter is required for the AtmoLITE instrument to suppress spectral ghost line leakage and limit the observed wavelength range to between 758.5 nm and 766.0 nm. The transmission curve of the optical bandpass filter was measured using the instrument as shown in Figure 4.19, where the ACU was utilised as the light source.

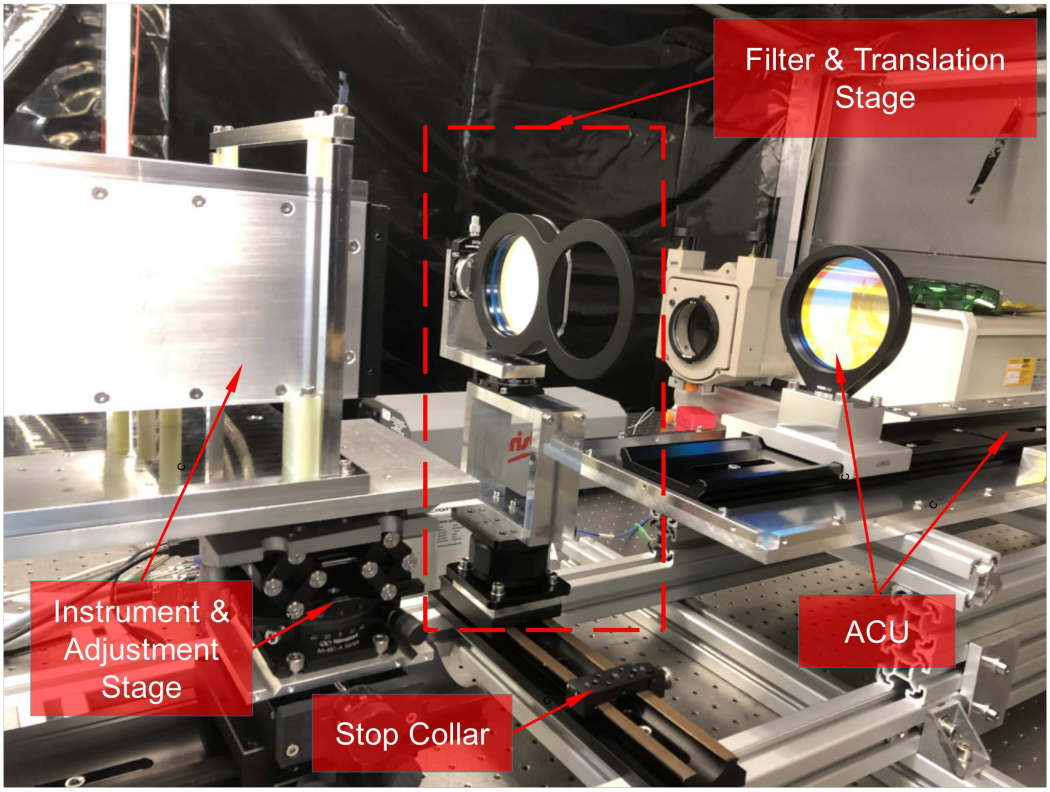

Figure 4.19: Measurement setup for obtaining the optical filter transmission curve.

The alignment procedures of the whole setup are as follows:

1) The instrument is placed in front of the ACU. Move the instrument vertically and horizontally to find the centre of the top flat area. The instrument is then tilted and inclined to complete the angular scan vertically and horizontally. This step aligns the instrument and the ACU so that they are equal in height and coaxial.

2) Insert a bandpass filter between the instrument and the ACU. Repeat the vertical and horizontal translation and angular sweeps for the filter so that it is coaxial and equal in height to the instrument and the ACU.

3) Scan the entire spectral range in steps of 0.1 nm from 758.4 nm to 767.4 nm. Two measurements were taken at each wavelength, one transmission measurement without the filter and one obstructed measurement with the filter. The transmission coefficient of the filter is calculated by the ratio between the obstructed intensity to the transmitted intensity. This step gives the transmission coefficient of the filter at the current tilt angle of the filter.

4) Tip and tilt the filter to the other tilt angles and repeat step 3. This step gives the transmission coefficient of the filter at the different tilt angles of the filter.

5) Due to the blue shift of the bandpass filter, the entire transmission curve of the filter will shift towards shorter wavelengths when light is incident on the filter at a non-zero angle of incidence (AOI). Compare the measurement results of the steps 3 and 4 to find the nominal position of the filter where the light exiting the ACU is incident perpendicular to the filter.

6) After finding the nominal position of the filter, repeat the measurement in step 3 to obtain the actual transmittance curve of the filter.

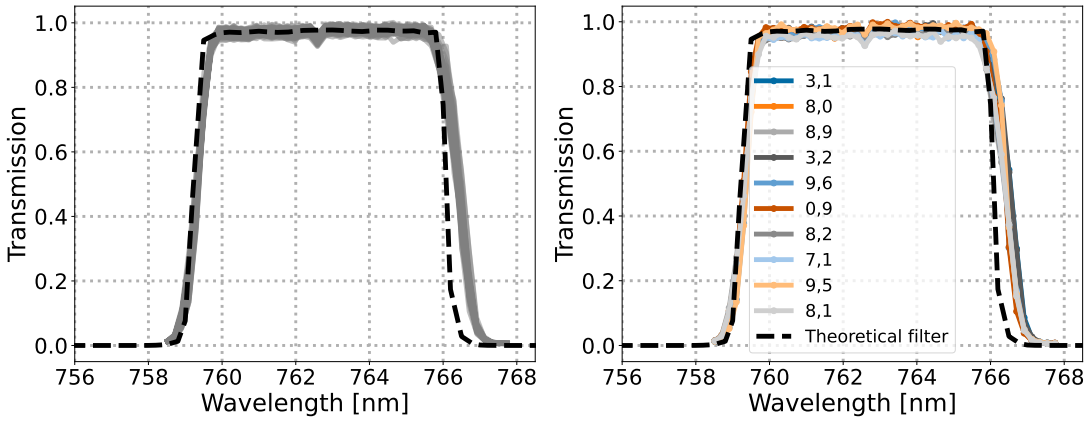

Figure 4.20: The transmission curve of the filter measured at the nominal position of the filter where the light exiting the ACU is incident perpendicular to the filter. The ROI of the detector is divided into 100 sub-regions by a grid of 10*10 superpixels. The spaghetti plot for all 100 regions is shown on the left subplot. The right subplot shows the 10 regions that deviate the most from the median of all 100 sub-regions.

Figure 4.20 shows the measured transmission curve of the filter at the nominal position of the filter where the light exiting the ACU is incident perpendicular to the filter. The ROI of the detector is divided into 100 sub-regions by a grid of 10*10 superpixels.

The spaghetti plot for all 100 regions is shown on the left subplot. The right subplot shows the 10 regions that deviate the most from the median of all 100 sub-regions.

It can be clearly seen that the measured transmission curve in the top flat region agrees with the theoretical filter curve. The mean and standard deviation of the differences between the measured transmission curve and the theoretical filter curve between 760.0 nm and 765.0 nm are -0.00024 and 0.01054 respectively.

In addition, the transmittance curves of the filter are also measured with different aperture stops. The corresponding results will be presented in *Ntokas* (2022).

4.4 Chapter Summary

This chapter presented the optical performance characterization during and after the SHS glueing for the AtmoLITE instrument. The detailed alignment procedures for the front optics and camera optics were introduced. The goal of aligning the front optics was to minimize the spot size imaged by a pinhole setup on the detector array by adjusting the distance between the last lens of the front optics and the SHI. And the purpose of aligning the camera optics was to achieve the desired contrast or visibility of the entire SHS system by adjusting the distance between the SHI and the camera optics and the distance between the camera optics and the detector.

As the overall alignments of the instrument were carried out in the ambient environment and at room temperature of approximately 20°C, but the final in-orbit measurements will be carried out in a vacuum environment. Therefore a vacuum compensator is required to maintain good image performance when bringing the instrument from air into vacuum. In order to verify the effectiveness of the designed vacuum compensator, the pinhole setup and field target measurements were performed. Before moving the vacuum compensator in the ambient environment, the measured spot size of 10 pixels matches the simulated result of 8 pixels with the alignment uncertainty about 2 pixels, which indicates that the alignment procedures for the front optics were correct and appropriate. However, after moving the vacuum compensator, the measured spot size is two to three times larger than the simulated spot size. This will reduce our spatial resolution by a factor of about two or three. Meanwhile, the variation of the spot size at different temperatures was investigated. The results show that the spot size imaged by the pinhole setup increases as the temperature decreases, which indicates that due to the use of aluminium as an optomechanical material, the effect of its thermal expansion on the optical performance of the instrument should be further investigated for further missions. The imaging characteristics of the instrument should be re-evaluated using the moon as the imaging target during the in-orbit measurements.

In addition, the transmission curve of the optical bandpass filter was measured and the results showed that the measured transmission curve in the top flat region agrees with the theoretical filter curve.

Chapter 5

Characterization and Calibration of the FM for the AtmoLITE Instrument

The previous chapters described the instrument alignment procedures and optical performance characterization during and after the SHS glueing. Once the final SHS system was completely assembled and aligned, a series of interferogram measurements were performed to characterize and calibrate instrument performance for further analysis. This chapter mainly presents property characterization and calibration results of the FM, including the dark and bias current subtraction, spike correction, removal of the DC and low frequency components, Littrow wavelength calibration, phase distortion correction and amplitude variation estimation.

5.1 Measurement Strategy

For a monochromatic spectral radiation of $B(\sigma)$, the recorded intensity distribution as a function of position x on the detector array is given by:

$$I_\sigma(x) = B(\sigma) + B(\sigma)A(x,\sigma)\varepsilon(x,\sigma)cos(2\pi f_x x + \varphi(x,\sigma)), \tag{5.1}$$

where σ is the wavenumber of the incoming emission line, f_x is the spatial frequency of the recorded interferogram, A(x,σ) represents the amplitude variation induced by the ACU and instrument itself, $\varepsilon(x,\sigma)$ is the modulation efficiency and $\varphi(x,\sigma)$ is the phase distortion term.

According to the definition of visibility in Equation 4.6, the visibility of a mono-

chromatic interferogram is given by:

$$\begin{aligned} Visibility &= \frac{I_{max} - I_{min}}{I_{max} + I_{min}} \\ &= \frac{B(\sigma)A(x,\sigma)\varepsilon(x,\sigma)}{B(\sigma)} \\ &= A(x,\sigma)\varepsilon(x,\sigma). \end{aligned} \tag{5.2}$$

The goal of the calibration of the instrument is to obtain the visibility of $A(x,\sigma)\varepsilon(x,\sigma)$ at different temperatures and wavelengths. The laser observations were obtained at different wavelengths, temperatures and aperture stops. The corresponding dataset parameters are as follows:

- ★ Light source: the turnable laser and ACU.
- ★ Environment: thermal vacuum chamber.
- ★ Instrument temperature: the instrument temperature range was set at -40°C to 30°C. The actual temperature value of the instrument was obtained from the thermistor.
- ★ Detector temperature: the detector temperature was set to -25°C. The actual temperature value of the detector was obtained from the thermistor.
- ★ Wavelength range: 758.4 nm to 767.6 nm in 0.2 nm steps.
- ★ Monitors: the actual wavelength and intensity of the laser source were monitored by the wavemeter and picolog.

For measurements at each wavelength and temperature, multiple consecutive frames with the same integration time should be recorded and averaged to reduce statistical error and improve SNR. Figure 5.1 shows the standard deviation maps of the output dark current images for different average frame numbers. The detector output is in digital numbers (DN) or counts.

Figure 5.1(a) shows the standard deviation map of the raw recorded frame without any correction, and Figure 5.1(b) shows the corresponding map with the spike correction and removal of the dark and bright pixels, in which a threshold filter with a window size of 3*3 pixels was applied for the spike correction. Obviously, the standard deviation curve tends to be smooth and stable after averaging 10 frames. Finally, 4 frames were recorded at each wavelength and temperature for the instrument FM as a result of a negotiation between limited measurement time and accuracy.

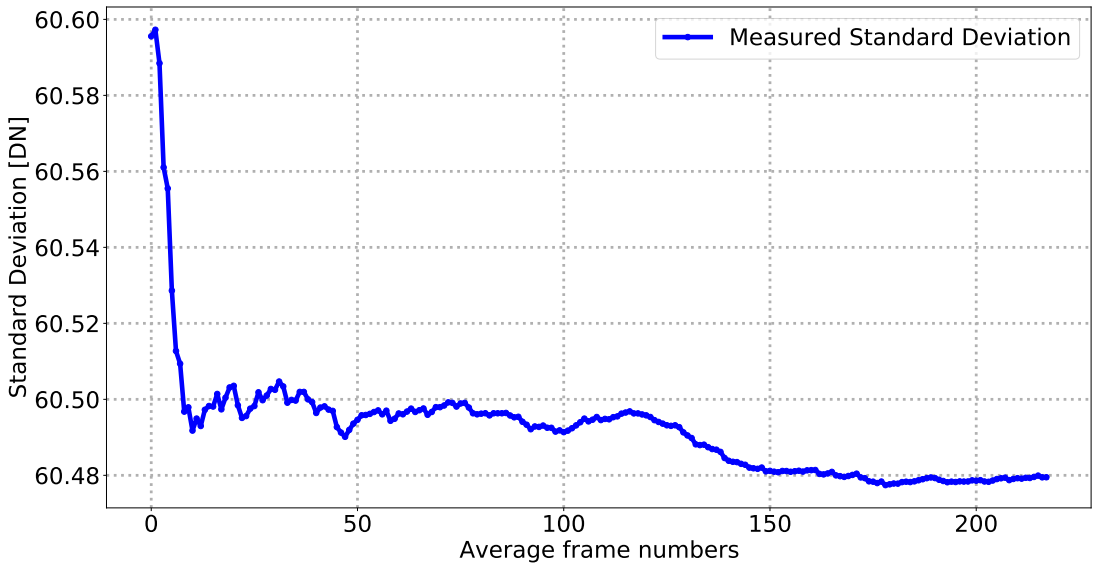

(a) Without any correction

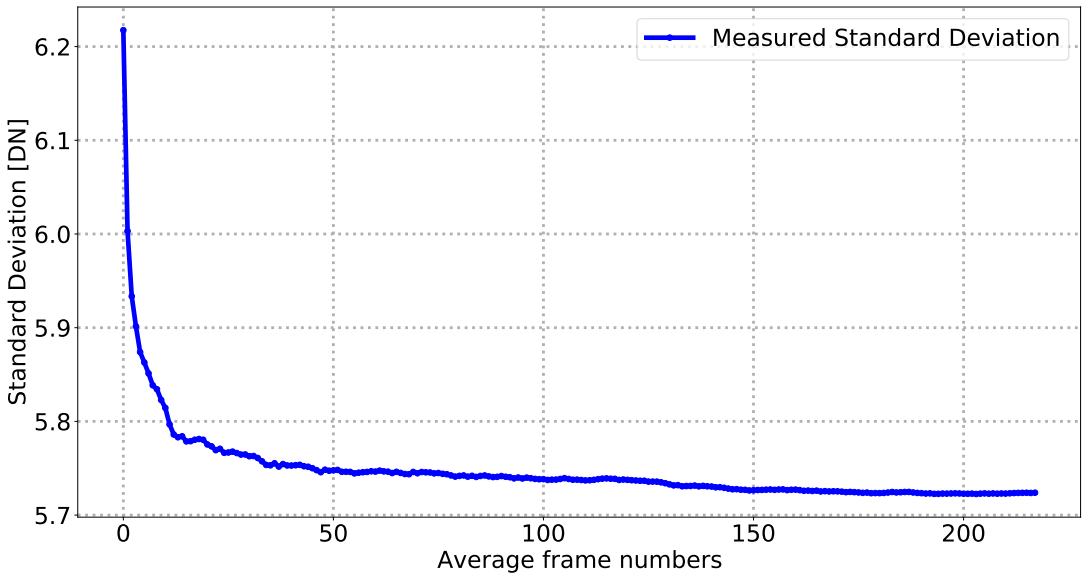

(b) With the spike correction and removal of the dark and bright pixels

Figure 5.1: Standard deviation maps of the dark current at different average frame numbers. Note that the integration time was set to 120 ms and the detector temperature was set to -11.1°C.

Figure 5.2 shows the standard deviation map and corresponding histogram of the dark current frame after averaging 4 frames for the instrument FM at the detector temperature of -25°C. The mean and median of the standard deviation map are 2.78 DN and 2.55 DN respectively. The output variation in most of detector array regions is less than 4 DN, which indicates that the GSENSE detector can provide a relatively constant output response.

It is worth noting that during the process of averaging the frames, some frames were found to have output counts exceeding 4095, which is the upper limit of the 12-bit output value. These frames were considered to be anomalous and they were discarded without participating in the averaging process.

5.2 Dark and Bias Current Subtraction

The image recorded by the instrument detector contains the light intensity from the laser source as well as the DC dark and bias current from the randomly generated electrons and holes in the detector. Therefore, the 'background frames' were taken at the same integration time and temperature. It was then averaged and subtracted to reduce the noise contribution and to remove the average of the bias and dark current. In this process, a threshold filter with an appropriate window size was applied for the spike correction before subtraction.

After subtracting the DC dark and bias current, the image was normalised row by row by dividing the mean intensity of each row to remove the laser source brightness profile. The normalized monochromatic interferogram can be expressed as:

$$I_\sigma(x) = 1 + A(x,\sigma)\varepsilon(x,\sigma)cos(2\pi f_x x + \varphi(x,\sigma)), \tag{5.3}$$

5.3 Define Region of Interest

Before processing the normalized interferogram, the size of the ROI needs to be decided. The recorded image size is 1100*1100 pixels, but the effective illuminated ROI is about 860*860 pixels. The actual trimmed ROI should be large than the effective ROI in order to avoid non-periodic edge effects produced by FFT (*Harlander et al.*, 2019b). Thus the ROI of 880*880 pixels around the zero OPD position was trimmed from the dark current corrected and normalized images for the further Littrow calibration and phase distortion correction.

The zero OPD position was obtained with constructed polychromatic interferogram by superimposing multiple monochromatic interferograms, as shown in Figure 5.3. The

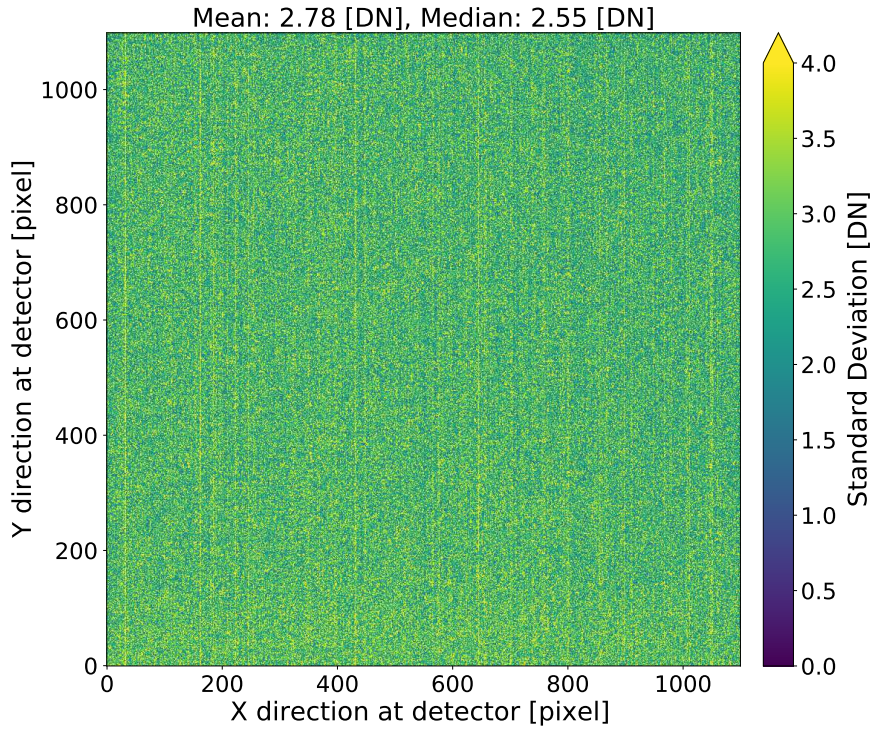

(a) Standard deviation map

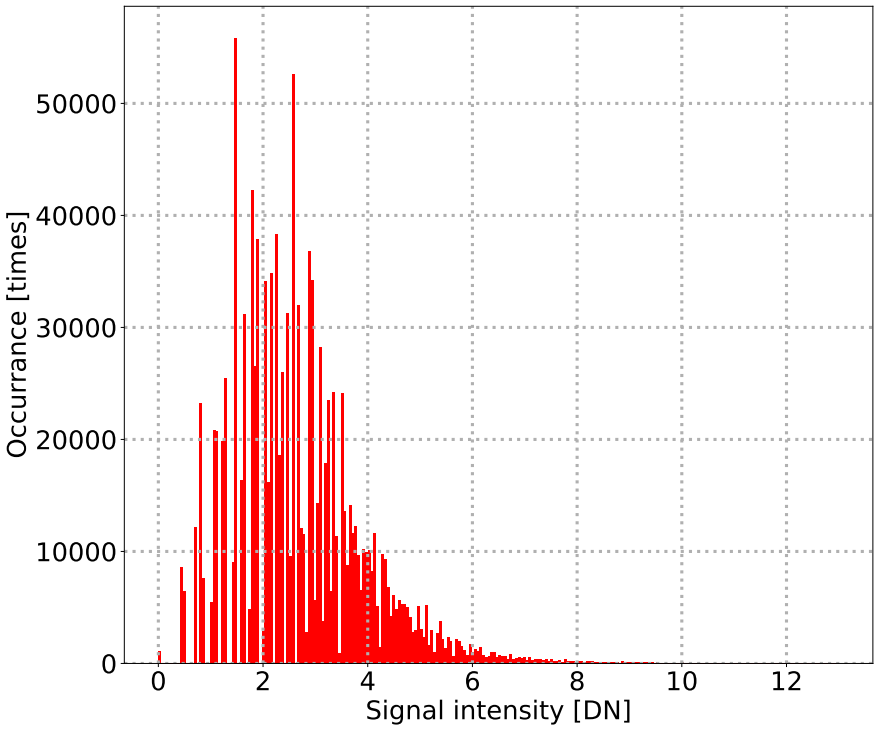

(b) Standard deviation histogram

Figure 5.2: Standard deviation map and histogram of the dark current frame after averaging 4 frames at the detector temperature of -25°C.

coordinate of the center pixel of the middle barber-pole gives the zero OPD position. The modulation along the y-axis within the barber-pole was caused by the tilted fringes due to the phase distortion, which can be removed after the phase correction.

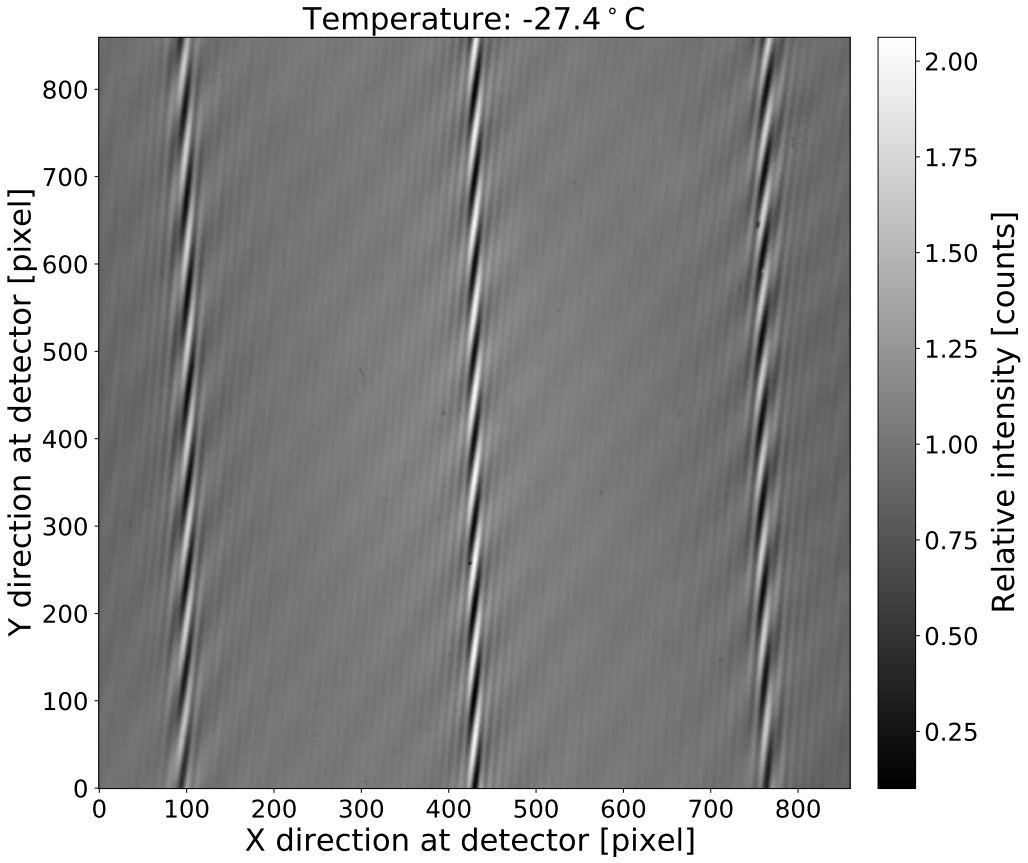

Figure 5.3: Constructed polychromatic interferogram by superimposing the multiple monochromatic interferograms.

5.4 Littrow Condition Calibration

As discussed in Chapter 2, the fringe frequency recorded on the detector array plane can be expressed as:

$$f_x = 4 \tan \theta_L \, (\sigma - \sigma_0) \, M, \tag{5.4}$$

where θ_L is the Littrow angle and σ_0 is the Littrow wavenumber of the SHS system. M is the magnification factor of the camera optics. The designed value of the magnification

factor M is 0.617 in the vacuum environment. The designed Littrow wavenumber is 13047 cm^{-1} and the corresponding Littrow angle is 6.602° (*Wroblowski*, 2022). Before further phase distortion correction, the actual Littrow wavenumber of the instrument has to be calibrated.

For a given temperature, the FM of the AtmoLITE instrument was illuminated by a homogeneous diffuse emission line source (namely the ACU) at different wavelengths as mentioned in Section 5.1. The spectra of the measured interferograms were obtained by the Fourier transformation with the apodization function and zero-padding. After peek searching, a series of σ_i and f_{xi} can be obtained for further linear regression to estimate the actual Littrow condition.

Due to variations in the optical path or the optical distortion of the instrument, the fringe frequency at each row was slightly variated. The average value across all rows at each wavelength is calculated and plotted as a function of wavenumber, as shown in Figure 5.4. According to the linear fitting results, the estimated Littrow wavenumber is 13050.687 cm^{-1}, the corresponding Littrow angle is 6.600° and the magnification factor of the camera optics is 0.590 in the vacuum environment. These derived values provide the as built Littrow condition at the temperature of the FM of the AtmoLITE instrument during the calibration measurement.

Furthermore, the linear regression was analysed for the estimated Littrow wavenumbers at different temperatures. Figure 5.5(a) shows the estimated Littrow wavenumbers at different temperatures, which is found that there is a linear trend of temperature dependence:

$$\sigma_0 = (-0.107 \pm 0.006)\frac{cm^{-1}}{^\circ C} * T + (13047.889 \pm 0.108)cm^{-1},$$

where T is the instrument temperature. The expected thermal drift value for the Littrow wavenumber should be less than 1 cm^{-1} over the nominal operating temperature range (*Wroblowski*, 2022), but the measured thermal drift of the Littrow wavenumber is up to 6 cm^{-1}. This means that the actual Littrow wavelength in the in-orbit measurements will shift towards the shorter wavelengths, resulting in the spectral overlap. Therefore, the ghost line removal needs to be considered for the in-orbit measurements.

Figure 5.5(b) shows the estimated magnification factors of the camera optics at different temperatures. From -27.4°C to 29°C, the mean of the magnification factors is 0.592 and the corresponding standard deviation is 0.00076, which indicates that the magnification factor of the camera optics remains nearly stable over the nominal operating temperature range.

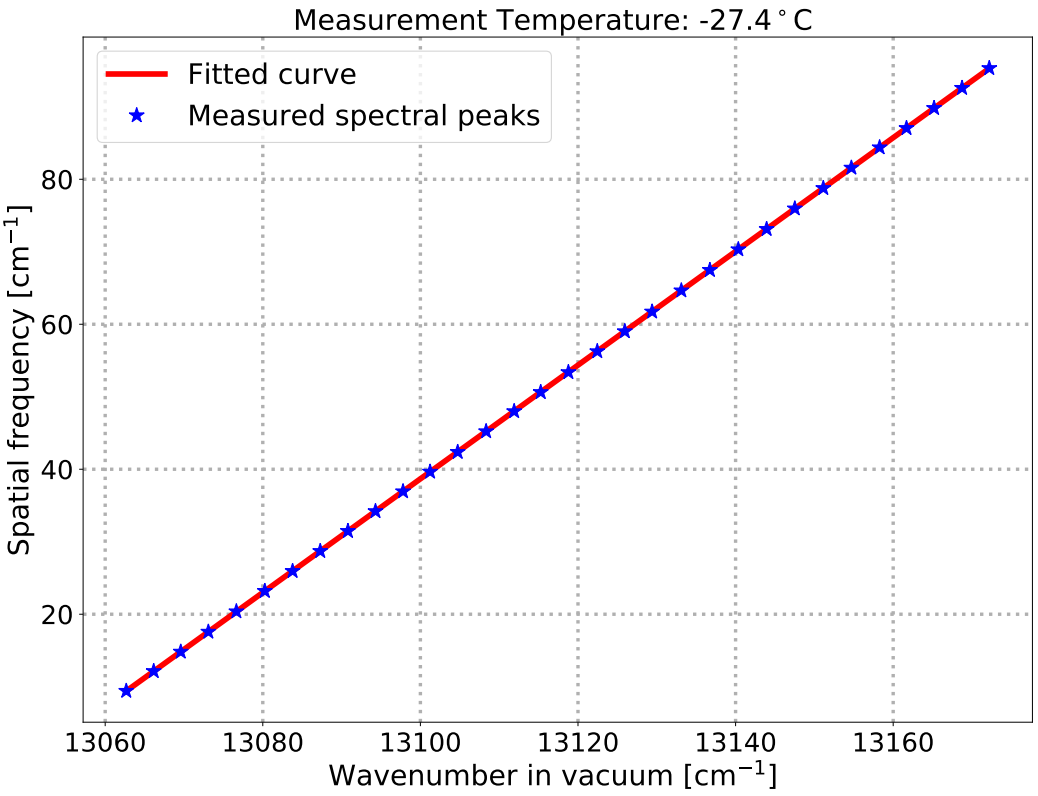

Figure 5.4: Spatial frequency of the interferogram vs the incident wavenumber at instrument temperature of -27.4°C. The estimated Littrow wavenumber is 13050.688 cm^{-1}, the corresponding Littrow angle is 6.600° and the magnification factor of the camera optics is 0.590. The estimated fitted standard deviation of the slope and intercept are 6.673e-5 and 8.754e-1, respectively.

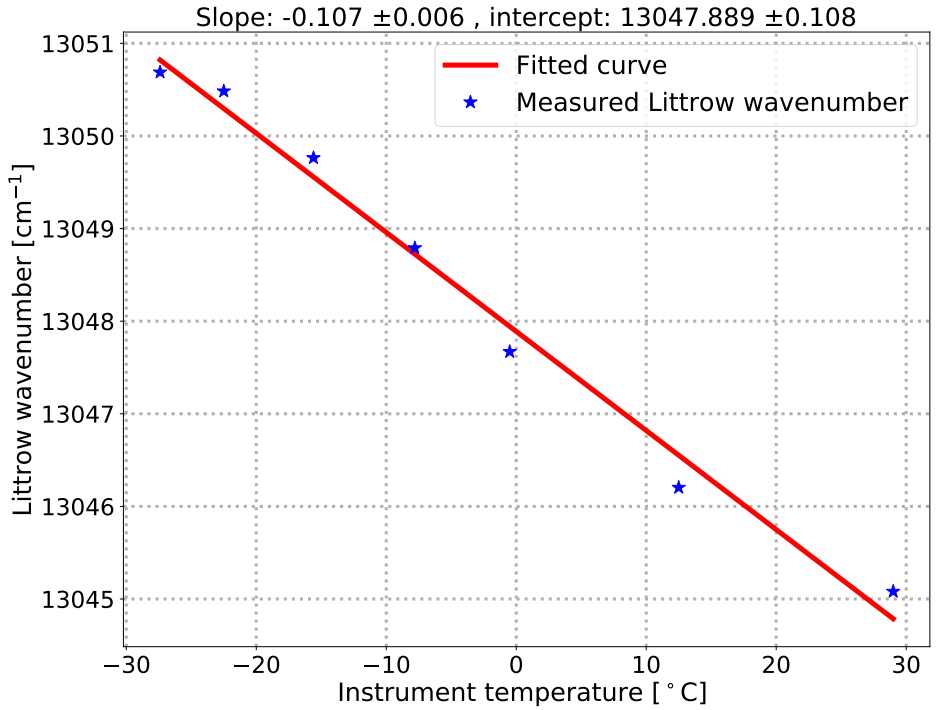

(a) Littrow wavenumber vs instrument temperature

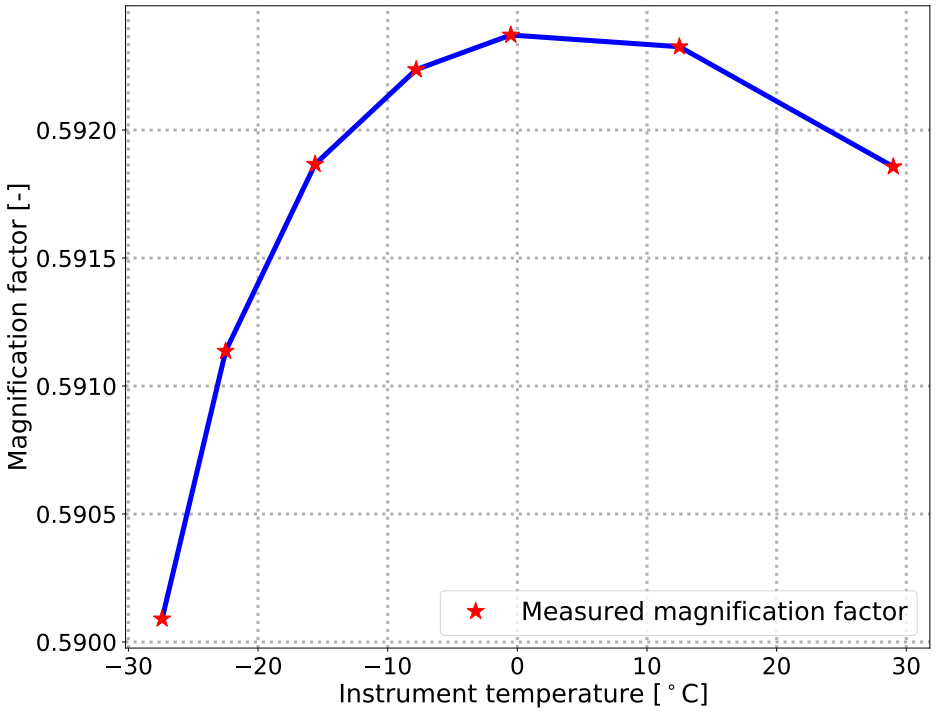

(b) Magnification factor vs instrument temperature

Figure 5.5: Estimated Littrow wavenumbers and magnification factors of the camera optics at different instrument temperatures.

5.5 Phase Distortion Correction

As mentioned in Section 5.1, for an monochromatic spectral radiation $B(\sigma)$, the recorded intensity distribution is given by:

$$I_\sigma(x) = B(\sigma) + B(\sigma)A(x,\sigma)\varepsilon(x,\sigma)cos(2\pi f_x x + \varphi(x,\sigma)). \tag{5.5}$$

Equation 5.5 can be rewritten in exponential form:

$$\begin{aligned} I_\sigma(x) = B(\sigma) &+ \frac{1}{2}B(\sigma)A(x,\sigma)\varepsilon(x,\sigma)e^{i[2\pi f_x x+\varphi(x,\sigma)]} \\ &+ \frac{1}{2}B(\sigma)A(x,\sigma)\varepsilon(x,\sigma)e^{-i[2\pi f_x x+\varphi(x,\sigma)]} \end{aligned} \tag{5.6}$$

The purpose of the phase correction is to remove the phase distortion term $\varphi(x,\sigma)$ from the original interferogram. As discussed in detail by Harlander (*Englert et al.*, 2004; *Harlander et al.*, 2019a), $\varphi(x,\sigma)$ can be obtained by a spectral isolation method.

Firstly, the DC and low frequency components were removed by blocking the low frequency components in the spectral domain. Then another isolation window function was used to isolate one of the conjugate spectral peaks. IFFT was performed with this isolated spectral peak to get a complex interferogram $I_\sigma(x)_{modulation}$ in the spatial domain:

$$I_\sigma(x)_{modulation} = \frac{1}{2}B(\sigma)A(x,\sigma)\varepsilon(x,\sigma)e^{i[2\pi f_x x+\varphi(x,\sigma)]}, \tag{5.7}$$

where the complex interferogram has the same amplitude and phase information as the original interferogram $I_\sigma(x)$.

The overall phase term $\Phi(x,\sigma) = 2\pi f_x x + \varphi(x,\sigma)$ can be obtained by performing an arctangent function on the complex interferogram. The calculated phase was wrapped within a modulo of 2π. It is necessary to unwrap it to retrieve the actual phase information.

Figure 5.6(a) shows the interferogram at 764.511 nm after removing the DC components and isolating the spectral peak. Figure 5.6(b) shows one slice at row 200 indicated by a red horizontal line in Figure 5.6(a). Figure 5.6(c) shows the retrieved wrapped phase and unwrapped phase at row 200. It is clearly seen that the modulo of 2π discontinuity has been removed to get a nearly linear trend curve, which is the actual phase term $\Phi(x,\sigma) = 2\pi f_x x + \varphi(x,\sigma)$.

The theoretical phase term $\Phi(x,\sigma)_{theoretical} = 2\pi f_x x$ can be calculated based on the Littrow calibration results in Section 5.4. Figure 5.7 shows the calculated theoretical and actual phase information at row 200 for the instrument temperature of -27.4°C and

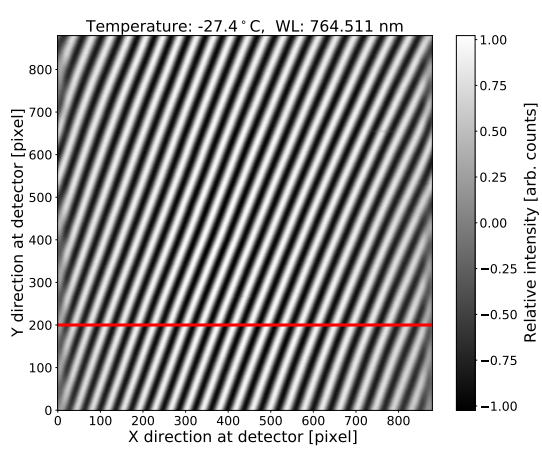

(a) Interferogram at 764.511 nm

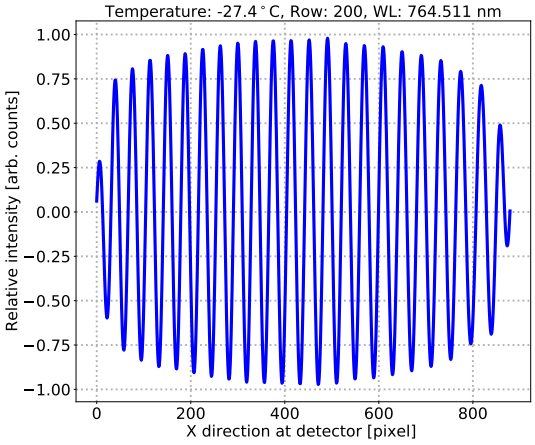

(b) One slice at row 200

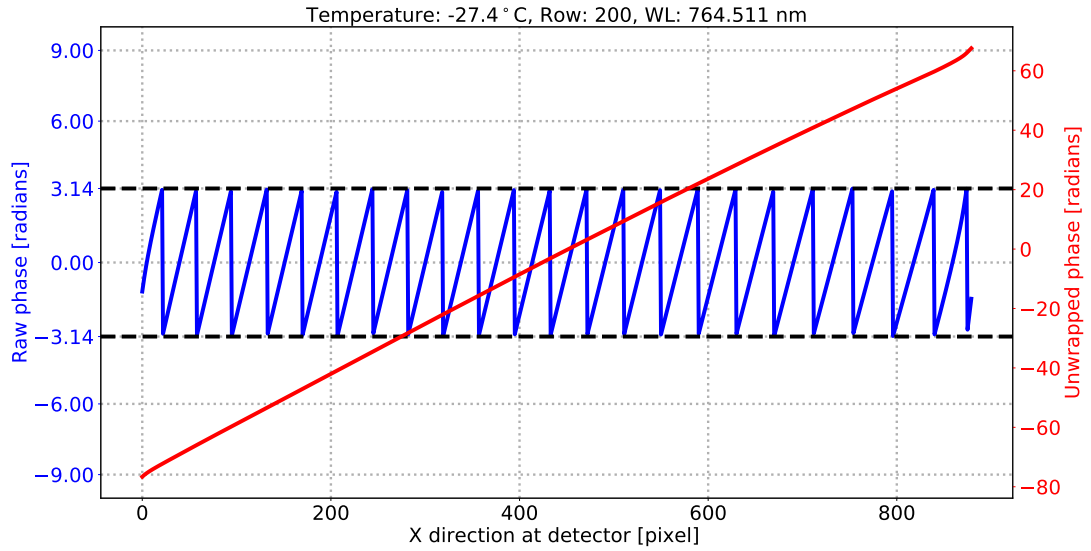

(c) Retrieved wrapped phase and unwrapped phase

Figure 5.6: Schematic diagram of the retrieved phase information. Figure 5.6(a) shows the interferogram at 764.511 nm after removing the DC components and isolating the spectral peak. Figure 5.6(b) shows one slice at row 200 indicated by a red horizontal line in Figure 5.6(a). Figure 5.6(c) shows the retrieved wrapped phase and unwrapped phase at row 200.

different wavelengths.

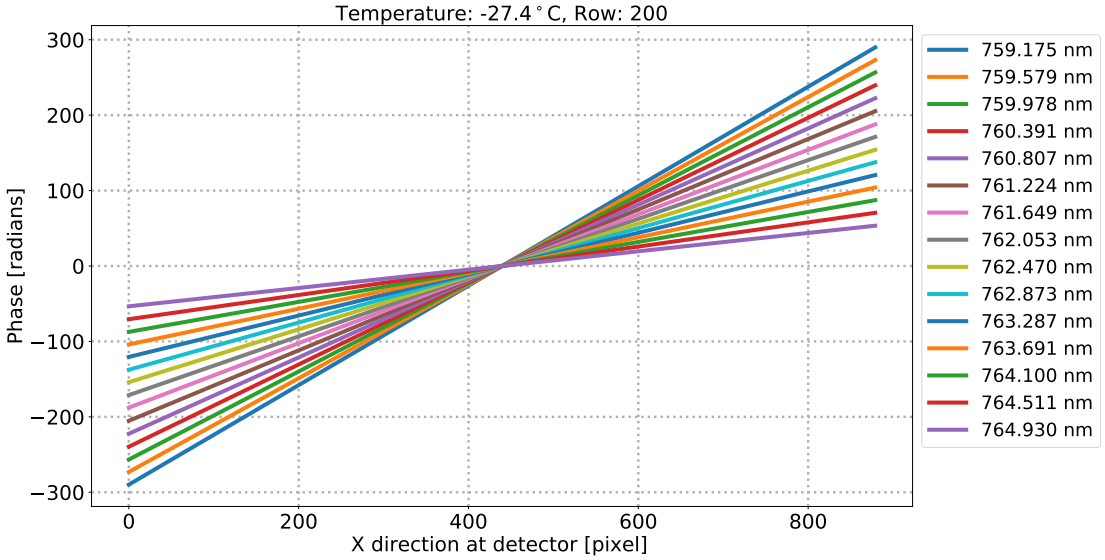

(a) Theoretical phase for different wavelengths

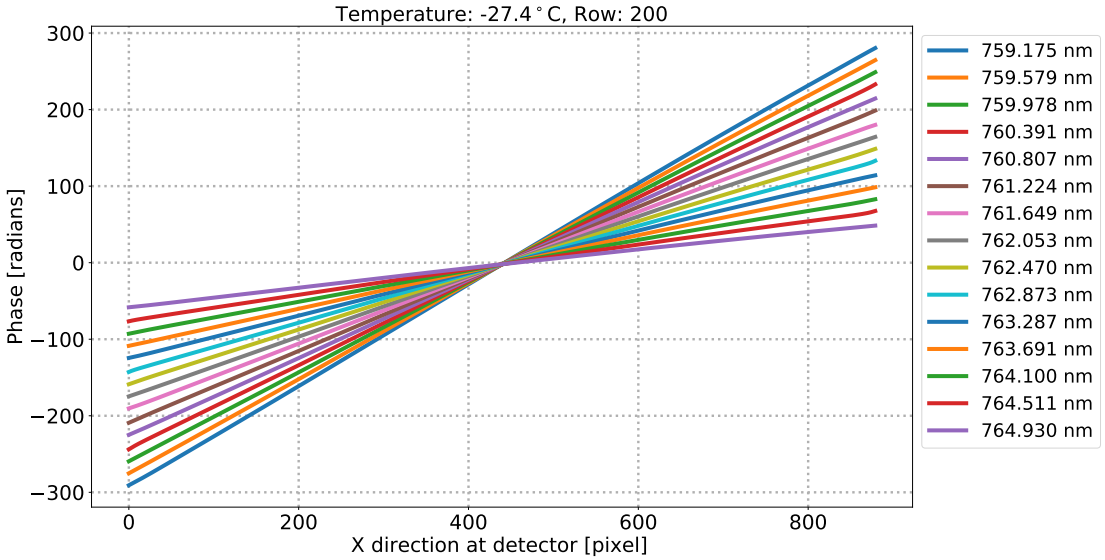

(b) Actual phase for different wavelengths

Figure 5.7: Calculated the theoretical and actual phase information at row 200 and the instrument temperature of -27.4°C for different wavelengths.

Then the phase distortion term can be obtained by $\varphi(x,\sigma) = \Phi(x,\sigma) - \Phi(x,\sigma)_{theoretical}$, as shown in Figure 5.8. It is found that the phase distortion term

$\varphi(x,\sigma)$ of the instrument FM varies slowly with the position x and the incident wavenumber σ. Especially at the effective ROI near the zero OPD position, the frequency-independent phase distortion is dominant.

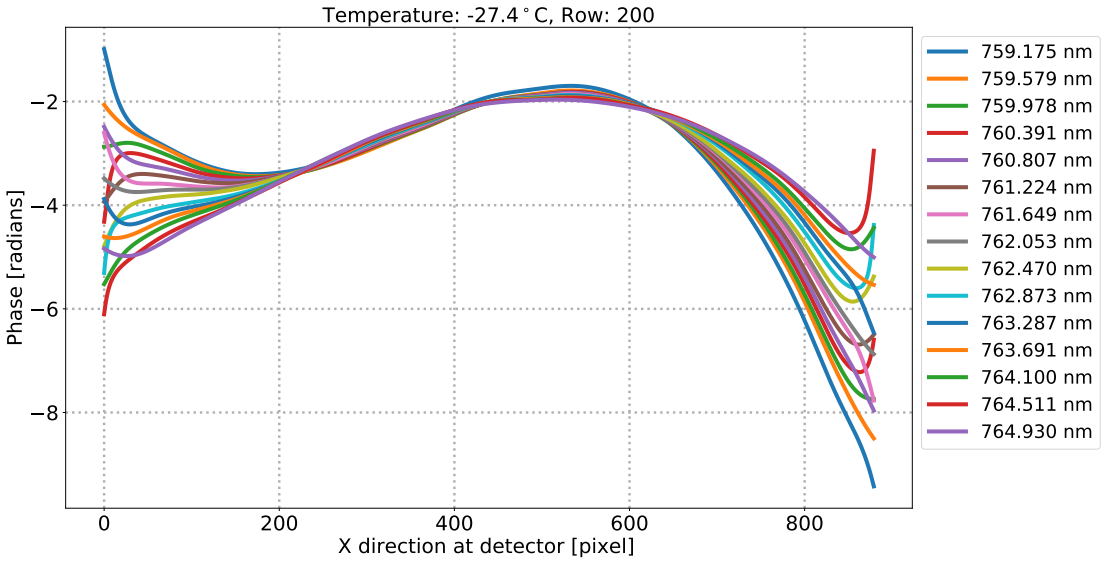

Figure 5.8: Phase distortion at row 200 for different wavelengths.

The phase distortion corrected interferogram can be obtained by multiplying the original interferogram with the negative exponential term of the phase distortion term. Figure 5.9 shows the interferogram at 764.722 nm before and after phase correction, where the tilt angle of the interferogram has been corrected.

Figure 5.10 shows the constructed polychromatic interferogram by superimposing multiple phase distortion corrected monochromatic interferograms. Compared with Figure 5.3, the modulation along the y-axis within the barber-pole has been removed, which indicates the validity of the phase correction method.

5.6 Amplitude Variation Estimation

After the phase distortion correction, the modulated normalized interferogram can be expressed as:

$$I_\sigma(x)_{corrected} = A(x,\sigma)\varepsilon(x,\sigma)e^{i(2\pi f_x x)}, \tag{5.8}$$

where $A(x,\sigma)\varepsilon(x,\sigma)$ represents the final modulation efficiency or visibility at the position x and wavenumber σ, and it can be estimated from the amplitude of the phase corrected complex interferogram, as shown in Figure 5.11. The red line in Figure 5.11

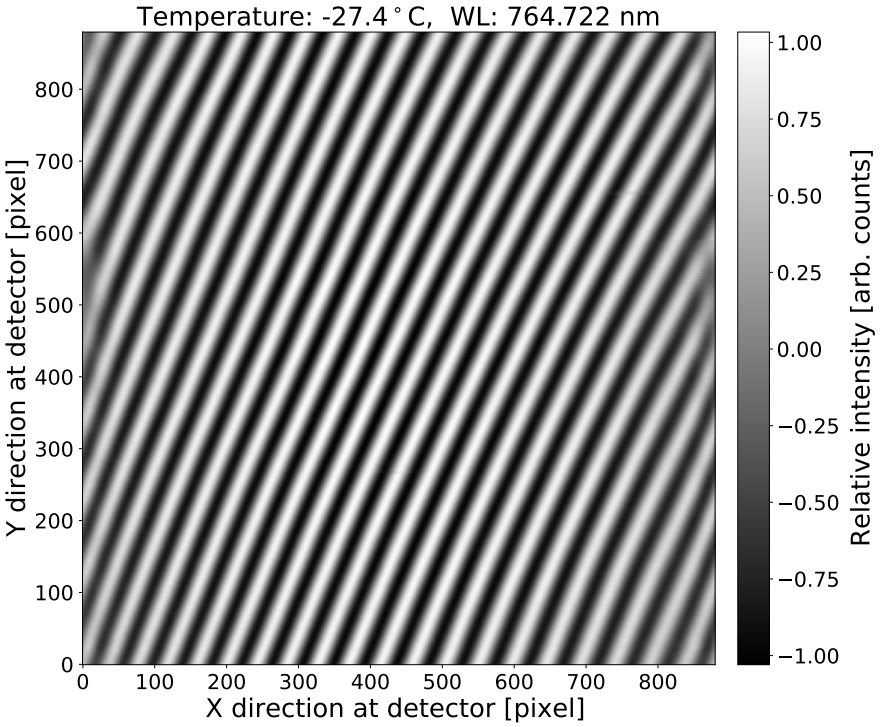

(a) Interferogram at 764.722 nm before phase correction

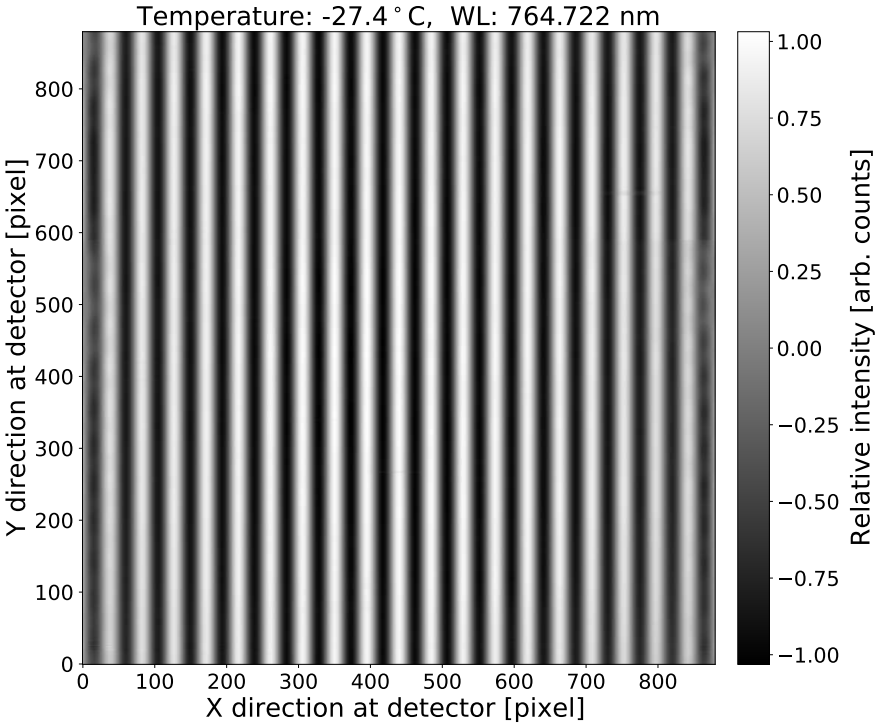

(b) Interferogram at 764.722 nm after phase correction

Figure 5.9: Phase correction interferogram sample at 764.722 nm.

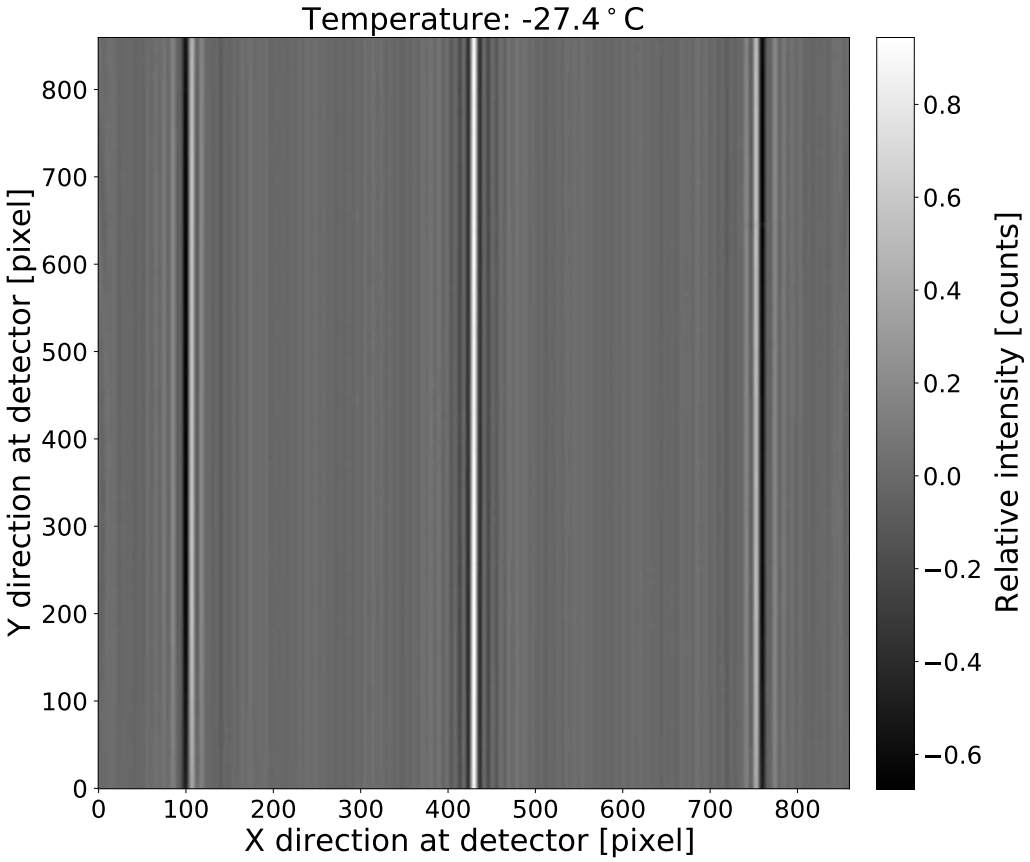

Figure 5.10: Constructed polychromatic interferogram by superimposing multiple phase distortion corrected monochromatic interferograms.

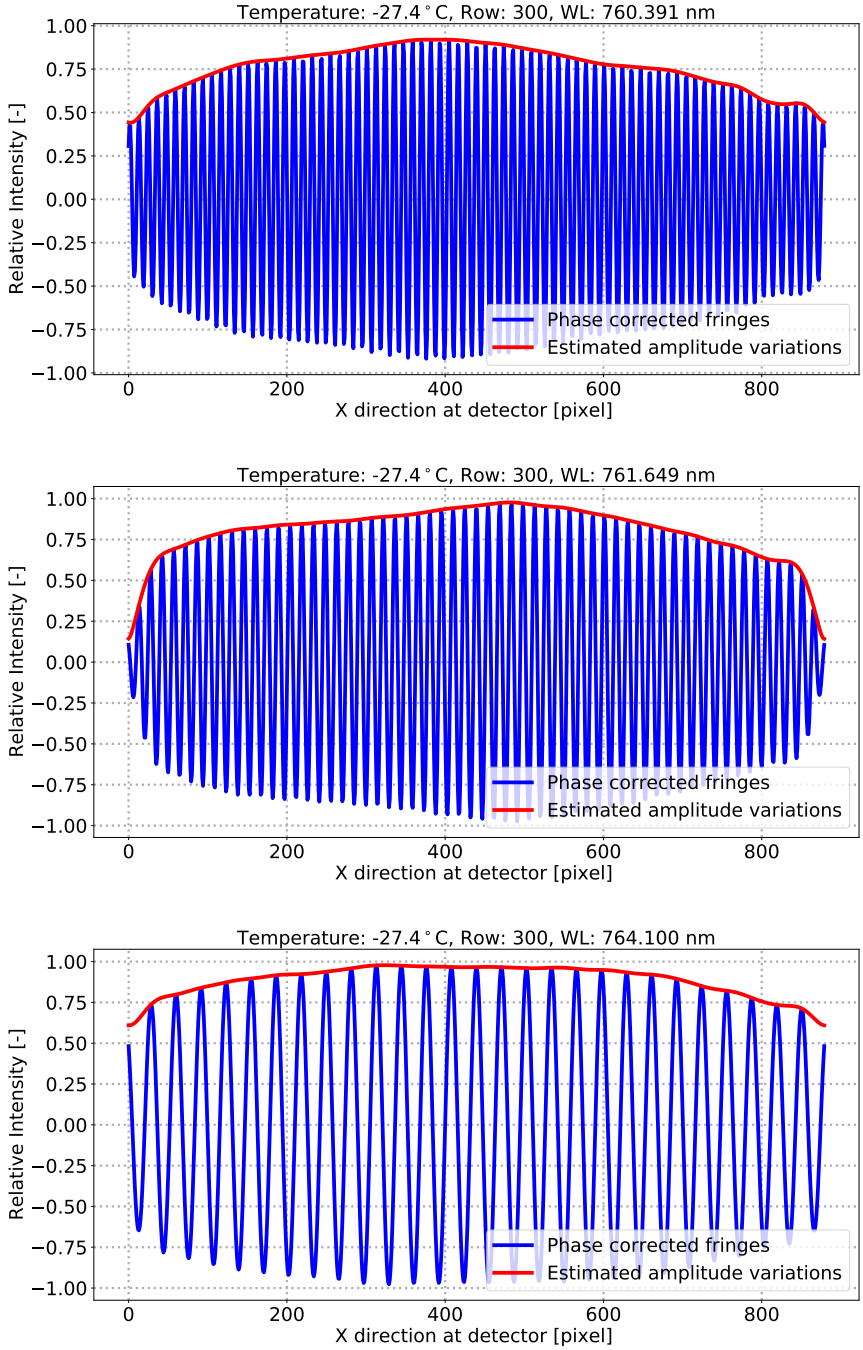

Figure 5.11: Estimated amplitude variation at row 300 for different wavelengths.

is the estimated amplitude variation $A(x,\sigma)\varepsilon(x,\sigma)$. The amplitude calculation was done row by row to obtain the final amplitude calibration matrix at each wavelength and tem-

perature.

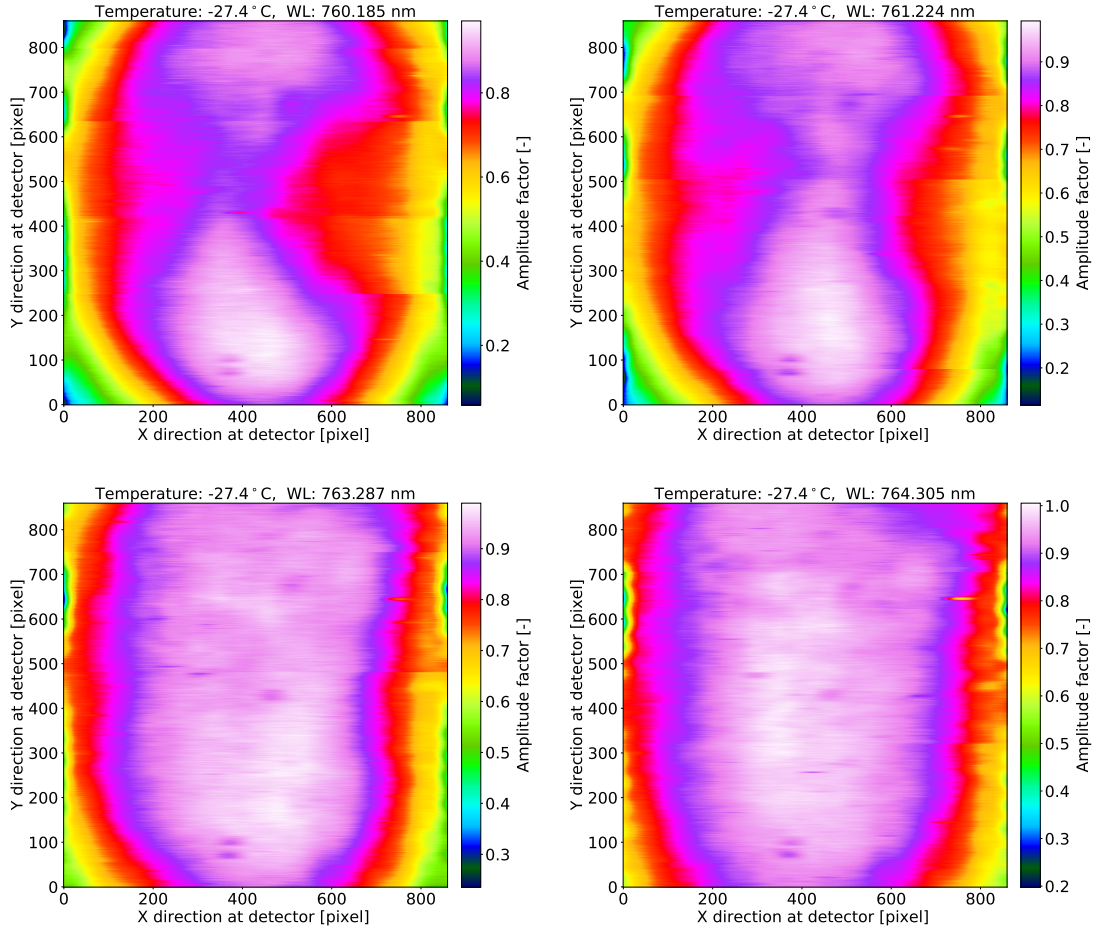

Figure 5.12: Amplitude calibration matrices at different wavelengths.

Figure 5.12 shows the obtained amplitude calibration matrices at different wavelengths for the instrument temperature of -27.4°C. Figure 5.13 shows the obtained amplitude calibration matrices at about 760.185 nm for different instrument temperatures. Figure 5.14 shows the difference image between the estimated amplitudes at about 760.185 nm for the instrument temperatures of -27.4°C and 29.0°C. The mean difference is 0.0056, the median difference is 0.0025, and the standard deviation is 0.023, which indicates that the temperature dependence of the amplitude variation $A(x,\sigma)\varepsilon(x,\sigma)$ is almost negligible. This is consistent with the temperature change trend of the measured magnification factor of the camera optics in Section 5.4.

Once the amplitude variation of the ACU is measured, the modulation efficiency matrix can be obtained by dividing the amplitude calibration matrix by the amplitude

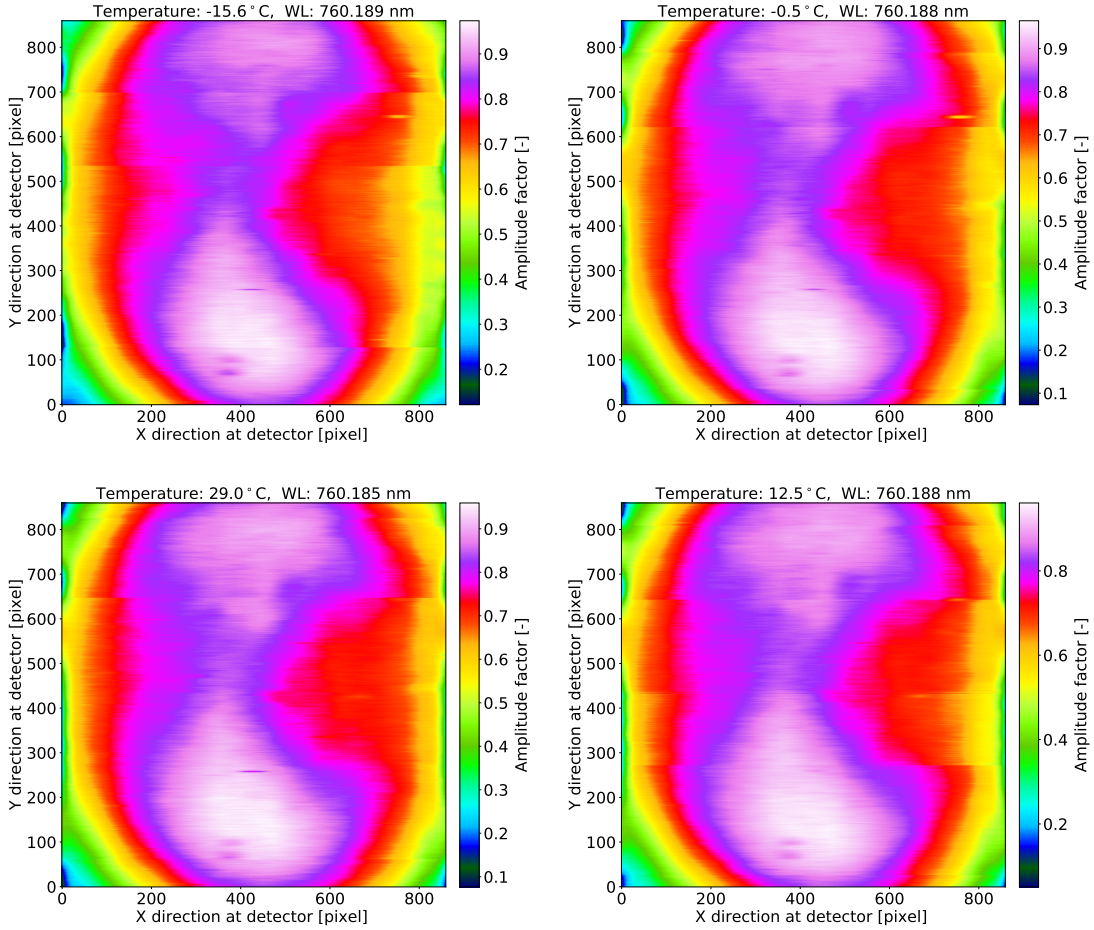

Figure 5.13: Amplitude calibration matrices at about 760.185 nm for different instrument temperatures.

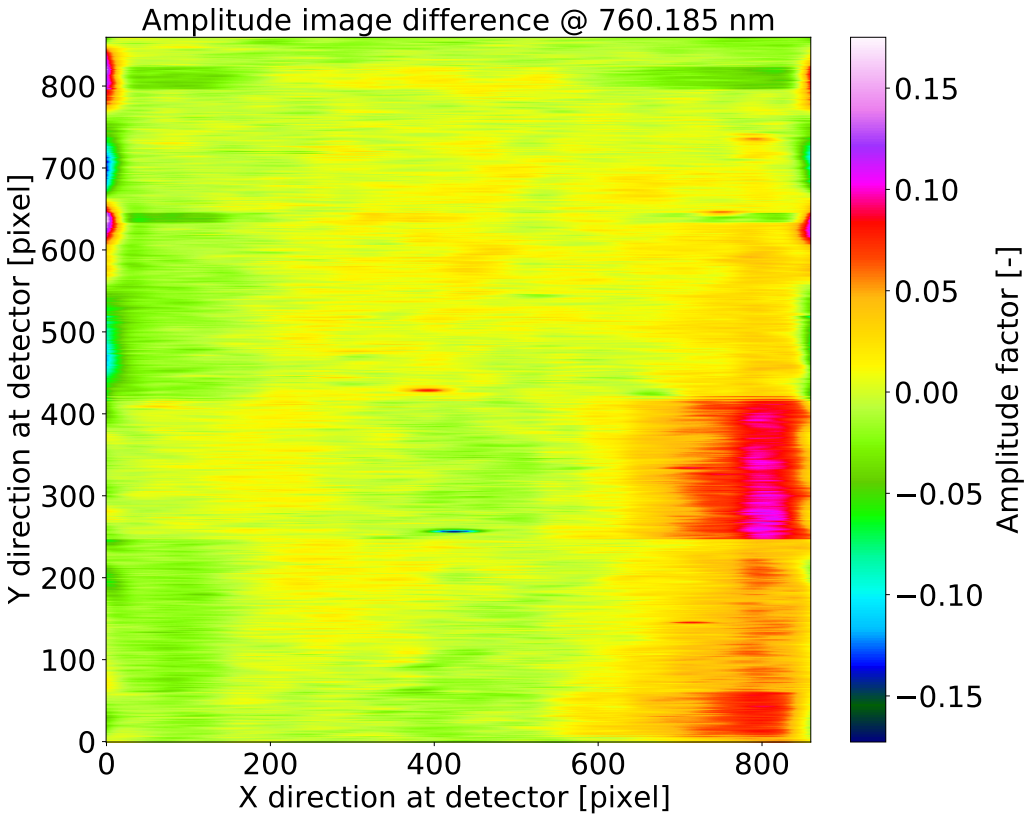

Figure 5.14: Difference between the estimated amplitudes at about 760.185 nm for the instrument temperatures of -27.4°C and 29.0°C.

variation profile of the ACU for further in-orbit measurement processing, which is not included in this thesis. In addition, the amplitude variation for the different aperture stops will be presented in *Ntokas* (2022).

5.7 Chapter Summary

This chapter described the characterization and calibration results of the FM and presented the procedure to obtain the amplitude calibration matrix at different wavelengths and temperatures, including the dark and bias current subtraction, spike correction, removal of the DC and low frequency components, Littrow wavelength calibration, phase distortion correction and amplitude variation estimation. The Littrow calibration results show

that there is a linear trend of temperature dependence:

$$\sigma_0 = (-0.107 \pm 0.006)\frac{cm^{-1}}{^{\circ}C} * T + (13047.889 \pm 0.108)cm^{-1}.$$

The expected thermal drift value for the Littrow wavenumber should be less than 1 cm^{-1} over the nominal operating temperature range (*Wroblowski*, 2022), but the measured thermal drift of the Littrow wavenumber is up to 6 cm^{-1}. This means that the actual Littrow wavelength in the in-orbit measurements will shift towards the shorter wavelengths, resulting in the spectral overlap. Therefore, the ghost line removal needs to be considered for the in-orbit measurements.

From -27.4°C to 29°C, the mean of the magnification factors of the camera optics is 0.592 and the corresponding standard deviation is 0.00076, which indicates that the magnification factor of the camera optics remains nearly stable over the nominal operating temperature range. Since the visibility of the instrument is mainly dependent on the performance of the camera optics, this implies that the visibility of the instrument varies less with temperature. This is verified in the subsequent amplitude variation calculations. Finally, the amplitude calibration matrix at different wavelengths and temperatures is obtained. Once the amplitude variation of the ACU is measured, the modulation efficiency matrix can be obtained by dividing the amplitude calibration matrix by the amplitude variation profile of the ACU for further in-orbit measurement processing.

Chapter 6

Summary and Outlook

The main work of this thesis is to characterize and calibrate the AtmoLITE satellite instrument for the INSPIRESat-4 mission. The full characterization and calibration procedures were divided into three phases: before the SHS glueing for the AtmoLITE instrument, during and after the SHS glueing for the AtmoLITE instrument, and after finalising the integration of the SHS system. At each phase, corresponding measurement strategies and alignment procedures were presented.

Before the SHS glueing for the AtmoLITE instrument, wavefront error measurements were performed on the different SHS front and camera optics samples for the AtmoLITE instrument's qualification model and flight model. For the front optics, coma aberration is the dominant Zernike polynomial, which contributes the most to the overall WFEs. The strategy to find the optimum position of the last lens of the front optics is to obtain the minimal coma during alignment. For the camera optics, apart from the tilt and defocus aberrations, the spherical aberration contributes the most to the overall WFEs. The large defocus value of the camera optics in the simulation results is due to the fact that the camera optics is designed to compensate for the field curvature of the front optics, resulting in the localization plane in our new system not being a strictly plane. Finally, the front#3 and the camera#2 with the old optical design were selected for the QM. The camera#2 with the new optical design was utilised for the FM.

During and after the SHS glueing for the AtmoLITE instrument, a pinhole light source setup was built to adjust the position of the last lens of the front optics to find the optimum position with the smallest image point, in which the pinhole light source provided a nearly collimated light beam with a limited divergence angle. The detailed alignment procedures for the front optics and camera optics were introduced. The alignment result of the front optics showed that the measured spot size of 10 pixels matches the simulated result of 8 pixels with the alignment uncertainty about 2 pixels, which indicates that the alignment procedures for the front optics were correct and appropriate.

The goal of aligning the camera optics was to find a balance between the visibility of the edges and the middle of the image. The alignment result of the camera optics showed that the trend in visibility was in line with the designed expectations.

In order to verify the effectiveness of the designed vacuum compensator, the pinhole setup and field target measurements were performed. After moving the vacuum compensator for the vacuum environment, the measured spot size is two to three times larger than the simulated spot size. This will reduce our spatial resolution by a factor of about two or three. Meanwhile, the variation of the spot size at different temperatures was investigated. The results showed that the spot size imaged by the pinhole setup increases as the temperature decreases, which indicates that due to the use of aluminium as an optomechanical material, the effect of its thermal expansion on the optical performance of the instrument should be further investigated for further missions. The imaging characteristics of the instrument should be re-evaluated using the moon as the imaging target during the in-orbit measurements. In addition, the transmission curve of the optical bandpass filter was measured and the results showed that the measured transmission curve in the top flat region agrees with the theoretical filter curve. The mean and standard deviation of the differences between the measured transmission curve and the theoretical filter curve between 760.0 nm and 765.0 nm are -0.00024 and 0.01054 respectively.

After finalising the integration of the SHS system, a series of interferogram measurements were performed at different wavelengths and temperatures in the vacuum environment, and corresponding calibration procedures were discussed, which mainly include the dark and bias current subtraction, spike correction, removal of the DC and low frequency components, Littrow wavelength calibration, phase distortion correction and amplitude variation estimation. The Littrow calibration results showed that there is a linear trend of temperature dependence. The expected thermal drift value for the Littrow wavenumber should be less than 1 cm^{-1} over the nominal operating temperature range, but the measured thermal drift of the Littrow wavenumber is up to 6 cm^{-1}. This means that the actual Littrow wavelength in the in-orbit measurements will shift towards the shorter wavelengths, resulting in the spectral overlap. Therefore, the ghost line removal needs to be considered for the in-orbit measurements.

The amplitude calibration matrix at different wavelengths and temperatures was obtained, and the results showed that the temperature dependence of the amplitude variation $A(x,\sigma)\varepsilon(x,\sigma)$ is almost negligible. This is consistent with the temperature change trend of the measured magnification factor of the camera optics. Once the amplitude variation of the ACU is measured, the modulation efficiency matrix can be obtained by dividing the amplitude calibration matrix by the amplitude variation profile of the ACU for further in-orbit measurement processing.

Appendix A

A.1 Field imaging measurement of the instrument before moving the vacuum compensation for the different scenes

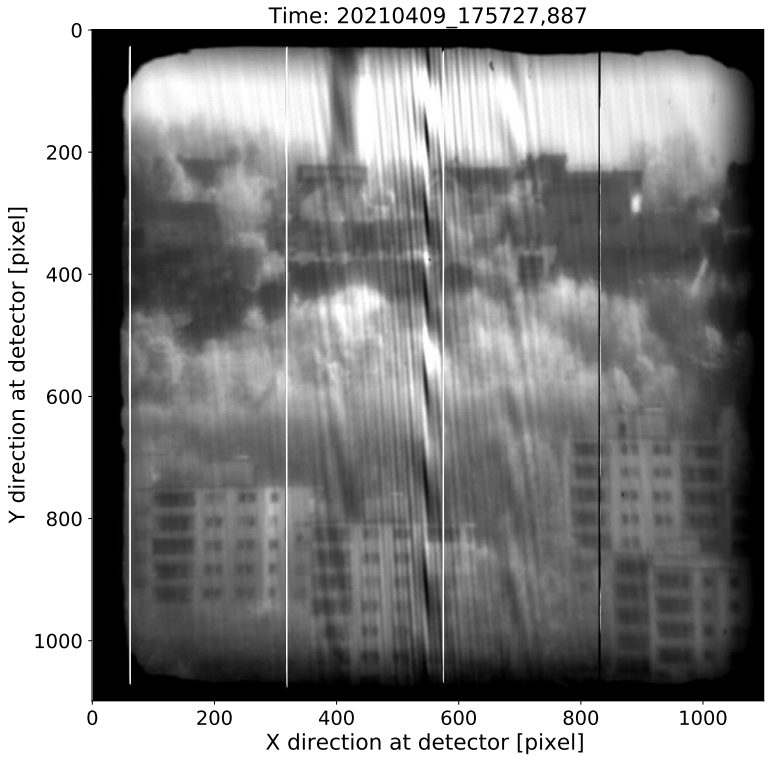

Figure A.1: Field imaging measurement of the instrument before moving the vacuum compensation, which includes the bottom of the telecommunication tower.

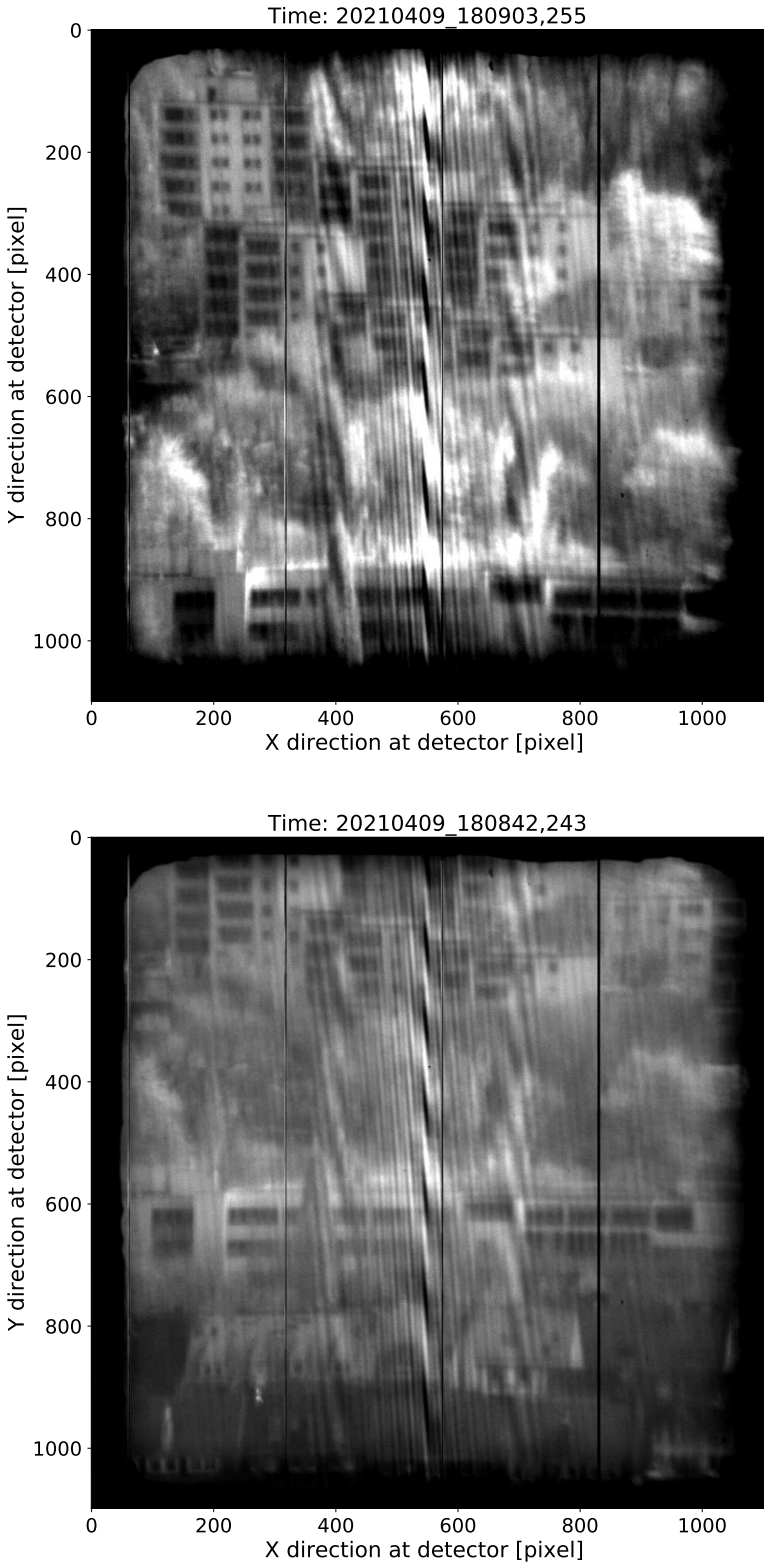

Figure A.2: Field imaging measurement of the instrument before moving the vacuum compensation for the different scenes.

A.2 The off-axis measurements for the camera#3 of the FM

Table A.1 gives the summarised measurement data of the camera#3 of the FM for the off-axis measurements.

Table A.1: Calculated wavefront performance of the camera#3 of the FM for the off-axis measurements, where '$0.0° \pm 0.05°$' represents the initial measurement angle.

Optic	Camera#3		Camera#3		Camera#3	
Field Angle	$0.0° \pm 0.05°$		$0.1° \pm 0.05°$		$0.2° \pm 0.05°$	
Unit	P-V [λ]	RMS [λ]	P-V [λ]	RMS [λ]	P-V [λ]	RMS [λ]
Tilt	0.73	0.18	0.91	0.23	0.64	0.16
Defocus	0.20	0.06	0.41	0.12	0.40	0.11
Coma	0.73	0.13	0.70	0.12	0.74	0.13
Astigmatism	0.21	0.04	0.22	0.05	0.22	0.04
Spherical Ab.	0.52	0.15	0.48	0.14	0.49	0.14
Optic	Camera#3		Camera#3		Camera#3	
Field Angle	$0.3° \pm 0.05°$		$0.4° \pm 0.05°$		$0.5° \pm 0.05°$	
Unit	P-V [λ]	RMS [λ]	P-V [λ]	RMS [λ]	P-V [λ]	RMS [λ]
Tilt	0.57	0.14	1.24	0.31	1.03	0.26
Defocus	0.26	0.08	0.30	0.09	0.60	0.17
Coma	0.69	0.12	0.60	0.11	0.58	0.10
Astigmatism	0.21	0.04	0.17	0.03	0.16	0.03
Spherical Ab.	0.47	0.14	0.45	0.13	0.44	0.13
Optic	Camera#3		Camera#3			
Field Angle	$0.6° \pm 0.05°$		$0.7° \pm 0.05°$			
Unit	P-V [λ]	RMS [λ]	P-V [λ]	RMS [λ]		
Tilt	0.69	0.17	0.66	0.17		
Defocus	0.75	0.22	0.24	0.07		
Coma	0.54	0.10	0.56	0.10		
Astigmatism	0.16	0.03	0.17	0.04		
Spherical Ab.	0.42	0.13	0.41	0.12		

A.3 The alternative version of the glass materials

Figure A.3 shows the RMS wavefront field maps for the original and substituted glasses materials of the front and camera optics for the AtmoLITE at 20.0 °C and 0.0 Pa. The maximum RMS wavefront error for the original and substituted glasses material versions are 0.141789 waves and 0.145660 waves, respectively. The minimum RMS wavefront error for the original and substituted glasses material versions are 0.048763 waves and 0.058153 waves, respectively. The difference between the two versions is almost 0.01 waves, which can be negligible.

Figure A.4 presents the OPD across the pupil position of the AtmoLITE for the original and substituted glasses materials versions at the on-axis field. Figure A.5 shows the corresponding off-axis situation. For both field situations, the maximum difference between the two glasses materials versions is less than 0.08 waves.

In order to compare the image performance of the two different glass material versions, Figure A.6 shows the spot diagrams of the on-axis field at the image plane refer to the chief ray for the original and substituted glasses materials versions. Figure A.7 shows the corresponding off-axis situation. The spot diagram is the tracing bundles of rays from the object plane with the specific FOV through the optical system to the image surface to show the ray distributions. It provides the RMS spot radius which describes the distribution range of the most image points in the spot diagram, and the geometric (GEO) spot radius which describes the actual geometric radius of the dispersion image points. For the on-axis field, the RMS radii of the two different glasses materials versions are 2.318 μm and 2.885 μm, and the GEO radii of the two versions are 6.544 μm and 8.209 μm. For the off-axis field, the RMS radii of the two versions are 3.790 μm and 4.202 μm, and the GEO radii of the two versions are 12.593 μm and 12.351 μm. The maximum difference between the two versions is 1.665 μm, which meets the designed spatial resolution requirement.

Figure A.8 shows the distortion maps referring to the wavelength at 0.76646 μm with the grid of 27 $\times$27 points for the original and substituted glasses materials versions, where the size of the image plane is 9.23 mm $\times$ 9.22 mm, corresponding to roughly 840 pixels $\times$ 840 pixels to be illuminated. For the version of the original material, the maximum distortion is 3.2704% at the edge of the image. For the Chinese materials version, the maximum distortion is 2.4814% at the edge of the image. Both versions get a similar distortion map.

Furthermore, the modulation transfer function (MTF) of the system also reflects the transfer response capability to the fringes with specific spatial frequencies at the object plane. Figure A.9 displays the MTF curves of the different materials versions at the image plane, where the difference between the two versions is less than 0.1.

From the foregoing analysis, comparing the output of the RMS wavefront field maps, OPD maps, spot diagrams, grid distortion maps and MTF curves of the two glasses materials versions, both provide similar optical performance, and the difference between each other still within the system designed requirements. Pure Chinese glasses version of the front and camera optics for the AtmoLITE is a suitable candidate.

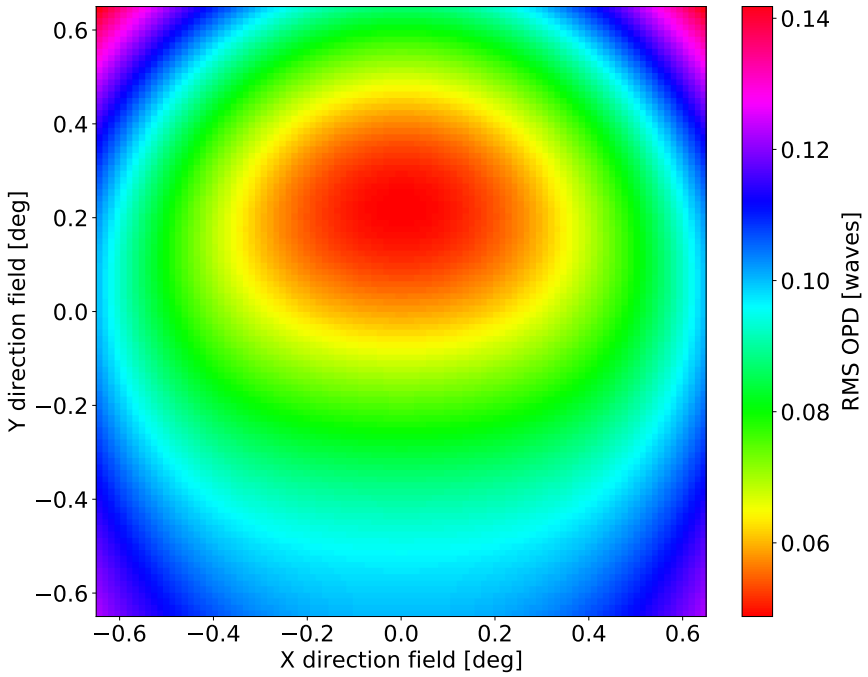

(a) RMS wavefront field map for the original glasses materials with the sampling of 100×100

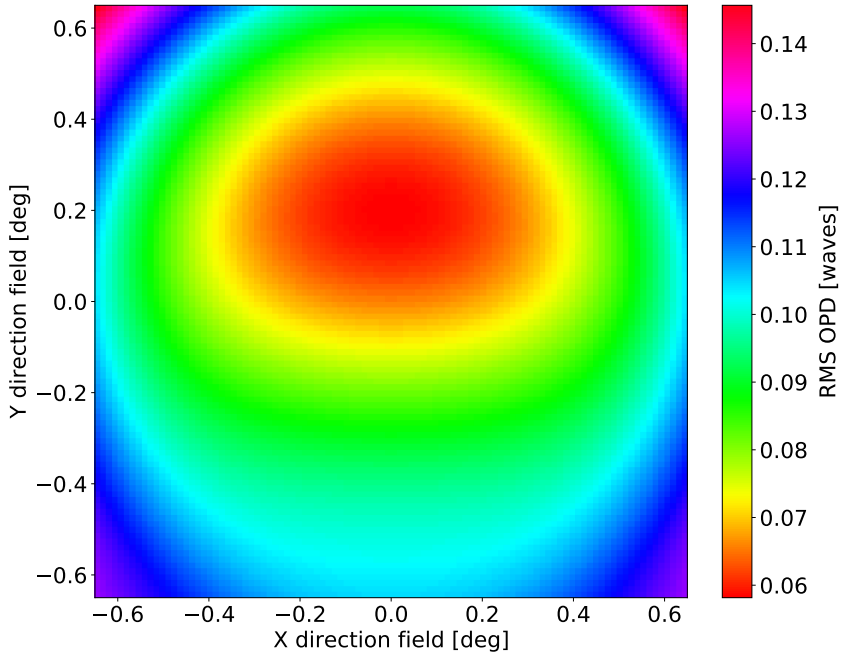

(b) RMS wavefront field map for the substituted Chinese glasses materials with the sampling of 100×100

Figure A.3: RMS wavefront field maps for the original and substituted glasses materials of the front and camera optics for the AtmoLITE.

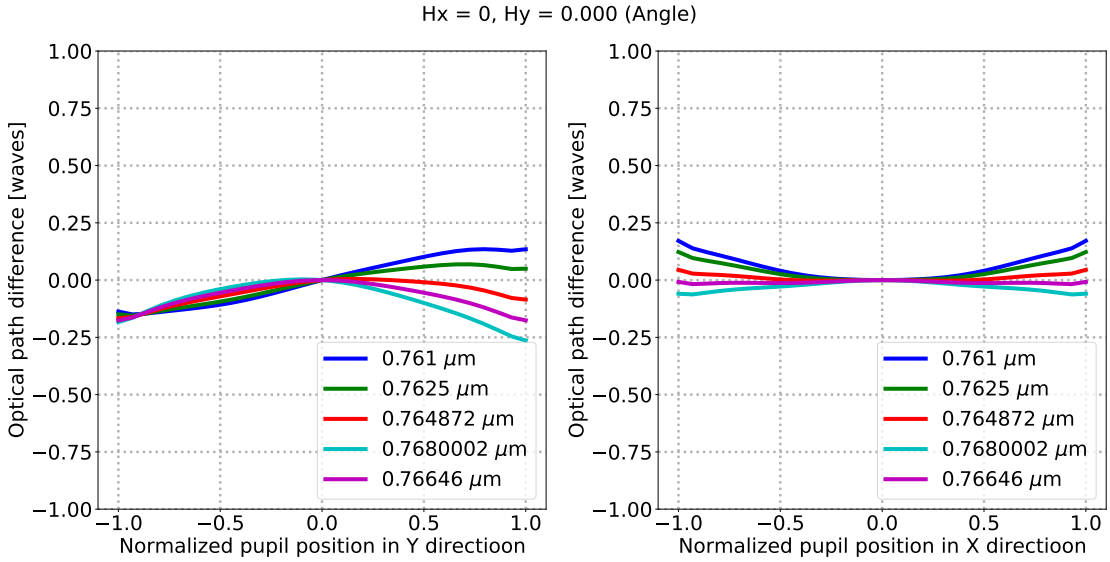

(a) OPD vs Pupil position of the on-axis field for the original glasses materials

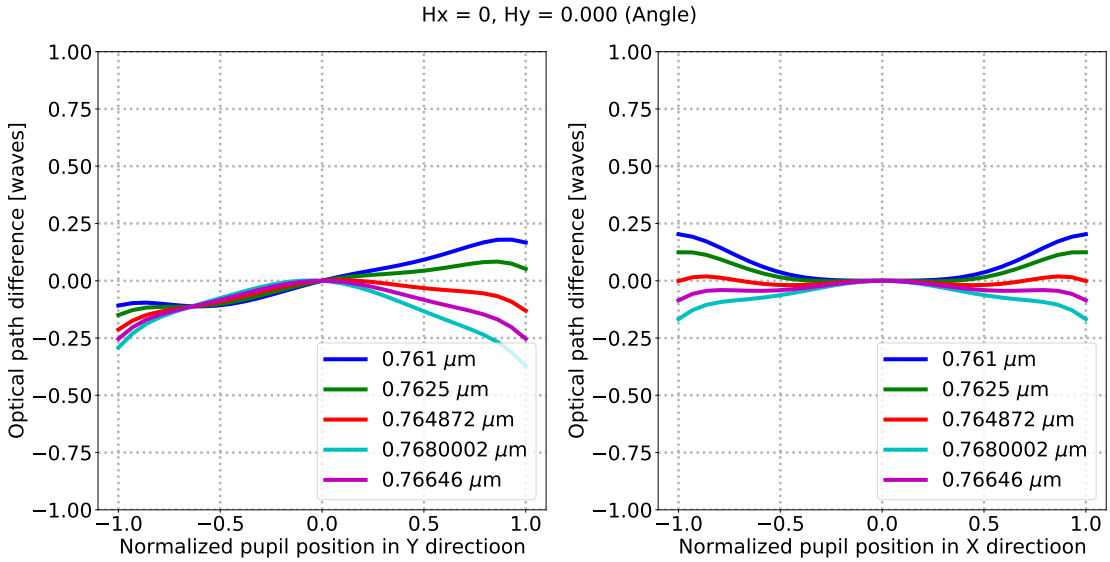

(b) OPD vs Pupil position of the on-axis field for the substituted Chinese glasses materials

Figure A.4: OPD vs Pupil position of the on-axis field for the original and substituted glasses materials versions on the tangential plane (left) and the sagittal plane (right).

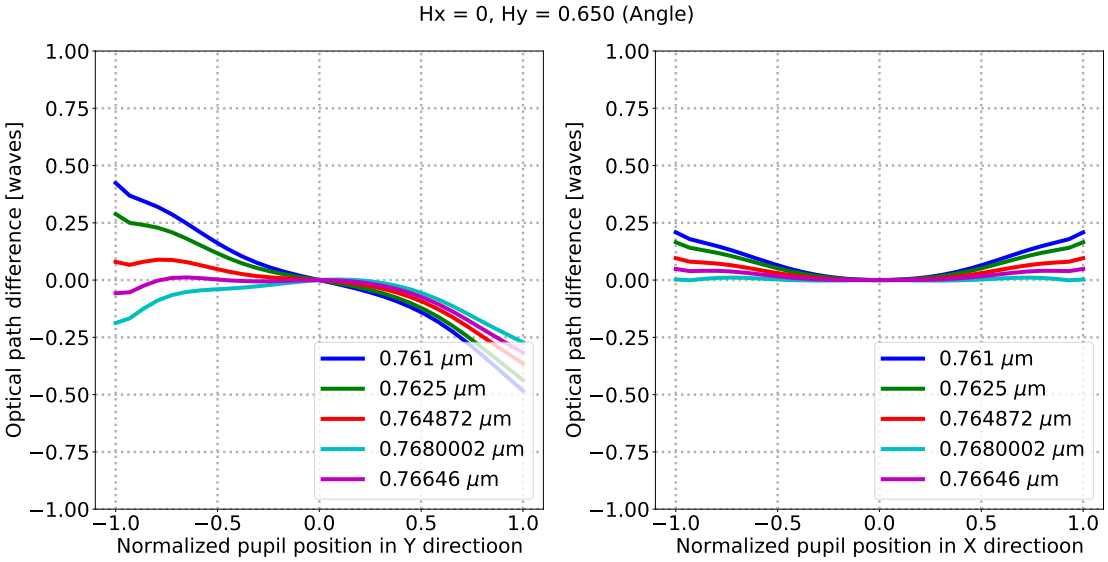

(a) OPD vs Pupil position of the off-axis field for the original glasses materials

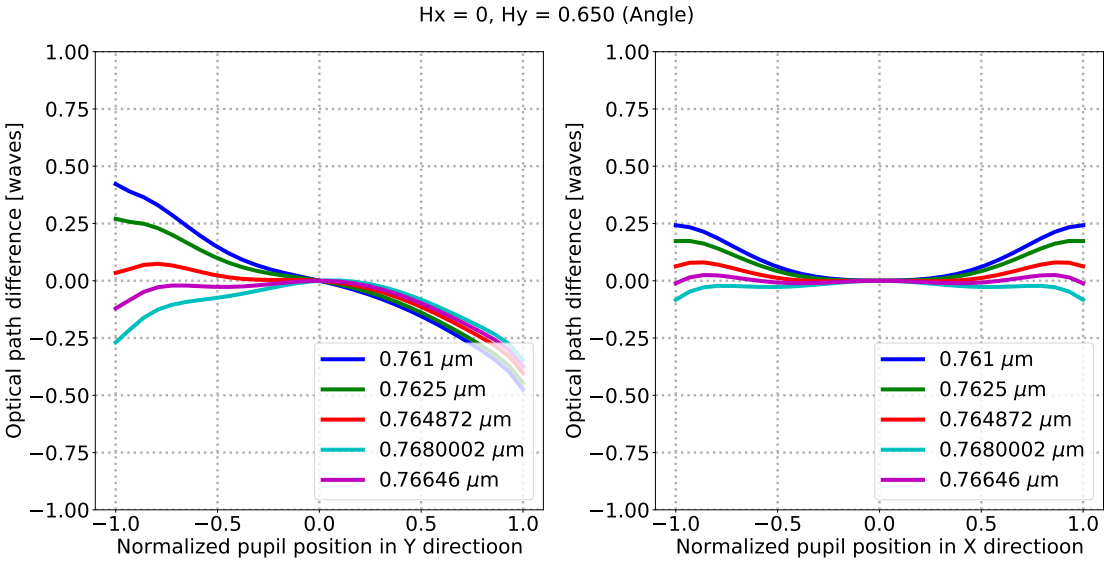

(b) OPD vs Pupil position of the off-axis field for the substituted Chinese glasses materials

Figure A.5: OPD vs Pupil position of the off-axis field for the original and substituted glasses materials versions on the tangential plane (left) and the sagittal plane (right).

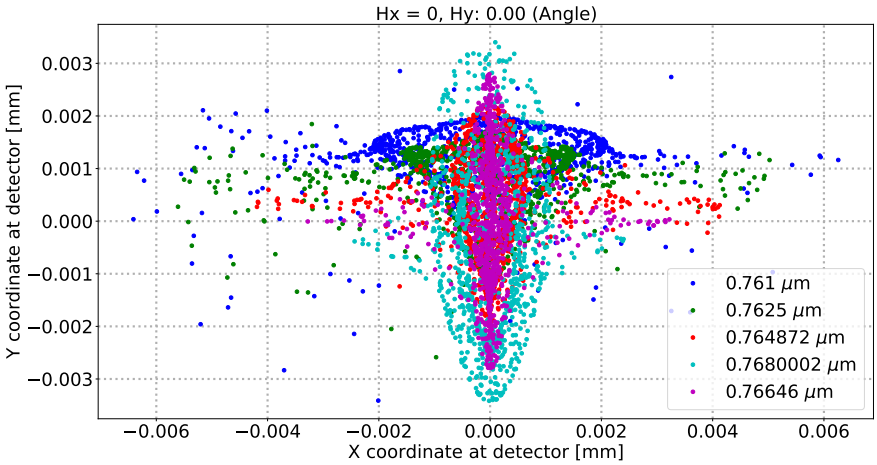

(a) Spot diagram of the on-axis field for the original glasses materials. RMS radius: 2.318 μm, GEO radius: 6.544 μm

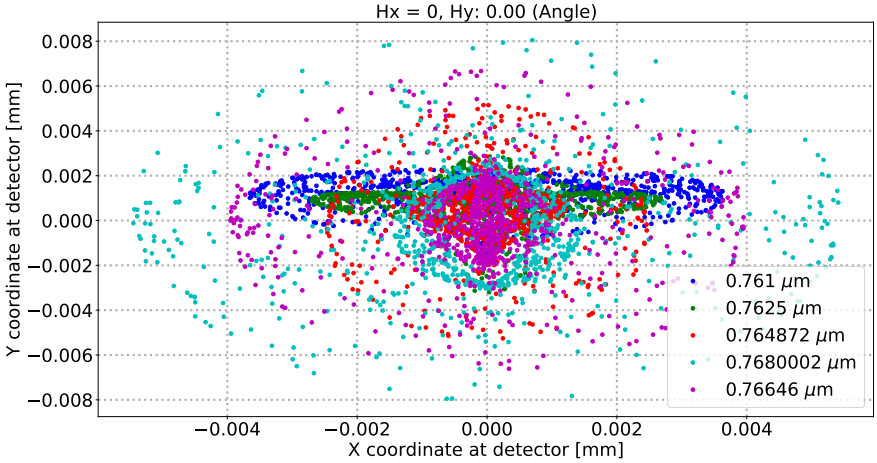

(b) Spot diagram of the on-axis field for the substituted Chinese glasses materials. RMS radius: 2.885 μm, GEO radius: 8.209 μm

Figure A.6: Spot diagrams of the on-axis field at the image plane for the original and substituted glasses materials versions.

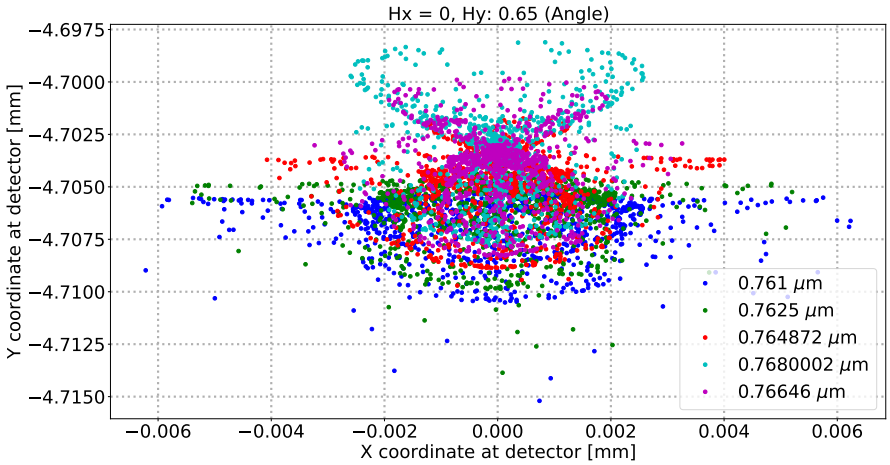

(a) Spot diagram of the off-axis field for the original glasses materials. RMS radius: 3.790 μm, GEO radius: 12.593 μm

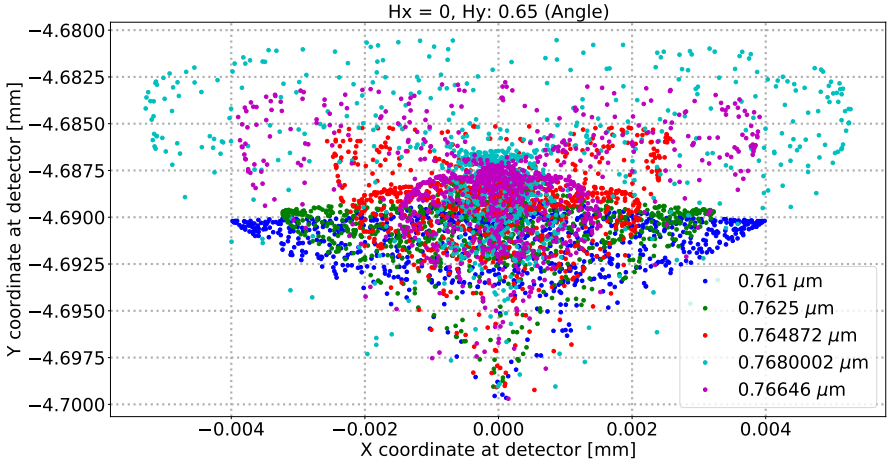

(b) Spot diagram of the off-axis field for the substituted Chinese glasses materials. RMS radius: 4.202 μm, GEO radius: 12.351 μm

Figure A.7: Spot diagrams of the off-axis field at the image plane for the original and substituted glasses materials versions.

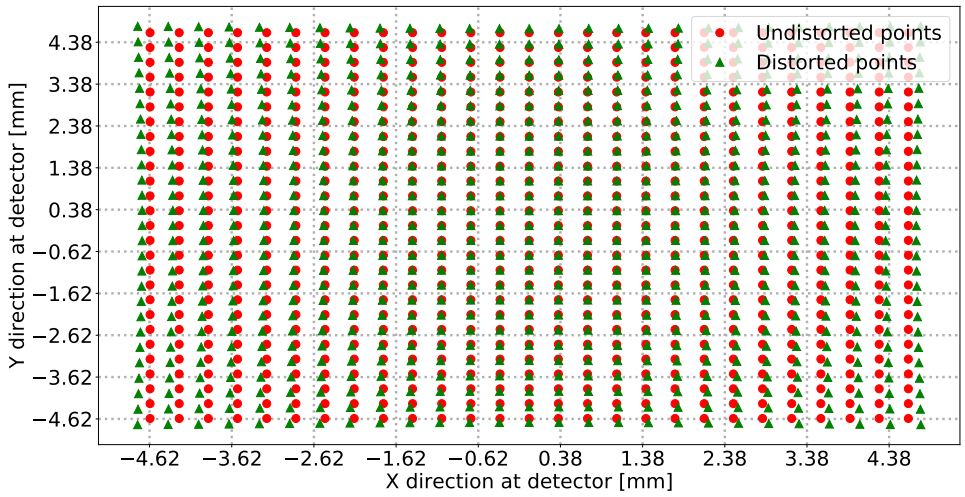

(a) Grid distortion map for the original glasses materials. The maximum distortion is 3.2704%.

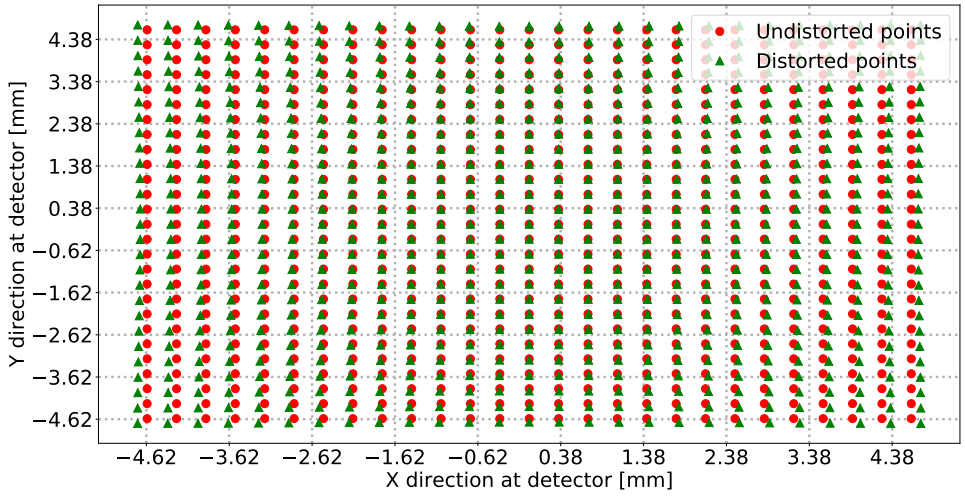

(b) Grid distortion map for the substituted Chinese glasses materials. The maximum distortion is 2.4814%.

Figure A.8: Gird distortion maps of the distorted and undistorted points by the ray-tracing simulation. The girds are 27×27 points.

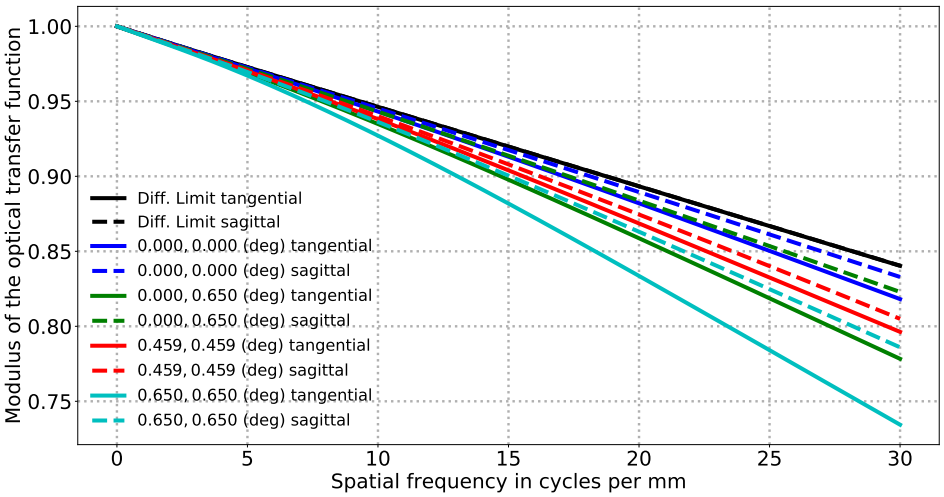

(a) MTF curve of the original glasses materials version

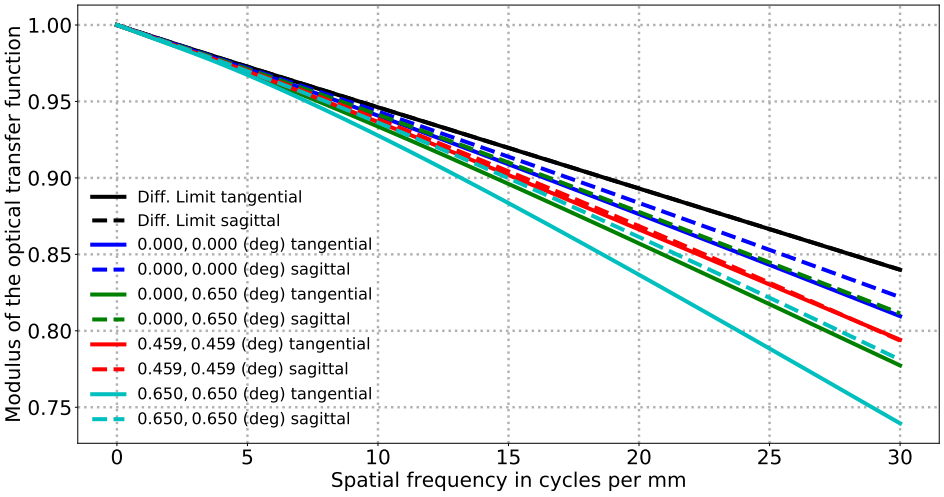

(b) MTF curve of the substituted Chinese glasses materials version

Figure A.9: MTF curves of the different materials versions at the image plane. The maximum spatial frequency is plotted to 30 mm^{-1}.

A.4 Spot diagrams of the FM at the different field points

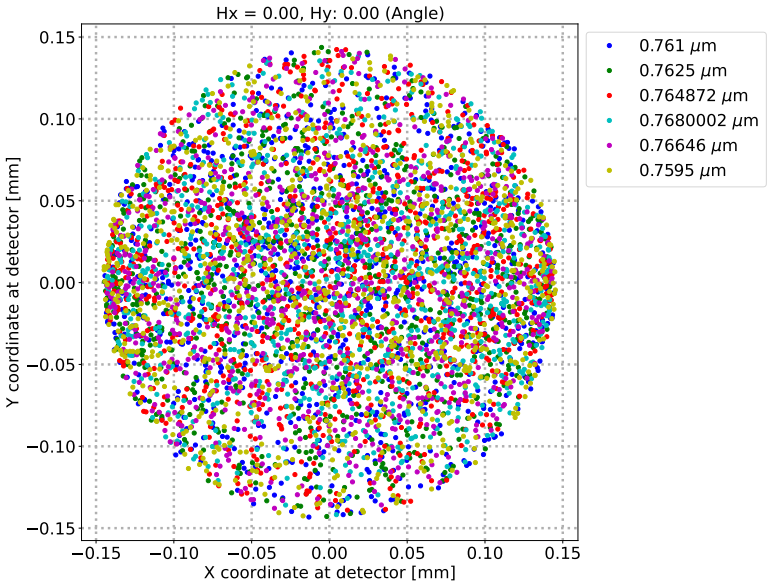

(a) GEO radius: 145.518 μm

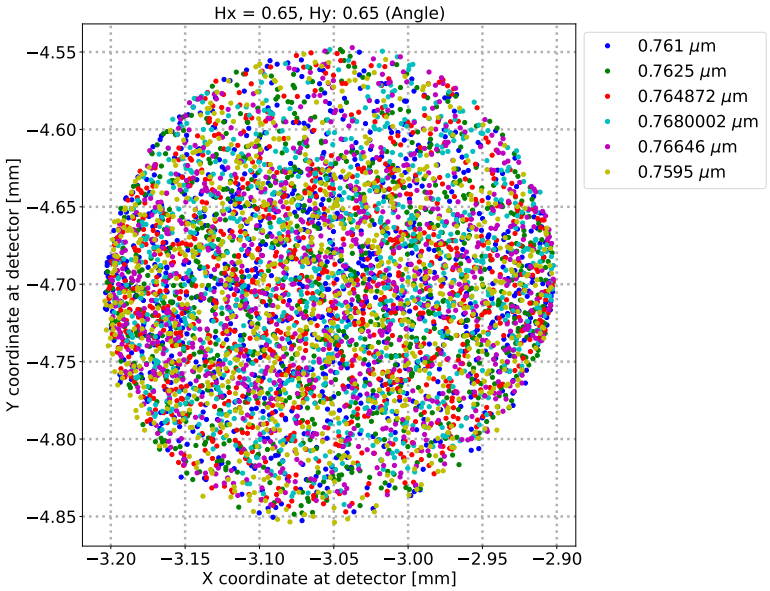

(b) GEO radius: 162.511 μm

Figure A.10: Spot diagrams at the different field points for the FM without the vacuum compensation under the vacuum environment.

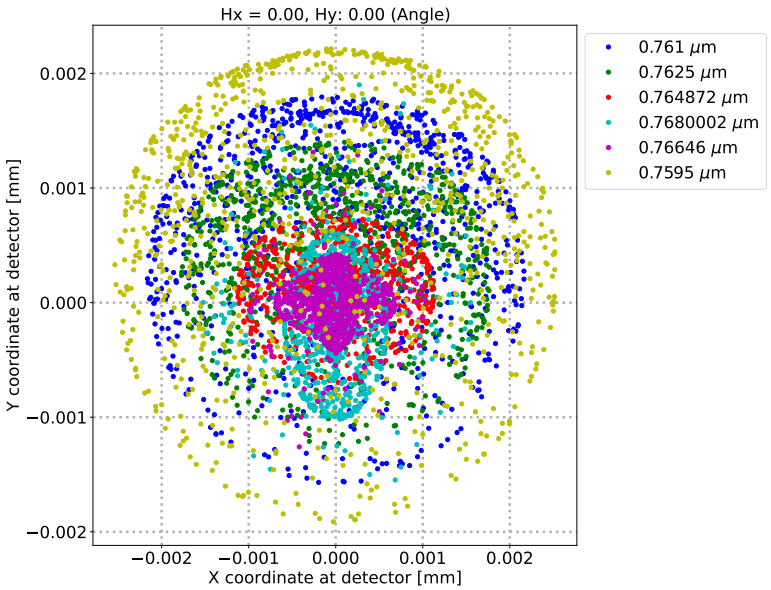

(a) GEO radius: 2.511 μm

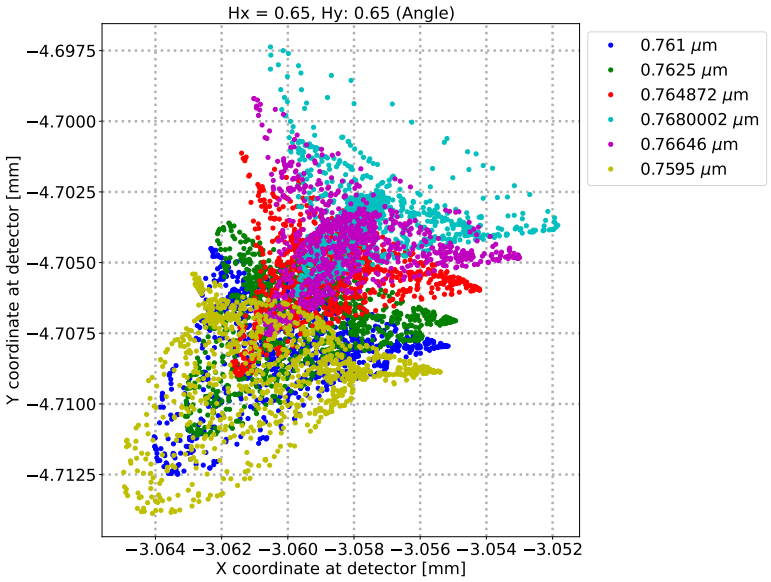

(b) GEO radius: 11.649 μm

Figure A.11: Spot diagrams at the different field points for the FM with the vacuum compensation under the vacuum environment.

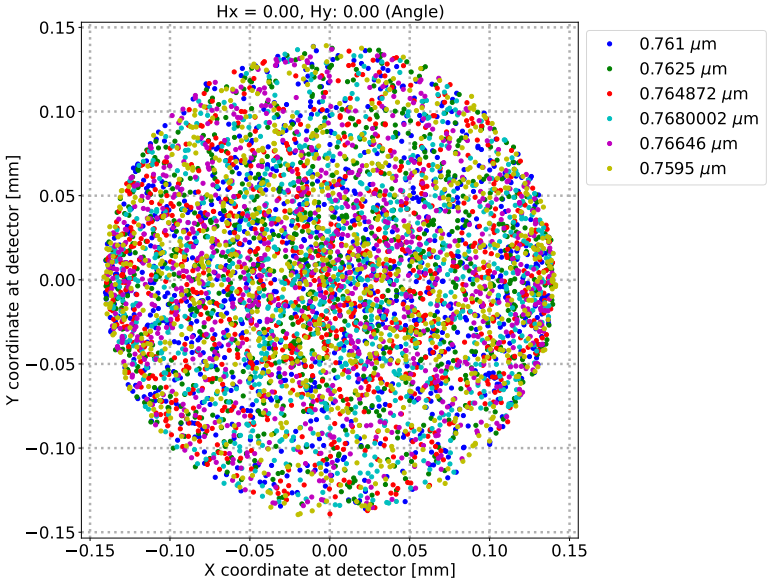

(a) GEO radius: 141.448 μm

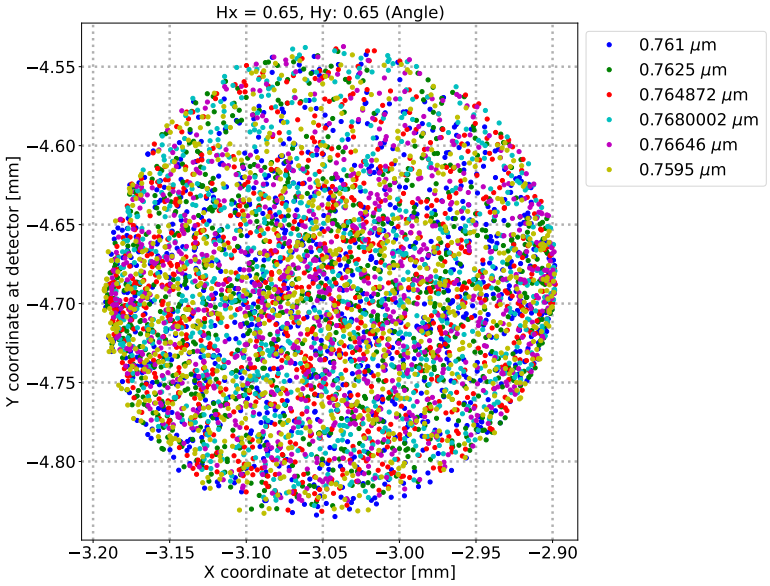

(b) GEO radius: 163.613 μm

Figure A.12: Spot diagrams at the different field points for the FM with moving the wrong direction of the vacuum compensation under the ambient environment.

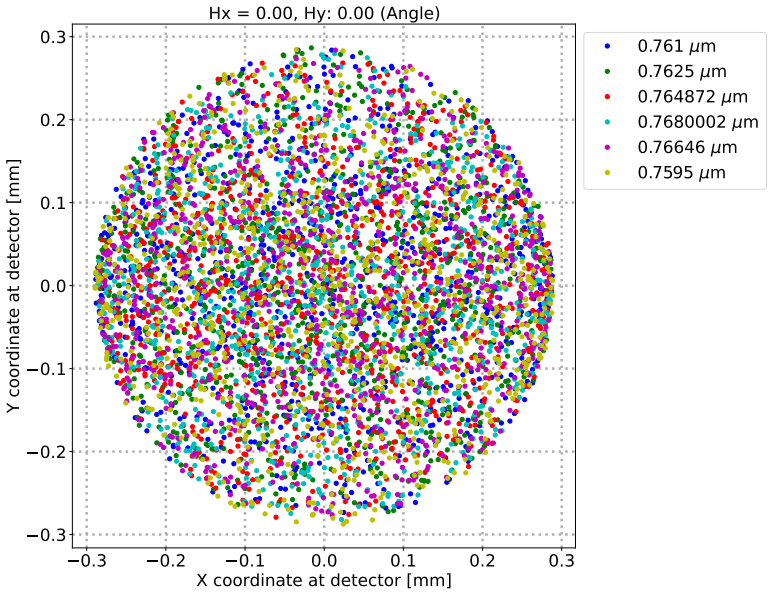

(a) GEO radius: 289.316 μm

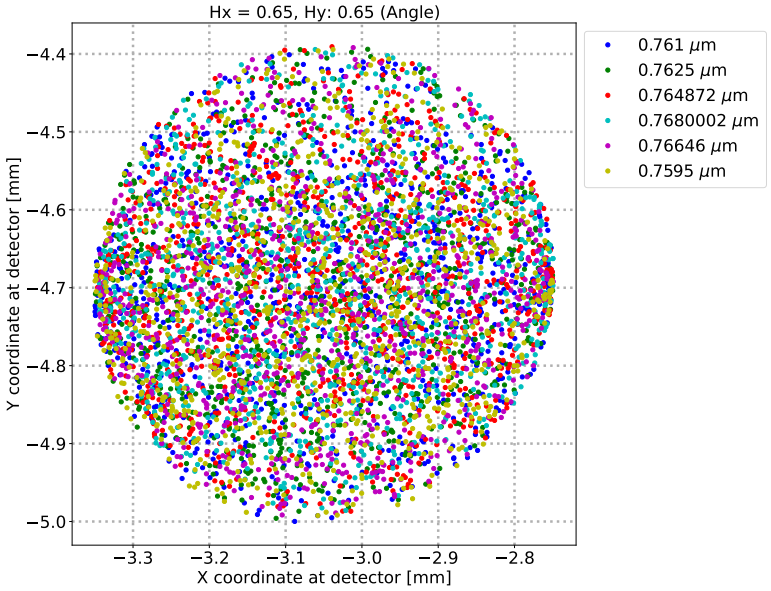

(b) GEO radius: 323.701 μm

Figure A.13: Spot diagrams at the different field points for the FM with moving the wrong direction of the vacuum compensation under the vacuum environment.

A.5 Pinhole setup measurements of the instrument after moving the vacuum compensation for the off-axis fields

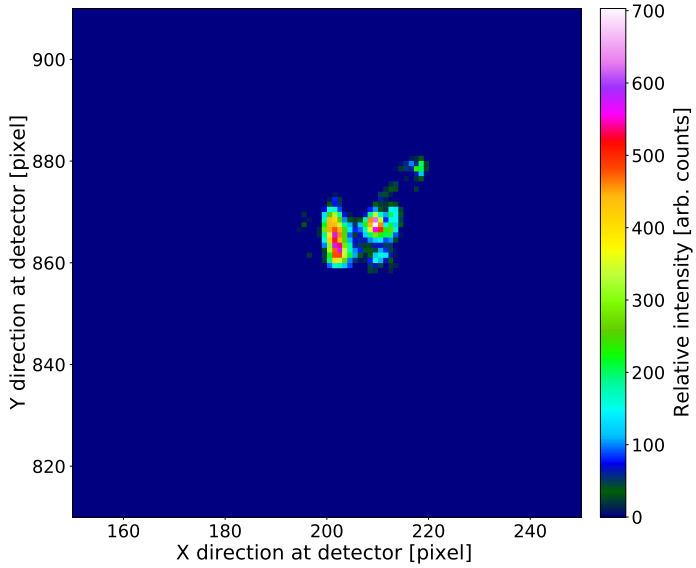

(a) The output image at the detector array.

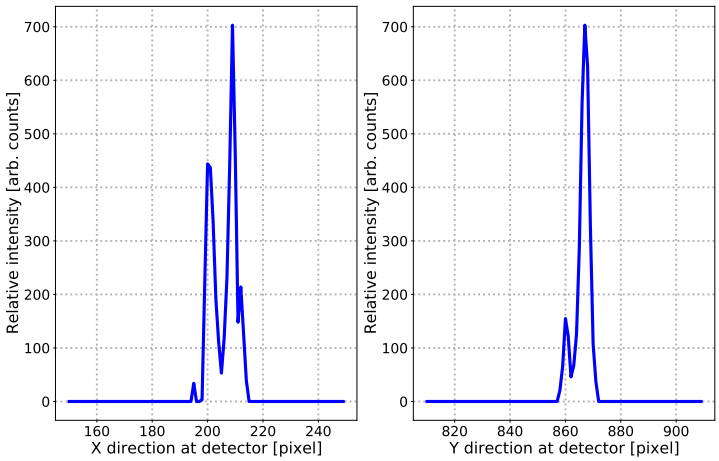

(b) The two cross slices at the brightest point of the image points.

Figure A.14: Points imaged by the pinhole setup under the ambient environment after moving the vacuum compensation, where the mode of the detector is HDR_LowGain and the orientation of the instrument is at the off-axis field.

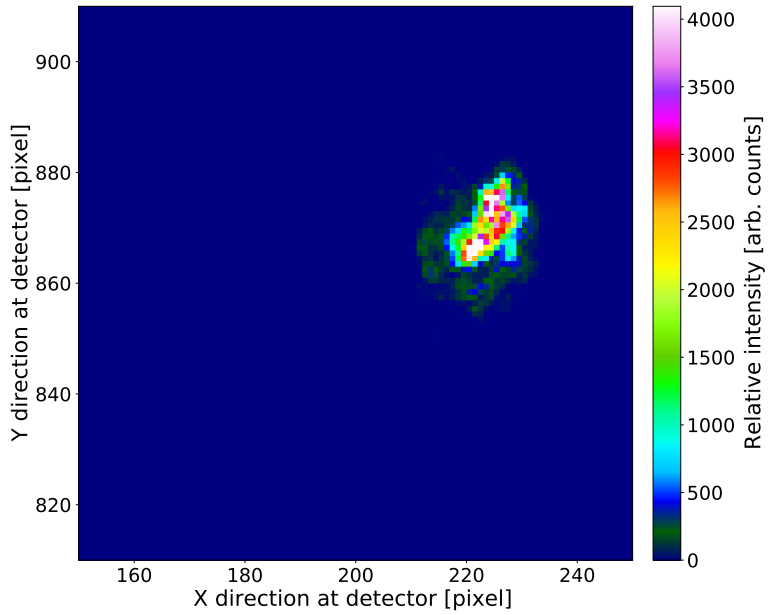

(a) The output image at the detector array.

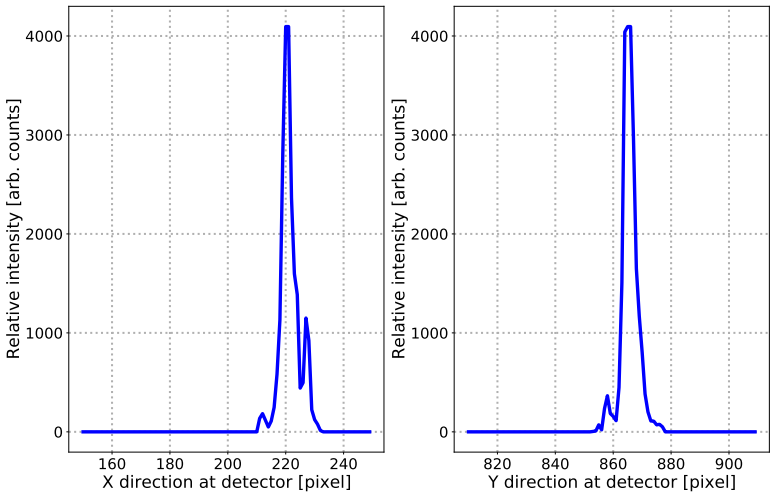

(b) The two cross slices at the brightest point of the image points.

Figure A.15: Points imaged by the pinhole setup under the vacuum environment after moving the vacuum compensation, where the mode of the detector is HDR_LowGain and the orientation of the instrument is at the off-axis field.

A.6 Pinhole setup measurements of the prototype instrument in the thermal chamber for the different temperatures.

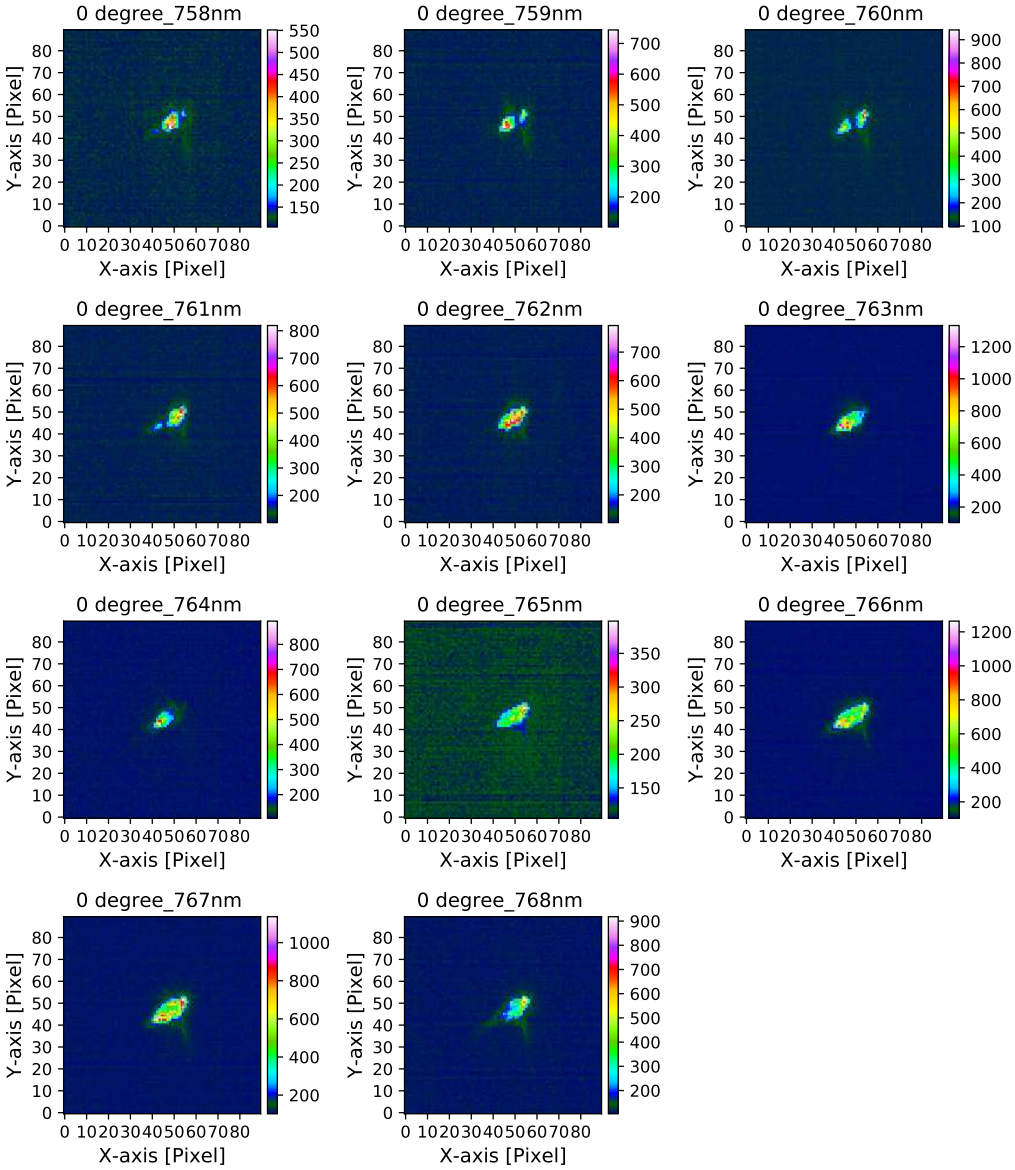

Figure A.16: Pinhole setup measurement results of the prototype instrument under the ambient environment for the different wavelengths at 0°C

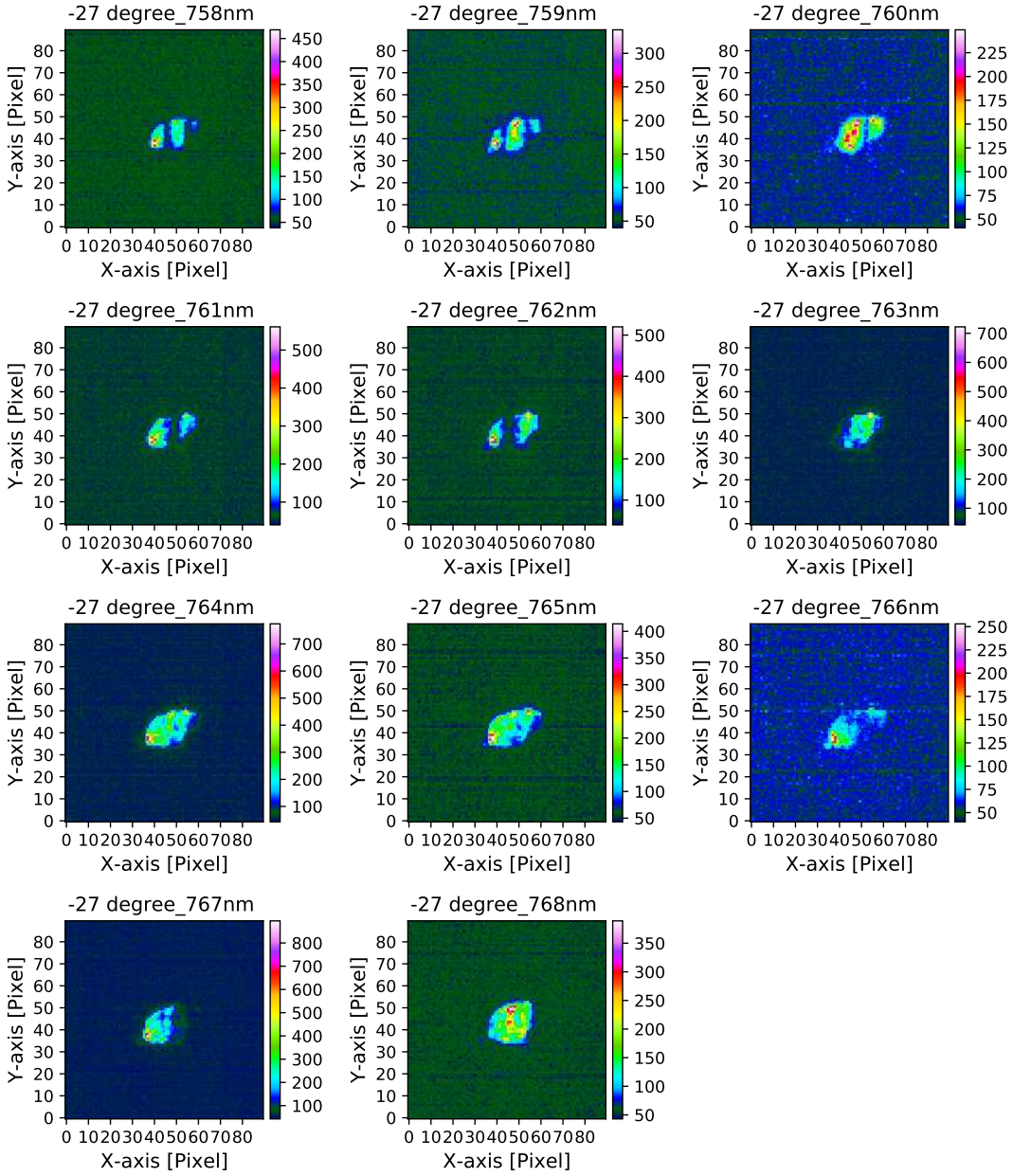

Figure A.17: Pinhole setup measurement results of the prototype instrument under the ambient environment for the different wavelengths at -27°C

Appendix B

Preliminary design of the UV-SHS

B.1 Design Framework Considerations for the UV-SHS

In order to design a spatial heterodyne interferometer (SHI), the system parameters such as the central working wavelength, the Littrow wavelength and the resolving power of the system should be first determined. This section describes how to determine the design parameters of an UV-SHS from a design point of view.

B.1.1 Research Background

The aim of designing an UV-SHS is to obtain the density and distribution of nitric oxide in the mesosphere and lower thermosphere by utilizing the gamma (γ) band emissions of nitric oxide in the dayglow.

The amount of nitric oxide in the upper atmosphere is highly variable. Its density is an indicator for solar and geomagnetic activity (*Barth*, 1996; *Siskind et al.*, 1997; *Hendrickx et al.*, 2017). At low latitudes the density of nitric oxide is controlled by the soft X-ray fluxes to the extreme ultraviolet (EUV) portion of the solar spectrum (*Barth et al.*, 1999). At polar latitudes it is controlled by the auroral and radiation belt electrons (*Feldman*, 1976; *Beiting III and Feldman*, 1978; *Solomon et al.*, 1999; *Barth et al.*, 2001).

Nitric oxide is the object of ionization in the D-region of the ionosphere by solar Lyman-α radiation (*Gylvan Meira Jr*, 1971a), because the energy to ionize this molecule is much lower than for other major constituents in the atmosphere. In the higher layers of the ionosphere (D and F1 regions), nitric oxide is an important reactant in the ion-molecule and charge exchange reactions (*Bailey et al.*, 2002).

Nitric oxide is also one of the major molecules affecting the energy balance of the upper atmosphere (*Roble et al.*, 1987; *Sætre et al.*, 2004). Like carbon dioxide (CO_2), it has vibration-rotation modes and emits infrared radiation. The nitric oxide thermal emissions at 5.3 μm contribute to the cooling of the lower thermosphere, especially for high solar activity (*Barth et al.*, 2009; *Barth*, 2010; *Hendrickx et al.*, 2018). The energy transfer from the ambient atmosphere to nitric oxide is done via collisions with atomic oxygen. Thereby a two channel observation of nitric oxide (in the UV and the infrared spectral region) can be used to derive the atomic oxygen abundance, which is another key constituent in the upper mesosphere and thermosphere.

Atomic oxygen is of high interest by itself, because it plays a key role in the thermal budget of the upper atmosphere as well (*Zhu et al.*, 2015; *Zhu and Kaufmann*, 2018, 2019; *Zhu*, 2016). It determines the amount of radiation emitted by CO_2 at 15 μm, in a similar way as for nitric oxide. This, in turn, affects the retrieval of temperature and other data observed by mid-infrared limb sounders like the Sounding of the Atmosphere using Broadband Emission Radiometry (SABER) instrument on the United States's (US) Thermosphere Ionosphere Mesosphere Energetics and Dynamics (TIMED) satellite, the Michelson Interferometer for Passive Atmospheric Sounding (MIPAS) instrument on the European Space Agency's (ESA) European Environmental Satellite (Envisat).

Furthermore, nitric oxide can be transported downward to the mesosphere and stratosphere by the mean meridional circulation, where it participates in the catalytic reactions destroying ozone (*Brasseur and Solomon*, 1984; *Barth*, 1992; *Marsh et al.*, 2004; *Sætre et al.*, 2007).

B.1.2 Production and Loss Mechanisms

The production mechanisms of nitric oxide in the upper atmosphere are mainly related to the ground state atomic nitrogen N(^{4}S) and metastable nitrogen atoms N(^{2}D) (*Barth*, 1992; *Bailey et al.*, 2002; *Gérard and Barth*, 1977):

$$\mathrm{N}(^4\mathrm{S}) + \mathrm{O}_2 \rightarrow \mathrm{NO} + \mathrm{O}, \tag{RB.1}$$

$$\mathrm{N}(^2\mathrm{D}) + \mathrm{O}_2 \rightarrow \mathrm{NO} + \mathrm{O}, \tag{RB.2}$$

where Reaction RB.2 provides the primary source of nitric oxide production in the upper atmosphere (*McPeters*, 1989).

The main loss mechanisms for nitric oxide are (*Marsh et al.*, 2004):

$$\mathrm{NO} + \mathrm{h}\nu \rightarrow \mathrm{N}(^4\mathrm{S}) + \mathrm{O}, \tag{RB.3}$$

$$\mathrm{N}(^4\mathrm{S}) + \mathrm{NO} \rightarrow \mathrm{N_2} + \mathrm{O}, \tag{RB.4}$$

where $h\nu$ represents the solar UV irradiance to provide the photodissociation of nitric oxide. Reaction RB.3 and Reaction RB.4 are so called 'cannibalistic reaction', in which the photodissociation of nitric oxide produces the ground state atomic nitrogen N(^{4}S) which can in turn react with nitric oxide to enhance the destruction rate.

Another loss mechanism is the reaction with ionized molecular oxygen $\mathrm{O_2^+}$:

$$\mathrm{NO} + \mathrm{O_2^+} \rightarrow \mathrm{NO^+} + \mathrm{O_2}. \tag{RB.5}$$

B.1.3 Emission Band Systems of Nitric Oxide

As discussed in Section B.1.1, there are two main emission channels of nitric oxide, the UV and infrared spectral region, respectively. The infrared emissions of nitric oxide are mainly caused by the vibrational transitions from the ground electronic state $X^2\Pi$ of NO (*Khomich et al.*, 2008):

$$\mathrm{NO}(\mathrm{X}^2\Pi, \mathrm{v} = 3) \rightarrow \mathrm{NO}(\mathrm{X}^2\Pi, \mathrm{v} = 0) + \mathrm{h}\nu(1.8\mu\mathrm{m}), \tag{RB.6}$$

$$\mathrm{NO}(\mathrm{X}^2\Pi, \mathrm{v} = 2) \rightarrow \mathrm{NO}(\mathrm{X}^2\Pi, \mathrm{v} = 0) + \mathrm{h}\nu(2.7\mu\mathrm{m}), \tag{RB.7}$$

$$\mathrm{NO}(\mathrm{X}^2\Pi, \mathrm{v} = 1) \rightarrow \mathrm{NO}(\mathrm{X}^2\Pi, \mathrm{v} = 0) + \mathrm{h}\nu(5.3\mu\mathrm{m}), \tag{RB.8}$$

where v represents the vibrational level. The Einstein coefficients which describe the probability of transition for spontaneous transitions RB.6, RB.7 and RB.8 are 0.067 $\mathrm{s^{-1}}$, 0.852 $\mathrm{s^{-1}}$ and 13.38 $\mathrm{s^{-1}}$, respectively (*Degges*, 1971; *Ogawa*, 1976; *Baker et al.*, 1977a; *Ogawa and Kondo*, 1977). The 5.3 μm emission is the most commonly measured emission band in the previous reports, like the German Cryogenic Infrared Spectrometers and Telescopes for the Atmosphere (CRISTA) measured the global distribution of nitric oxide infrared emissions during two US Space Shuttle missions in 1994 and 1997 (*Offermann et al.*, 1999; *Riese et al.*, 1999), the MIPAS instrument on Envisat measured nitric oxide 5.3 μm from 2003-2012 (*Fischer et al.*, 2008) and the Atmospheric Chemistry Experiment-Fourier Transform Spectrometer (ACE-FTS) aboard the Cana-

dian Atmospheric Chemistry Experiment (ACE) satellite measured infrared nitric oxide absorption spectra in the upper atmosphere since 2003 (*Bernath et al.*, 2005; *Sheese et al.*, 2013; *Bender et al.*, 2015).

For UV spectral regions, the gamma band system ($\gamma : A^2\Sigma^+ - X^2\Pi$), the delta band system ($\delta : C^2\Pi - X^2\Pi$), the beta bands system ($\beta : B^2\Pi - X^2\Pi$) and the epsilon band system ($\varepsilon : D^2\Sigma^+ - X^2\Pi$) that arise primarily in fluorescence from absorbing solar UV light are the result of electronic transitions of the NO molecule:

$$\begin{aligned} \mathrm{NO(v=0)} + \mathrm{h}\nu(\mathrm{solar}) &\rightarrow \mathrm{NO(A^2\Sigma^+, v')} \\ &\rightarrow \mathrm{NO(X^2\Pi, v'')} + \mathrm{h}\nu(\gamma), \end{aligned} \tag{RB.9}$$

$$\begin{aligned} \mathrm{NO(v=0)} + \mathrm{h}\nu(\mathrm{solar}) &\rightarrow \mathrm{NO(C^2\Pi, v')} \\ &\rightarrow \mathrm{NO(X^2\Pi, v'')} + \mathrm{h}\nu(\delta), \end{aligned} \tag{RB.10}$$

$$\begin{aligned} \mathrm{NO(v=0)} + \mathrm{h}\nu(\mathrm{solar}) &\rightarrow \mathrm{NO(B^2\Pi+, v')} \\ &\rightarrow \mathrm{NO(X^2\Pi, v'')} + \mathrm{h}\nu(\beta), \end{aligned} \tag{RB.11}$$

$$\begin{aligned} \mathrm{NO(v=0)} + \mathrm{h}\nu(\mathrm{solar}) &\rightarrow \mathrm{NO(D^2\Sigma^+, v')} \\ &\rightarrow \mathrm{NO(X^2\Pi, v'')} + \mathrm{h}\nu(\varepsilon), \end{aligned} \tag{RB.12}$$

where v' and v'' represent the vibrational levels of the excited and ground electronic states, respectively. Among these band systems, the gamma (γ) bands of nitric oxide in the dayglow are frequently measured to retrieve the abundance of nitric oxide due to its bright emission feature (*Piper and Cowles*, 1986; *Eparvier and Barth*, 1992; *Barth*, 1964).

B.1.4 Selection of Observational Emission Band from the Gamma Bands System

The gamma (γ) band emissions of upper atmospheric nitric oxide have been measured in many missions, such as sounding rocket-borne (*Barth*, 1964, 1966; *Pearce*, 1969; *Gylvan Meira Jr*, 1971b; *Feldman and Takacs*, 1974; *Baker et al.*, 1977b; *Clayton*, 1990; *Eparvier and Barth*, 1992; *Cleary et al.*, 1995) and satellite-borne experiments (*Rusch and Barth*, 1975; *Minschwaner et al.*, 2004; *Bender et al.*, 2013). Satellite based observations of the (1,0) γ-band of nitric oxide at twilight were performed by a nadir-viewing Ebert-Fastie UV scanning spectrometer on-board the polar orbiting satellite Orbiting

Geophysical Observatory 4 (OGO 4) in the 1960s (*Barth and Mackey*, 1969; *Rusch*, 1973; *Gérard and Barth*, 1977), which is the first time to observe the thermospheric nitric oxide based on satellite experiments. Later the (1,0) γ-band was also observed by the Solar Mesosphere Explorer (SME) from January 1982 to December 1986 (*Barth*, 1996). (1,4) γ-band was measured by the Solar Backscattered Ultraviolet (SBUV) spectral radiometer on the Nimbus-7 satellite in the 1980s (*Frederick and Serafino*, 1985). Then the Shuttle Solar Backscatter Ultraviolet (SSBUV) as the complement study of SBUV measured the (1,0) γ-band and (0,2) γ-band in the 1990s (*Stevens et al.*, 1997). In the late 1990s, the (0,1) γ-band was observed by the Ionospheric Spectroscopy and Atmospheric Chemistry (ISAAC) satellite instrument aboard the Advanced Research and Global Observing Satellite (ARGOS) for dayside limb observations (*Minschwaner et al.*, 2004). At roughly the same time, the polar orbiting satellite Student Nitric Oxide Explorer (SNOE) was launched to obtain the density of nitric oxide by measuring the (0,1) γ-band and (1,0) γ-band (*Merkel et al.*, 2001; *Barth et al.*, 2003; *Barth and Bailey*, 2004). The Scanning Imaging Absorption Spectrometer for Atmospheric Chartography (SCIAMACHY) instrument on the Envisat measured the nitric oxide UV-emissions from 2003 to 2012 and used the (0,2) γ-band, (1,4) γ-band and (1,5) γ-band to retrieve the NO densities (*Sinnhuber et al.*, 2016; *Bender et al.*, 2017). Figure B.1 shows a part of measured UV spectra from the SCIAMACHY's UV channel 1 for a tangent location of 73.335° N, 153.706° E and at 105.782 km height and a solar zenith angle (SZA) of 91.808° and a Universal Time Coordinated (UTC) time 2010-02-03 01:51:09, and the relatively bright emission lines are (0,1) γ-band, (0,2) γ-band and (1,4) γ-band.

The various gamma band emissions of nitric oxide can be divided into two main categories, resonant transitions and non-resonant transitions:

★ For resonant transitions, it connects to the ground vibrational state, where excitation and emission are at the same energy. These emission lines usually have high emissivity, but the disadvantage is that it may have self-absorptions from the source to the observer (*Stevens*, 1995), like the (1,0) γ-band, (2,0) γ-band, etc.

★ For non-resonant transitions, it does not connect to the ground vibrational state, where excitation and emission are at different energies. So self-absorptions can be negligible, but the emissivity is relatively lower (*Cleary*, 1986; *Siskind et al.*, 2004; *Cravens*, 1977), like the (0,1) γ-band, (0,2) γ-band, (1,4) γ-band and (1,5) γ-band, etc.

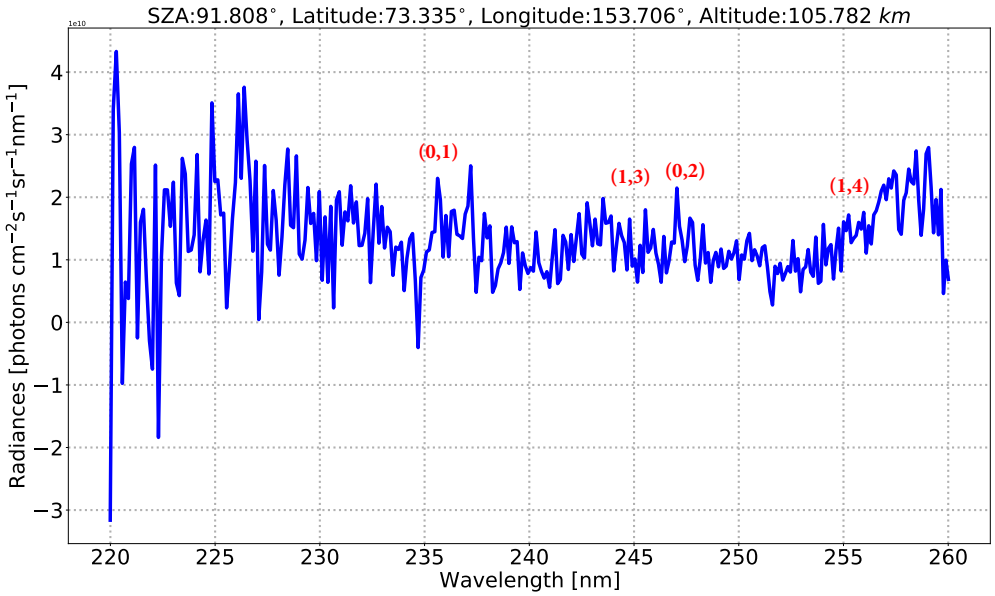

Figure B.1: Measured spectra from the SCIAMACHY's UV channel 1 for a tangent location of 73.335° N, 153.706° E and at 105.782 km height and a solar zenith angle of 91.808° and a UTC time 2010-02-03 01:51:09, where the relatively bright emission lines are (0,1) γ-band, (0,2) γ-band and (1,4) γ-band.

The relatively intense gamma bands of nitric oxide are listed in the Table B.1 (*Piper and Cowles*, 1986; *Luque and Crosley*, 1999):

Table B.1: The gamma bands of nitric oxide with the highest intensities

γ-band	Wavelength [nm]	Einstein coefficient [s^{-1}]
(2,0)	204.952	1.926E06
(1,0)	215.134	2.023E06
(1,1)	224.182	5.863E05
(0,0)	226.548	9.261E05
(0,1)	236.603	1.368E06
(0,2)	247.421	1.148E06

The (0,1) γ-band is selected as the observational emission band of the UV-SHS in this thesis because it is the non-resonant transition with the highest emission. Thus, it is not affected by self-absorption.

B.1.5 Design Parameter Considerations for the UV-SHS

The core components of the SHS consist of a beamsplitter, two field-widening prisms and two reflective diffraction gratings. The first step is to select suitable gratings. Determining the grating parameters depends on the desired theoretical spectral resolving power $R_{required}$.

The typical effective line width of the γ-band is about 0.064 nm (*Barth*, 1965) and the central emission wavelength of the (0,1) γ-band is near 236.603 nm. So the spectral resolving power $R_{required}$ is expected to be $R_{required} = \frac{\lambda_{working}}{\delta\lambda} = \frac{236.603\ nm}{0.064\ nm} \approx 3697$. Since the apodization function will lead to a broadening of the spectral lines in the subsequent Fourier transform processing, the actual required spectral resolving power R_{actual} should be $R_{actual} = \frac{236.603\ nm}{0.064\ nm/4} \approx 15000$, where the coefficient of 4 is from the degree of broadening of the main lobe of the Hanning window function. According to Equation 2.12, the spectral resolving power R_{actual} depends on the illuminated width W and the groove spacing d. A blazed holographic grating from Edmund Optics was selected for the UV-SHS. Table B.2 summarizes the main parameters of the grating. It can provide a theoretical spectral resolving power $R_{theoretical} = 2 \times 600 \times 21 = 25200$, where $R_{theoretical} > R_{actual}$ meets the designed accuracy.

Table B.2: Reflective diffraction grating specifications

Item	Description
Type	Reflective diffraction grating
Construction	Holographic grating
Groove density [grooves/mm]	600
Groove density tolerance [grooves/mm]	$\pm$ 0.5
Blaze angle [°]	$4°18'$
Clear aperture [mm]	21.0×21.0
Substrate	Float glass
Coating	Bare aluminum
Relative diffraction efficiency [%]	>55

The second step is to determine the Littrow wavelength λ_0 and the corresponding Littrow angle θ_L. A scientific CMOS image sensor GSENSE400BSI with a pixel size of 11 μm is planned to be used for the UV-SHS. Thus the sampling frequency $f_{sampling}$ is given by $f_{sampling} = \frac{1\ fringes}{11\ \mu m} \approx 909\ fringes/cm$. According to the Nyquist Shannon sampling theorem, the recorded maximum heterodyne spatial frequency f_x is equal to one-half of the sampling frequency: $f_x < \frac{f_{sampling}}{2} = 454.5\ fringes/cm$. The spatial

frequency f_x depends on the Littrow wavelength λ_0 and Littrow angle θ_L. After optimization iterations, the final Littrow wavelength λ_0 of the UV-SHS is set to 238.2 nm and the corresponding Littrow angle θ_L is 4.098°. The advantages of these values are that the Littrow angle θ_L is very close to the blaze angle of the grating, which is conducive to obtain high diffraction efficiency, and that the relatively small Littrow angle can reduce the astigmatism aberration. Based on the determined Littrow wavelength λ_0 and Littrow angle θ_L, Table B.3 shows the spatial frequencies of the emission lines from the (0,1) γ-band, where all recorded spatial frequencies meet the Nyquist frequency requirements.

Table B.3: Spatial frequencies of the emission band heads from the (0,1) γ-band

Wavenumber [cm^{-1}]	Wavelength [nm]	Spatial frequency [fringes/cm]
42177.94	237.0907	56
42201.66	236.9575	63
42264.89	236.603	81
42301.83	236.3964	91
42321.57	236.2861	97

The third step is to select the optical glass material of the beamsplitter and the field-widening prisms. Due to the UV fluorescence effect and low transmittance, ordinary optical glass materials are difficult to apply in the UV band. The SUPRASIL-1 glass from the HERAEUS is selected for the beamsplitter and field-widening prisms as it is the optically isotropic 3D-material, which is highly homogeneous and has no striations or bubbles in any of the three dimensions (*HERAEUS GLASS CO.,LTD*). The refractive index differences are less than 5×10^{-6} which indicates that the refractive index is homogeneous. Furthermore, it has no fluorescence, while having high transmittance (more than 90% at 230-250 nm) and best damage resistance to the UV light.

The fourth step is to determine the angle parameters of the field-widening prisms. Due to the visibility of the interferogram decreases as the off-axis angle increases, a field-widening technique can be employed to improve the system throughput and increase the fringe contrast for the off-axis angles. This technique can be implemented by inserting a prism between the beamsplitter and the reflective diffraction grating so that the images of the gratings on two arms will be coincident and perpendicular to the optical axis for the observer viewed from the exit pupil.

Harlander et al. (*Harlander*, 1991; *Harlander et al.*, 1992) analyzed the relationship between the incident angle β of the prisms and the Littrow angle of the system θ_L under

the approximation condition of the minimum deviation:

$$2\left(n^2-1\right)\tan\beta = n^2\tan\theta_L, \tag{B.1}$$

where n is the refractive index of the prism. The incident angle β can be obtained for a given Littrow angle from Equation B.1. Subsequently, the apex angle of the prism α can be obtained for the condition of the minimum deviation of the prism:

$$n\sin\frac{\alpha}{2} = \sin\beta. \tag{B.2}$$

These give the initial values of the prism design. The final values are obtained by iterative optimisation. For the designed UV-SHS, the second surface or the exit plane of the prism is parallel to the incident plane of the diffraction grating. The angle of the first surface (or the incident plane) of the field-widening prism γ_1 and the angle of the second surface of the field-widening prism γ_2 are given by the geometry relationship and Snell's law:

$$\begin{aligned}\gamma_1 &= \arcsin\left\{n*\sin\left[\alpha-\arcsin\left(\frac{\sin\theta_L}{n}\right)\right]\right\},\\ \gamma_2 &= \alpha-\gamma_1.\end{aligned} \tag{B.3}$$

Table B.4 summarises the values of the prism angles before and after optimisation.

Table B.4: The values of the prism angles before and after optimisation

	γ_1 [°]	γ_2 [°]	α [°]
Initial value	3.166	1.626	4.792
Iterative optimisation	3.154	1.633	4.787

The final step is to determine the size of the beamsplitter, the distance between the beamsplitter and the field-widening prism, and the distance between the field-widening prism and the grating. These values can be optimized using ZEMAX, a commercial optical ray-tracing software.

B.2 Simulation results of the UV-SHS

According to the above analysis and parameters, an optical ray-tracing model can be built to simulate the system performance. Figure B.2 shows the configuration of the field-widening UV-SHS. Only one arm is shown in this plot as the other arm is identical.

A paraxial lens is inserted in front of the beamsplitter to focus the infinity light source onto the grating without introducing additional wavefront aberrations. The different colour ray cones represent the different field points of the system. The simulation environment is set to 20.0 °C and 0.0 Pa. To verify the feasibility of the field-widening technique in the UV spectral region, two different FOV configurations are investigated. One is a large field of view configuration, which uses the FOV of 1.3°. This is similar to typical SHS instruments such as the AtmoSHINE instrument. The other is a small field of view configuration, corresponding to a non-imaging type SHS.

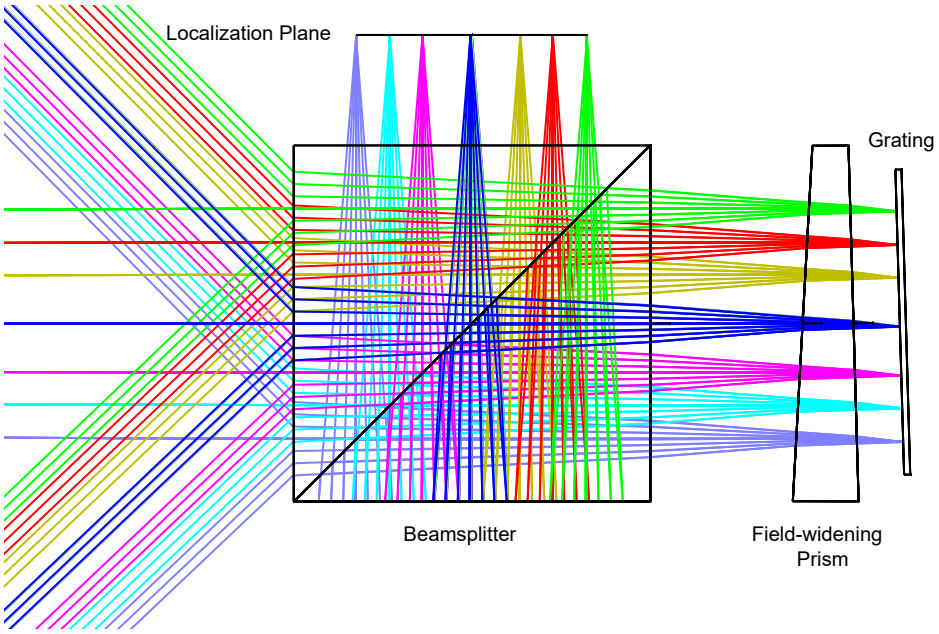

Figure B.2: Configuration of a field-widening UV-SHS consists of the beamsplitter, the field-widening prism and the grating. Different colored ray cones represent different field points.

The Wavefront error and OPD are two commonly used metrics to evaluate the properties of an optical system. The root mean squares (RMS) of the wavefront error for the small field configuration is shown in Figure B.3. The maximum RMS wavefront error and the minimum RMS wavefront error are 0.0863 waves and 0.0819 waves, respectively. For the large FOV configuration, the RMS wavefront field map is shown in Figure B.4. The maximum RMS wavefront error and the minimum RMS wavefront error are 0.1297 waves and 0.0944 waves, respectively. For both configurations, the RMS wavefront error is very small, which means that the field-widening technique is suitable for UV applications.

The OPD across the pupil positions for the small FOV configuration is shown in

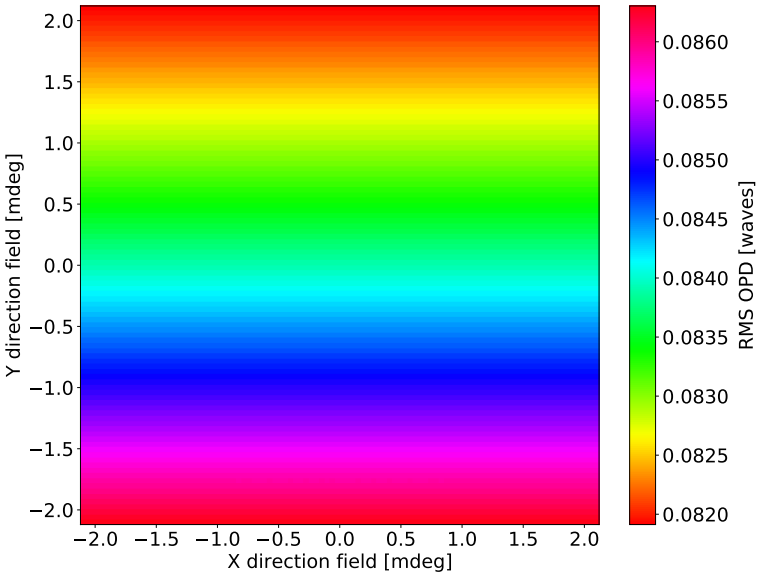

Figure B.3: RMS wavefront field map for the small field configuration with the sampling of 100 $\times$ 100 points.

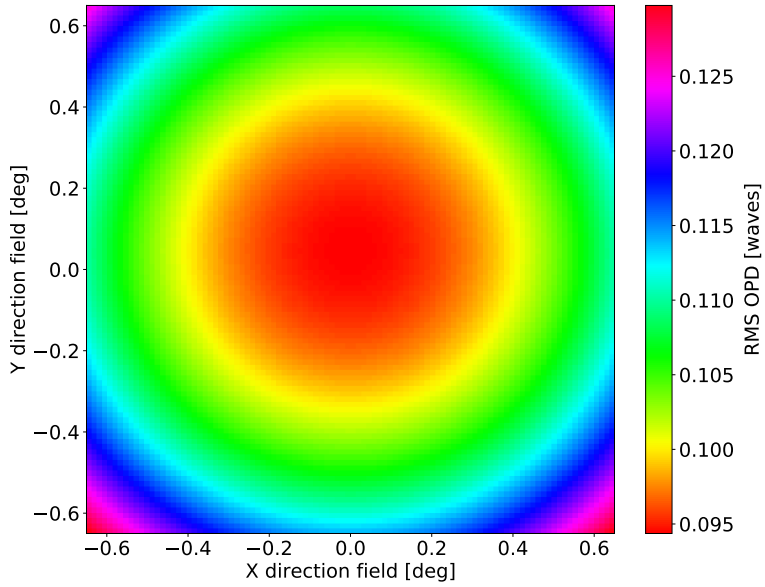

Figure B.4: RMS wavefront field map for the large field configuration with the sampling of 100 $\times$ 100 points.

Figure B.5, where the emission head of the (0,1) γ-band is 236.603nm, the calibration lamp emission wavelength is 237.83 nm and the designed Littrow wavelength of the UV-SHS is 238.2 nm. Figure B.5(a) and Figure B.5(b) show the OPD for the on-axis and off-axis field points, respectively. The OPDs at different pupil positions for different field points are less than 0.30 waves.

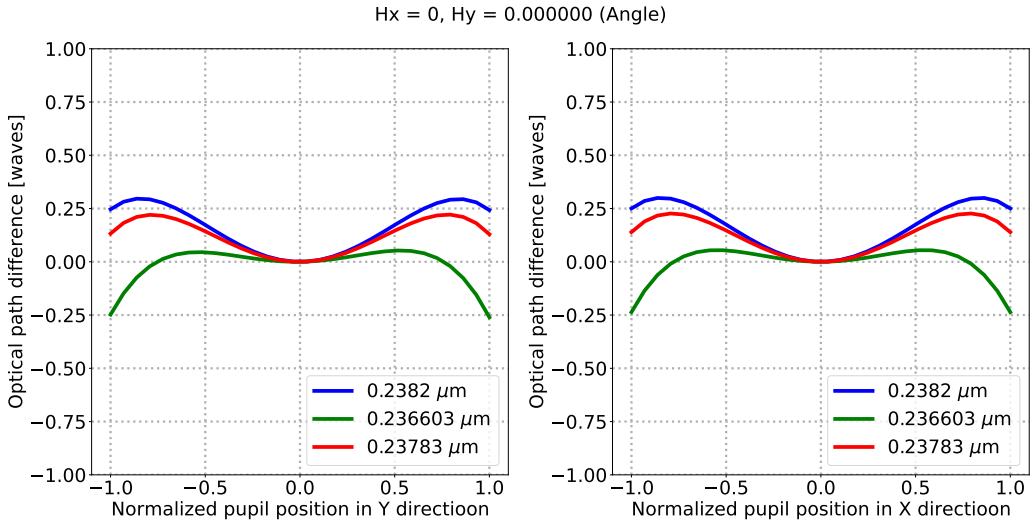

(a) OPD vs Pupil position at on-axis field point for the small FOV configuration

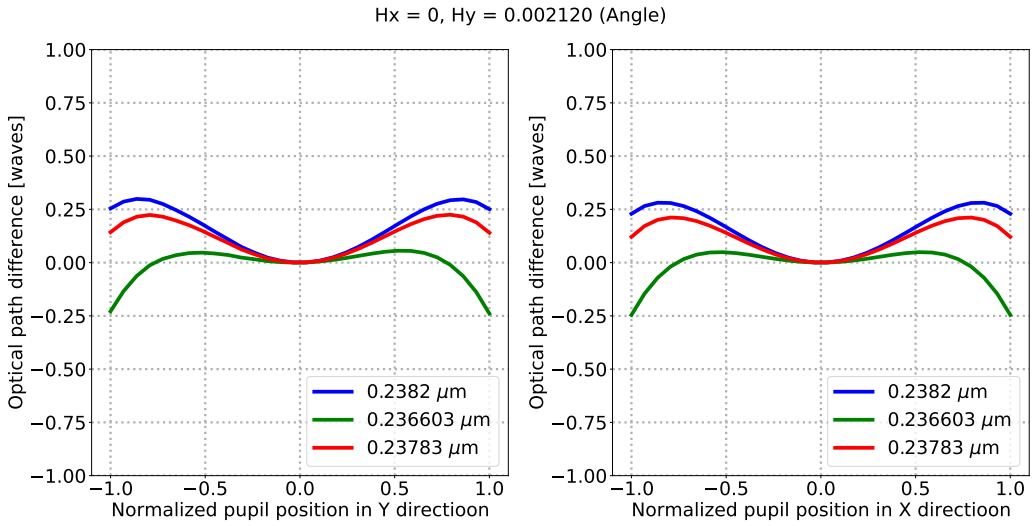

(b) OPD vs Pupil position at off-axis field point for the small FOV configuration

Figure B.5: OPD vs Pupil position of the small FOV configuration for the on-axis field point (a) and the off-axis field point (b) on the tangential plane (left) and the sagittal plane (right).

Figure B.6 shows the corresponding results for the large FOV configuration. The OPDs at different pupil positions and different field points are mostly less than 0.50 waves, and the maximum OPD is 0.65 waves, which indicates both configurations have the ability to obtain good interferogram visibility.

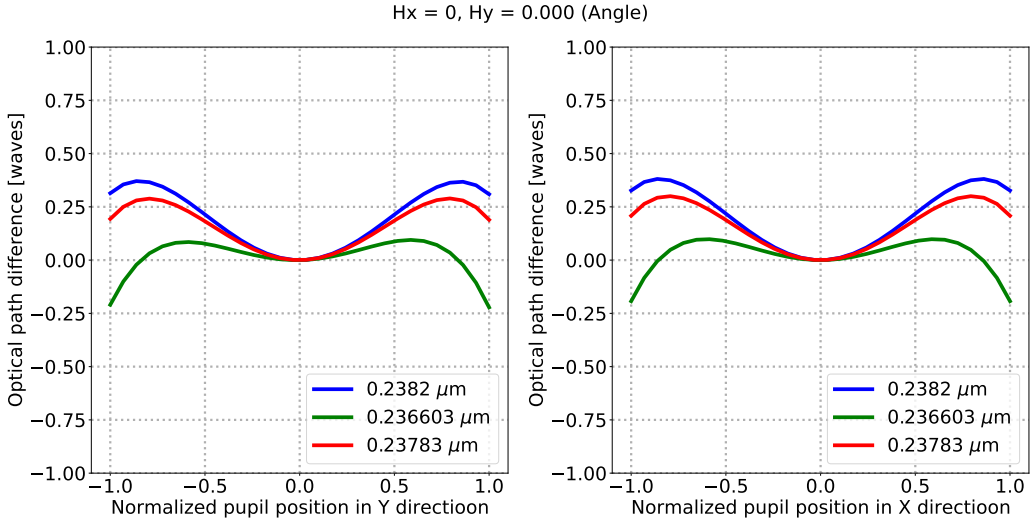

(a) OPD vs Pupil position at on-axis field point for the large FOV configuration

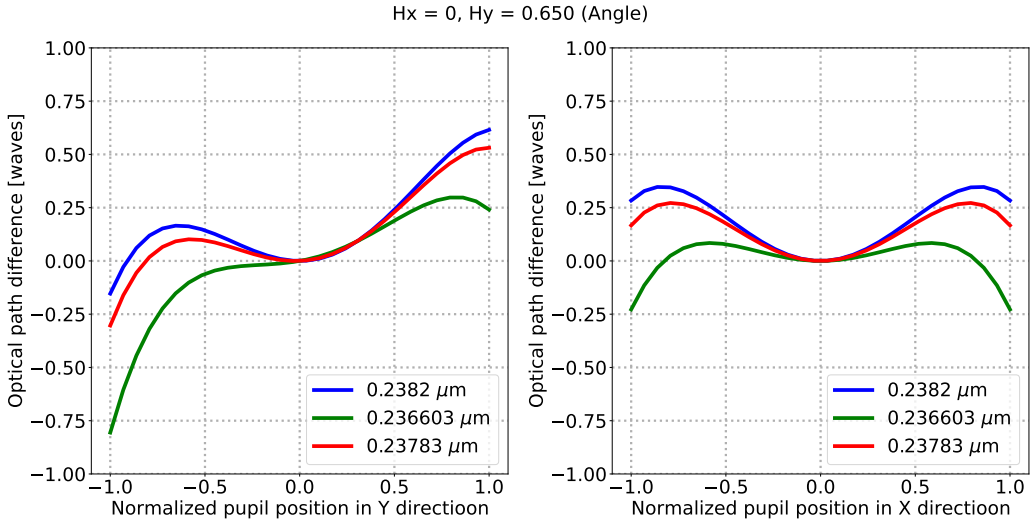

(b) OPD vs Pupil position at off-axis field point for the large FOV configuration

Figure B.6: OPD vs Pupil position of the large FOV configuration for the on-axis field point (a) and the off-axis field point (b) on the tangential plane (left) and the sagittal plane (right).

Acknowledgements

First and foremost, I would like to express my sincere gratitude to my doctoral supervisor Prof. Ralf Koppmann, for giving me the opportunity to join this professional research group and for his selfless help and support during my PhD studies at Bergische Universität Wuppertal. I am also sincerely grateful to Prof. Martin Riese for providing me with the opportunity to study at IEK-7, Forschungszentrum Jülich, and for his generous support and assistance in my studies and life.

I would like to give special thanks to my academic supervisor Dr. Martin Kaufmann. He brought me into the field of satellite instruments and patiently helped and supported me. He was not only a teacher to me but also an older friend who encouraged me to overcome difficulties. He also taught me how to think better about life.

My sincere thanks also go to Friedhelm Olschewski, Dr. Heinz Rongen and Tom Neubert for their support on the mechanical design and electronic experiments. I would also like to give special thanks to Mrs. Sabine Hoffmann-Senger for her patient support in all administrative matters.

Many thanks to Anton rabanus, Dr. Daikang Wei, Dr. Jilin Liu, Konstantin Ntokas, Marco Miebach, Dr. Qiuyu Chen. Dr. Rui Song, Tobias Augspurger, Dr. Yajun Zhu and other colleagues at IEK-7 and Bergische Universität Wuppertal for the pleasant and fulfilling time we worked together.

Finally and most importantly, I would like to thank my parents for their unconditional encouragement and support, which has been a constant motivation for me to improve. I sincerely hope they will always be healthy and happy.

Acronyms

ACE Atmospheric Chemistry Experiment.

ACE-FTS Atmospheric Chemistry Experiment-Fourier Transform Spectrometer.

ACU AtmoLITE Calibration Unit.

AOI Angle Of Incidence.

ARGOS Advanced Research and Global Observing Satellite.

AtmoLITE Atmospheric Limb Interferometer for Temperature Exploration.

AtmoSHINE Atmospheric Spatial Heterodyne Interferometer Next Exploration.

CRISTA Cryogenic Infrared Spectrometers and Telescopes for the Atmosphere.

DC Direct Current.

DN Digital Number.

Envisat Environmental Satellite.

ESA European Space Agency.

EUV Extreme Ultraviolet.

FFT Fast Fourier Transformation.

FM Flight Model.

FOV Field Of View.

FTS Fourier Transform Spectrometer.

FWHM Full Width at Half Maximum.

GEO Geometric.

GLORIA Gimballed Limb Observer for Radiance Imaging of the Atmosphere.

GPS Global Positioning System.

HDR High Dynamic Range.

IFFT Inverse Fast Fourier Transformation.

ILS Instrument Line Shape.

INSPIRE International Satellite Program in Research and Education.

ISAAC Ionospheric Spectroscopy and Atmospheric Chemistry.

ISF Interferogram Scale Factor.

MERIA Multiple Eye for Remote Investigation of the Atmosphere.

MIPAS Michelson Interferometer for Passive Atmospheric Sounding.

MLT Mesosphere and Lower Thermosphere.

MTF Modulation Transfer Function.

NO Nitric Oxide.

O_2 A-band Oxygen Atmospheric band.

OGO 4 Orbiting Geophysical Observatory 4.

OPD Optical Path Difference.

PCA Principal Component Analysis.

P-V Peak-to-Valley.

QM Qualification Model.

RMS Root Mean Square.

ROI Regions Of Interest.

RS Reflective Sphere.

SABER Sounding of the Atmosphere using Broadband Emission Radiometry.

SBUV Solar Backscattered Ultraviolet Spectral.

SCIAMACHY Scanning Imaging Absorption Spectrometer for Atmospheric Chartography.

SHI Spatial Heterodyne Interferometer.

SHS Spatial Heterodyne Spectrometer.

SME Solar Mesosphere Explorer.

SNOE Student Nitric Oxide Explorer.

SSBUV Shuttle Solar Backscatter Ultraviolet.

SZA Solar Zenith Angle.

TF Transmission Flat.

TIMED Thermosphere Ionosphere Mesosphere Energetics and Dynamics satellite.

TS Transmission Sphere.

US United States.

UTC Universal Time Coordinated.

WFE Wavefront Error.

List of Figures

List of Tables

Bibliography

Bailey, S. M., C. A. Barth, and S. C. Solomon (2002), A model of nitric oxide in the lower thermosphere, *Journal of Geophysical Research: Space Physics*, *107*(A8), SIA–22.

Baker, K., D. Baker, J. Ulwick, and A. Stair Jr (1977a), Measurements of 1.5-to 5.3-μm infrared enhancements associated with a bright auroral breakup, *Journal of Geophysical Research*, *82*(25), 3518–3528.

Baker, K., A. Nagy, R. Olsen, E. Oran, J. Randhawa, D. Strobel, and T. Tohmatsu (1977b), Measurement of the nitric oxide altitude distribution in the mid-latitude mesosphere, *Journal of Geophysical Research*, *82*(22), 3281–3286.

Barth, C. (1996), Reference models for thermospheric nitric oxide, 1994, *Advances in Space Research*, *18*(9-10), 179–208.

Barth, C., and S. Bailey (2004), Comparison of a thermospheric photochemical model with student nitric oxide explorer (snoe) observations of nitric oxide, *Journal of Geophysical Research: Space Physics*, *109*(A3).

Barth, C., D. Baker, K. Mankoff, and S. Bailey (2001), The northern auroral region as observed in nitric oxide, *Geophysical research letters*, *28*(8), 1463–1466.

Barth, C., K. D. Mankoff, S. Bailey, and S. Solomon (2003), Global observations of nitric oxide in the thermosphere, *Journal of Geophysical Research: Space Physics*, *108*(A1).

Barth, C., G. Lu, and R. Roble (2009), Joule heating and nitric oxide in the thermosphere, *Journal of Geophysical Research: Space Physics*, *114*(A5).

Barth, C. A. (1964), Rocket measurement of the nitric oxide dayglow, *Journal of Geophysical Research*, *69*(15), 3301–3303.

Barth, C. A. (1965), *Ultraviolet spectroscopy of planets*, Jet Propulsion Laboratory, California Institute of Technology.

Barth, C. A. (1966), Rocket measurement of nitric oxide in the upper atmosphere, *Planetary and Space Science*, *14*(7), 623–630.

Barth, C. A. (1992), Nitric oxide in the lower thermosphere, *Planetary and space science*, *40*(2-3), 315–336.

Barth, C. A. (2010), Joule heating and nitric oxide in the thermosphere, 2, *Journal of Geophysical Research: Space Physics*, *115*(A10).

Barth, C. A., and E. F. Mackey (1969), Ogo-iv ultraviolet airgiow spectrometer, *IEEE Transactions on Geoscience Electronics*, *7*(2), 114–119.

Barth, C. A., S. M. Bailey, and S. C. Solomon (1999), Solar-terrestrial coupling: Solar soft x-rays and thermospheric nitric oxide, *Geophysical research letters*, *26*(9), 1251–1254.

Beiting III, E., and P. Feldman (1978), A search for nitric oxide gamma band emission in an aurora, *Geophysical Research Letters*, *5*(1), 51–53.

Bender, S., M. Sinnhuber, J. P. Burrows, M. Langowski, B. Funke, and M. López-Puertas (2013), Retrieval of nitric oxide in the mesosphere and lower thermosphere from sciamachy limb spectra, *Atmospheric Measurement Techniques*, *6*(9), 2521–2531.

Bender, S., M. Sinnhuber, T. Von Clarmann, G. Stiller, B. Funke, M. López-Puertas, J. Urban, K. Pérot, K. Walker, and J. Burrows (2015), Comparison of nitric oxide measurements in the mesosphere and lower thermosphere from ace-fts, mipas, sciamachy, and smr, *Atmospheric Measurement Techniques*, *8*(10), 4171–4195.

Bender, S., M. Sinnhuber, M. Langowski, and J. P. Burrows (2017), Retrieval of nitric oxide in the mesosphere from sciamachy nominal limb spectra, *Atmospheric Measurement Techniques*, *10*(1), 209–220.

Bernath, P. F., C. T. McElroy, M. Abrams, C. D. Boone, M. Butler, C. Camy-Peyret, M. Carleer, C. Clerbaux, P.-F. Coheur, R. Colin, et al. (2005), Atmospheric chemistry experiment (ace): mission overview, *Geophysical Research Letters*, *32*(15).

Brasseur, G. P., and S. Solomon (1984), Aeronomy of the middle atmosphere: Chemistry and physics of the stratosphere and mesosphere, *dordrecht d.reidel publishing co.p*.

Cai, Q. (2016), Research on large aperture spatial heterodyne imaging spectroscopy, Ph.D. thesis, University of Science and Technology of China.

Cardon, J., C. Englert, J. Harlander, F. Roesler, and M. Stevens (2003), Shimmer on sts-112: development and proof-of-concept flight, in *AIAA Space 2003 Conference & Exposition*, p. 6224.

CDGM GLASS CO.,LTD (2018), OPTICAL GLASS DATABASE.

Chen, Q. (2020), Retrieval of atmospheric quantities from remote sensing measurements of nightglow emissions in the mlt region, Ph.D. thesis, Universität Wuppertal, Fakultät für Mathematik und Naturwissenschaften.

Clayton, M. J. (1990), Analysis of the ultraviolet emissions of nitric oxide from mid-latitude rocket observations, *Tech. rep.*, NAVAL POSTGRADUATE SCHOOL MONTEREY CA.

Cleary, D. D. (1986), Daytime high-latitude rocket observations of the no γ, δ, and ε bands, *Journal of Geophysical Research: Space Physics*, *91*(A10), 11,337–11,344.

Cleary, D. D., S. Gnanalingam, R. P. McCoy, K. F. Dymond, and F. Eparvier (1995), The middle ultraviolet dayglow spectrum, *Journal of Geophysical Research: Space Physics*, *100*(A6), 9729–9739.

Connes, P. (1958), Spectromètre interférentiel à sélection par l'amplitude de modulation, *Journal de Physique et le Radium*, *19*(3), 215–222.

Cooke, B. J., B. W. Smith, B. E. Laubscher, P. V. Villeneuve, and S. D. Briles (1999), Analysis and system design framework for infrared spatial heterodyne spectrometers, in *Infrared Imaging Systems: Design, Analysis, Modeling, and Testing X*, vol. 3701, edited by G. C. Holst, pp. 167 – 191, International Society for Optics and Photonics, SPIE, doi:10.1117/12.352971.

Cravens, T. (1977), Nitric oxide gamma band emission rate factor, *Planetary and Space Science*, *25*(4), 369–372.

Degges, T. (1971), Vibrationally excited nitric oxide in the upper atmosphere, *Applied optics*, *10*(8), 1856–1860.

Englert, C. R., J. M. Harlander, J. G. Cardon, and F. L. Roesler (2004), Correction of phase distortion in spatial heterodyne spectroscopy, *Applied optics*, *43*(36), 6680–6687.

Englert, C. R., J. M. Harlander, D. D. Babcock, M. H. Stevens, and D. E. Siskind (2006a), Doppler asymmetric spatial heterodyne spectroscopy (DASH): an innovative concept for measuring winds in planetary atmospheres, in *Atmospheric Optical Modeling, Measurement, and Simulation II*, edited by S. M. Hammel and A. Kohnle, p. 63030T, San Diego, California, USA, doi:10.1117/12.681704.

Englert, C. R., D. D. Babcock, and J. M. Harlander (2006b), Shimcad breadboard: design and characterization, *Tech. rep.*, NAVAL RESEARCH LAB WASHINGTON DC.

Englert, C. R., M. H. Stevens, D. E. Siskind, J. M. Harlander, and F. L. Roesler (2010), Spatial Heterodyne Imager for Mesospheric Radicals on STPSat-1, *Journal of Geophysical Research*, *115*(D20), doi:10.1029/2010JD014398.

Eparvier, F. G., and C. A. Barth (1992), Self-absorption theory applied to rocket measurements of the nitric oxide (1, 0) gamma band in the daytime thermosphere, *Journal of Geophysical Research*, *97*(A9), 13,723.

Feldman, P. D. (1976), Nitric oxide gamma band emission in an aurora, *Geophysical Research Letters*, *3*(1), 9–12.

Feldman, P. D., and P. Z. Takacs (1974), Nitric oxide gamma and delta band emission at twilight, *Geophysical Research Letters*, *1*(4), 169–171.

Fischer, H., M. Birk, C. Blom, B. Carli, M. Carlotti, T. von Clarmann, L. Delbouille, A. Dudhia, D. Ehhalt, M. Endemann, J. M. Flaud, R. Gessner, A. Kleinert, R. Koopman, J. Langen, M. López-Puertas, P. Mosner, H. Nett, H. Oelhaf, G. Perron, J. Remedios, M. Ridolfi, G. Stiller, and R. Zander (2008), MIPAS: an instrument for atmospheric and climate research, *Atmospheric Chemistry and Physics*, *8*(8), 2151–2188, doi:10.5194/acp-8-2151-2008.

Frederick, J., and G. Serafino (1985), Satellite observations of the nitric oxide dayglow: Implications for the behavior of mesospheric and lower-thermospheric odd nitrogen, *Journal of Geophysical Research: Atmospheres*, *90*(D2), 3821–3830.

Gérard, J.-C., and C. Barth (1977), High-latitude nitric oxide in the lower thermosphere, *Journal of Geophysical Research*, *82*(4), 674–680.

Gong (2020), Wavefront error measurements on shs front and camera optics for the atmolite instrument.

Gray, R. W., C. Dunn, K. P. Thompson, and J. P. Rolland (2012), An analytic expression for the field dependence of zernike polynomials in rotationally symmetric optical systems, *Optics Express*, *20*(15), 16,436–16,449.

Gylvan Meira Jr, L. (1971a), Rocket measurements of upper atmospheric nitric oxide and their consequences to the lower ionosphere, *Journal of Geophysical Research*.

Gylvan Meira Jr, L. (1971b), Rocket measurements of upper atmospheric nitric oxide and their consequences to the lower ionosphere, *Journal of Geophysical Research*, *76*(1), 202–212.

Harlander, J., R. J. Reynolds, and F. L. Roesler (1992), Spatial heterodyne spectroscopy for the exploration of diffuse interstellar emission lines at far-ultraviolet wavelengths, *The Astrophysical Journal*, *396*, 730–740.

Harlander, J., K. Marr, and C. Englert (2019a), Mighti level 1 data analysis summary, *Tech. rep.*, NAVAL RESEARCH LAB WASHINGTON DC.

Harlander, J. M. (1991), Spatial Heterodyne Spectroscopy: Interferometric Performance at any Wavelength Without Scanning, Ph.D. thesis, The University of Wisconsin-Madison, The University of Wisconsin - Madison.

Harlander, J. M., H. Tran, F. L. Roesler, K. P. Jaehnig, S. M. Seo, W. T. Sanders III, and R. J. Reynolds (1994), Field-widened spatial heterodyne spectroscopy: correcting for optical defects and new vacuum ultraviolet performance tests, in *EUV, X-Ray, and Gamma-Ray Instrumentation for Astronomy V*, vol. 2280, pp. 310–319, International Society for Optics and Photonics.

Harlander, J. M., C. R. Englert, K. D. Marr, B. J. Harding, and K. T. Chu (2019b), On the uncertainties in determining fringe phase in doppler asymmetric spatial heterodyne spectroscopy, *Applied optics*, *58*(13), 3613–3619.

Harris, W., F. Roesler, L. Ben-Jaffel, E. Mierkiewicz, J. Corliss, R. Oliversen, and T. Neef (2005), Applications of spatial heterodyne spectroscopy for remote sensing of diffuse uv–vis emission line sources in the solar system, *Journal of Electron Spectroscopy and Related Phenomena*, *144*, 973–977.

Hendrickx, K., L. Megner, D. R. Marsh, J. Gumbel, R. Strandberg, and F. Martinsson (2017), Relative importance of nitric oxide physical drivers in the lower thermosphere, *Geophysical Research Letters*, *44*(19), 10–081.

Hendrickx, K., L. Megner, D. R. Marsh, and C. Smith-Johnsen (2018), Production and transport mechanisms of no in the polar upper mesosphere and lower thermosphere in observations and models, *Atmospheric Chemistry and Physics*, *18*(12), 9075–9089.

HERAEUS GLASS CO.,LTD (), OPTICAL GLASS DATABASE.

Kaufmann, M., F. Olschewski, K. Mantel, B. Solheim, G. Shepherd, M. Deiml, J. Liu, R. Song, Q. Chen, O. Wroblowski, D. Wei, Y. Zhu, F. Wagner, F. Loosen, D. Froehlich, T. Neubert, H. Rongen, P. Knieling, P. Toumpas, J. Shan, G. Tang, R. Koppmann, and M. Riese (2018), A highly miniaturized satellite payload based on a spatial heterodyne spectrometer for atmospheric temperature measurements in the mesosphere and lower thermosphere, *Atmospheric Measurement Techniques*, *11*(7), 3861–3870, doi:10.5194/amt-11-3861-2018.

Khomich, V. Y., A. I. Semenov, and N. N. Shefov (2008), *Airglow as an indicator of upper atmospheric structure and dynamics*, Springer Science & Business Media.

Lakshminarayanan, V., and A. Fleck (2011), Zernike polynomials: a guide, *Journal of Modern Optics*, *58*(7), 545–561.

Lin, Y. (2010), *Instrument development for spatial heterodyne observations of water*, York University.

Liu, J. (2019), Study on a miniaturized satellite payload for atmospheric temperature measurements, Ph.D. thesis, Universität Wuppertal, Fakultät für Mathematik und Naturwissenschaften.

Luque, J., and D. R. Crosley (1999), Transition probabilities and electronic transition moments of the a 2 σ+–x 2 π and d 2 σ+–x 2 π systems of nitric oxide, *The Journal of chemical physics*, *111*(16), 7405–7415.

Marsh, D., S. Solomon, and A. Reynolds (2004), Empirical model of nitric oxide in the lower thermosphere, *Journal of Geophysical Research: Space Physics*, *109*(A7).

McPeters, R. (1989), Climatology of nitric oxide in the upper stratosphere, mesosphere, and thermosphere: 1979 through 1986, *Journal of Geophysical Research: Atmospheres*, *94*(D3), 3461–3472.

Merkel, A., C. Barth, and S. Bailey (2001), Altitude determination of ultraviolet measurements made by the student nitric oxide explorer, *Journal of Geophysical Research: Space Physics*, *106*(A12), 30,283–30,290.

Milligan, S., J. W. Howard, B. E. Laubscher, B. W. Smith, R. R. Berggren, and J. M. Harlander (1999), Optical design of an imaging spatial heterodyne infrared spectrometer, in *Infrared Technology and Applications XXV*, vol. 3698, pp. 869–881, International Society for Optics and Photonics.

Minschwaner, K., J. Bishop, S. Budzien, K. Dymond, D. Siskind, M. Stevens, and R. McCoy (2004), Middle and upper thermospheric odd nitrogen: 2. measurements of nitric oxide from ionospheric spectroscopy and atmospheric chemistry (isaac) satellite observations of no γ band emission, *Journal of Geophysical Research: Space Physics*, *109*(A1).

Ntokas, K. (2022), To be submitted, Ph.D. thesis, University of Wuppertal.

Offermann, D., K.-U. Grossmann, P. Barthol, P. Knieling, M. Riese, and R. Trant (1999), Cryogenic Infrared Spectrometers and Telescopes for the Atmosphere (CRISTA) experiment and middle atmosphere variability, *Journal of Geophysical Research: Atmospheres*, *104*(D13), 16,311–16,325, doi:10.1029/1998JD100047.

Ogawa, T. (1976), Excitation processes of infrared atmospheric emissions, *Planetary and Space Science*, *24*(8), 749–756.

Ogawa, T., and Y. Kondo (1977), Diurnal variability of thermospheric n and no, *Planetary and Space Science*, *25*(8), 735–742.

Pearce, J. B. (1969), Rocket measurement of nitric oxide between 60 and 96 kilometers, *Journal of Geophysical Research*, *74*(3), 853–861.

Piper, L. G., and L. M. Cowles (1986), Einstein coefficients and transition moment variation for the NO ($A^2\Sigma^+ - X^2\Pi$) transition, *The Journal of chemical physics*, *85*(5), 2419–2422.

Riese, M., R. Spang, P. Preusse, M. Ern, M. Jarisch, D. Offermann, and K. U. Grossmann (1999), Cryogenic Infrared Spectrometers and Telescopes for the Atmosphere (CRISTA) data processing and atmospheric temperature and trace gas retrieval, *Journal of Geophysical Research: Atmospheres*, *104*(D13), 16,349–16,367, doi:10.1029/1998JD100057.

Riley, M., and M. Gusinow (1977), Laser beam divergence utilizing a lateral shearing interferometer, *Applied Optics*, *16*(10), 2753–2756.

Roble, R., E. Ridley, and R. Dickinson (1987), On the global mean structure of the thermosphere, *Journal of Geophysical Research: Space Physics*, *92*(A8), 8745–8758.

Rusch, D., and C. Barth (1975), Satellite measurements of nitric oxide in the polar region, *Journal of Geophysical Research*, *80*(25), 3719–3721.

Rusch, D. W. (1973), Satellite ultraviolet measurements of nitric oxide fluorescence with a diffusive transport model, *Journal of Geophysical Research*, *78*(25), 5676–5686.

Sætre, C., J. Stadsnes, H. Nesse, A. Aksnes, S. Petrinec, C. Barth, D. Baker, R. Vondrak, and N. Østgaard (2004), Energetic electron precipitation and the no abundance in the upper atmosphere: A direct comparison during a geomagnetic storm, *Journal of Geophysical Research: Space Physics*, *109*(A9).

Sætre, C., C. Barth, J. Stadsnes, N. Østgaard, S. Bailey, D. Baker, G. Germany, and J. Gjerloev (2007), Thermospheric nitric oxide at higher latitudes: Model calculations with auroral energy input, *Journal of Geophysical Research: Space Physics*, *112*(A8).

Santiago-Alvarado, A., S. Vázquez-Montiel, F. Granados-Agustín, J. Munoz-López, E. Percino-Zacarias, and J. González-García (2009), Functional characterization of a liquid lens using a zygo interferometer, in *Seventh Symposium Optics in Industry*, vol. 7499, pp. 232–239, SPIE.

Sheese, P., K. Strong, R. Gattinger, E. Llewellyn, J. Urban, C. Boone, and A. Smith (2013), Odin observations of antarctic nighttime no densities in the mesosphere–lower thermosphere and observations of a lower no layer, *Journal of Geophysical Research: Atmospheres*, *118*(13), 7414–7425.

Shukla, R., and D. Udupa (2000), Zygo interferometer for measuring refractive index of liquids and its application for heavy water analysis, *Optics & laser technology*, *32*(5), 355–360.

Shukla, R., D. Udupa, and M. Aggarwal (1998), Zygo interferometer for measuring refractive index of photorefractive bismuth silicon oxide (bi12sio20) crystal, *Optics & Laser Technology*, *30*(6-7), 425–430.

Sinnhuber, M., F. Friederich, S. Bender, and J. Burrows (2016), The response of mesospheric no to geomagnetic forcing in 2002–2012 as seen by sciamachy, *Journal of Geophysical Research: Space Physics*, *121*(4), 3603–3620.

Siskind, D. E., J. T. Bacmeister, M. E. Summers, and J. M. Russell (1997), Two-dimensional model calculations of nitric oxide transport in the middle atmosphere and comparison with halogen occultation experiment data, *Journal of Geophysical Research Atmospheres*, *102*(D3), 3527–3545.

Siskind, D. E., J. Picone, M. Stevens, and K. Minschwaner (2004), Middle and upper thermospheric odd nitrogen: 1. a new analysis of rocket data, *Journal of Geophysical Research: Space Physics*, *109*(A1).

Solomon, S. C., C. A. Barth, and S. M. Bailey (1999), Auroral production of nitric oxide measured by the snoe satellite, *Geophysical Research Letters*, *26*(9), 1259–1262.

Stevens, M. H. (1995), Nitric oxide γ band fluorescent scattering and self-absorption in the mesosphere and lower thermosphere, *Journal of Geophysical Research: Space Physics*, *100*(A8), 14,735–14,742.

Stevens, M. H., D. E. Siskind, E. Hilsenrath, R. P. Cebula, J. W. Leitch, J. M. Russell III, and L. L. Gordley (1997), Shuttle solar backscatter uv observations of nitric oxide in the upper stratosphere, mesosphere, and thermosphere: Comparisons with the halogen occultation experiment, *Journal of Geophysical Research: Space Physics*, *102*(A5), 9717–9727.

Watchorn, S. R. (2001), *The development of the Spatial Heterodyne Spectrometer for observations of C IV emissions near 1500 A from the cygnus loop and the diffuse hot interstellar medium*, The University of Wisconsin-Madison.

Wroblowski, O. (2022), To be submitted, Ph.D. thesis, University of Wuppertal.

Yi, Y., S. Zhang, F. Liu, Y. Zhang, and F. Yi (2017), Laboratory fabrication of monolithic interferometers for one and two-dimensional spatial heterodyne spectrometers, *Optics Express*, *25*(23), 29,121–29,134.

ZEMAX LLC. (2020), OpticStudio_usermanual.

Zhu, Y. (2016), Atomic oxygen derived from SCIAMACHY O(^{1}S) and OH airglow measurements in the Mesopause region, Ph.D. thesis, University of Wuppertal.

Zhu, Y., and M. Kaufmann (2018), Atomic oxygen abundance retrieved from SCIAMACHY hydroxyl nightglow measurements, *Geophysical Research Letters*, *45*(17), 9314–9322, doi:10.1029/2018GL079259.

Zhu, Y., and M. Kaufmann (2019), Consistent nighttime atomic oxygen concentrations from O_2 A-band, O(^{1}S) green-line, and OH airglow measurements as performed by SCIAMACHY, *Geophysical Research Letters*, *46*(14), 8536–8545, doi:10.1029/2019GL083550.

Zhu, Y., M. Kaufmann, M. Ern, and M. Riese (2015), Nighttime atomic oxygen in the mesopause region retrieved from SCIAMACHY O(^{1}S) green line measurements and its response to solar cycle variation, *Journal of Geophysical Research: Space Physics*, *120*(10), 9057–9073, doi:10.1002/2015JA021405.

ZYGO. (2015), Zygo_Typical Interferometer Setups.